Chapter III. *De Novo* Design and Characterization of Copper Metallopeptides Inspired by Cupredoxin Centers

Introduction

Electron transfer (ET) is the simplest chemical transformation in a redox reaction. This reaction plays a central role in numerous energy processes including photosynthesis and respiration, two biological systems that sustain all life on earth.[1, 2] Found in bacteria, algae, plants and animals, cupredoxins or type one copper centers (CuT1) are copper electron transfer proteins that have been extensively studied to understand this fundamental reaction.[3-6] CuT1 centers are often described using the entatic state or rack-induced bonding model,[7] which proposes that the β-barrel fold forces the copper ion, regardless of the oxidation state, into a strict geometry that allows for minimal change in the coordination environment during ET. This structural feature provides CuT1 centers with unusual spectroscopic, structural and redox properties, which have been comprehensively characterized.[8, 9] For these reasons, cupredoxins offer an attractive metal center to model using protein design. Overall, the objective of the work in this chapter is to impart the α_3D scaffold with the asymmetric CuT1 center and examine if the physical properties this native copper site can be retained in this scaffold. Ultimately, my goal is incorporate a cupredoxin-inspired ET site in α_3D.

A Greek β-barrel fold encompasses the copper center, where the metal binding site is provided by two loops that connect two separate β-strands. The copper ion is coordinated to three equatorial ligands, which is comprised of two N(His) and one S(Cys), as well as one or two more weakly bound axial ligands, such as S(Met) or O(Gln), to form a 3- to 5-coordinate copper complex. This copper center is tightly constrained by an elaborate network of hydrogen bonding

XAS work is a collaboration with Dr. James Penner-Hahn from University of Michigan Biophysics/Chemistry Department. XANES and EXAFS data were analyzed and fitted by Drs. Aniruddha Deb (Chemistry) and James-Penner-Hahn.

and hydrophobic interactions, resulting in a well-defined and pre-organized site. The canonical CuT1 proteins plastocyanin and azurin display a deep blue color as a result of a strong electronic absorption band at 600 nm (3000 - 6000 M^{-1} cm^{-1}), a compressed EPR hyperfine coupling constant ($A_{||}$) of $< 70 \times 10^{-4}$ cm^{-1}, an unusually short Cu-S(Cys) bond of 2.1 – 2.2 Å and highly positive reduction potential (E) that has a range of 180 – 800 mV (vs. NHE). The 600 nm band was assigned to a ligand-to-metal charge transfer (LMCT) from the S(Cys)$\pi \rightarrow Cu^{2+}$ $3d_{x^2-y^2}$ charge transfer transition. Green copper centers stellacyanin and the CuT1 center in copper nitrite reductase, which have characterized as containing a perturbed blue copper center, have an additional charge transfer band at 450 nm (3000 - 6000 M^{-1} cm^{-1}) but nevertheless demonstrate similar physical properties as their blue counterparts. Nitrosocyanin, a red copper center, is a recent addition to the CuT1 family because it contains the core 2HisCys residues. It possesses that most perturbed copper site, exhibiting an inverted absorption spectrum with a λ_{max} at 390 nm (7000 M^{-1} cm^{-1}) as a result of a weak π charge transfer (CT) but intense σ CT transitions. Moreover, nitrosocyanin has large $A_{||}$ (144 x 10^{-4} cm^{-1}), a Cu-S(Cys) bond that is elongated by ~0.1 Å and a reduction potential of 84 mV (vs. NHE), all of which are the characteristics of native proteins with a type-two copper site or a "normal" copper center such as $CuCl_4$.

Protein design is a biologically relevant approach used to study the structure-function relationship of the metal centers in native proteins.[10-13] *De novo* protein design offers a novel approach in modeling the active sites of native proteins in a simplified or unrelated fold. The knowledge gained from this approach could ultimately provide greater insight into the fundamental processes of biological systems, thus allowing the possibility to produce new metalloproteins with higher stability and superior efficiency than its native counterparts. The α_3D scaffold was recently functionalized with a symmetric metal binding site to produce α_3D**IV**[14] (Figure III-I) and α_3D$\mathbf{H_3}$ (Table III-1).[15] The first derivative, α_3D**IV**, contains a symmetric 3Cys site found in native metalloregulatory proteins (MerR and ArsR) and was designed to examine the metallobiochemistry of toxic heavy metals (Cd, Hg and Pb). Moreover, the NMR structure of apo α_3D**IV** was solved to investigate the perturbation on the overall fold of α_3D as a result of incorporating a 3Cys site in place 3Leu residues that serve to stabilize the tertiary structure of the bundle.[16] The second derivative, α_3D$\mathbf{H_3}$, possesses a tris(His) site that coordinates transition metal

ions and was shown to recapitulate the catalytic reaction performed by a zinc metalloenzyme carbonic anhydrase.

This chapter describes the design process and characterization of copper metallopeptides that incorporate the asymmetric 2HisCys(Met) metal binding site of native CuT1 proteins (Figure III-2) within the α_3D scaffold. Utilizing the structure of α_3D**IV**[16] as the foundation, I designed three distinct constructs designated as α_3D-core (CR), -chelate (CH) and -chelate-core (ChC). The CR and CH chelate designs contain the asymmetric 2HisCysMet residues at the C-terminal end of the three-helix bundle, residues that make up the copper-binding site in plastocyanin, rusticyanin and azurin. I note here that the cupredoxin site in azurin contains a fifth carbonyl ligand from the backbone of the β-barrel fold, which cannot be emulated in the α-helical fold of α_3D. Next, the ChC construct incorporates 2HisCys residues that are found in plantacyanin and the CuT1 center in lacasse deeper inside the helical bundle, one layer toward the N-terminal end compared to the CR and CH constructs. My objective in this chapter is to assess if I can build a cupredoxin center that is naturally found in a β-barrel fold in the α-helical framework of α_3D and determine if the unique physical properties (e.g., absorption λ_{max} at 600 nm, compressed $A_{||}$, short Cu-S(Cys) bond and E° value > 180 mV) of such centers can be retained. In addition, these series of constructs allows for further examination of the entatic state model, as well as the inherent stability of the S(Cys)N_2(2His) ligand in an α-helical environment. Ultimately, learning how to build an electron transfer site in a *de novo* designed scaffold will provide the Pecoraro group the foundation to study long-rate ET reactions and later develop a bifunctional/bimetallic construct that contain a catalytic and an ET center, such as in copper nitrite reductase.

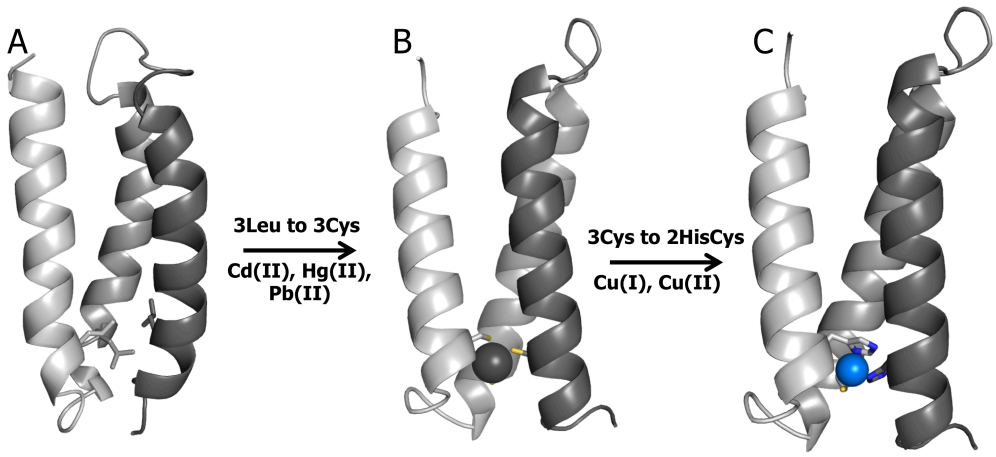

Figure III-1. *De novo* design of α_3D constructs from a heavy metal binding site to a transition metal center. A) Structure of α_3D (PDB 2A3D).[17] B) Addition of 3Cys residues to the α_3D construct, producing α_3D**IV** with a modeled mercury atom (apo α_3D**IV** PDB 2MQT).[14, 16] C) Redesign of α_3D**IV** to incorporate the core 2HisCys residues in native CuT1 proteins.

Table III-1. Amino Acid Sequence of α_3D constructs.

Peptide	Sequence abcdefg abcdefg abcdef loop	Mutations	Ligands
α_3D	MGSWAEFKQR LAAIKTR LQAL GGS EAELAAFEKE IAAFESE LQAY KGKG NPEVEALRKE AAAIRDE LQAYRHN	designed from Coil-ser[18]	
α_3D**IV**	MGSWAEFKQR LAAIKTR **C**QAL GGS EAE**C**AAFEKE IAAFESE LQAY KGKG NPEVEALRKE AAAIRDE **C**QAYRHN	α_3D**IV** + L18C, L28C, C67H	C18, C28, C67
α_3D**H$_3$**	MGSWAEFKQR LAAIKTR **H**QAL GGS EAE**H**AAFEKE IAAFESE LQAY KGKG NPEVEALRKE AAAIRDE **H**QAYR**V**N**GSGA**	α_3D**IV** + C18H, C28H, C67H, H72V+ G74, S75, G76, A77	H18, H28, H67
α_3D-CR1	MGSWAEFKQR LAAIKTR **H**QAL GGS EAE**C**AAFEKE IAAFESE LQAY KGKG NPEVEALRKE AAAIRDE **H**QAYR**M**NGSGA	α_3D**IV** + C18H, C67H, H72V + G74, S75, G76, A77	H18, C28, H67, M72
α_3D-CH3	MGSWAEFKQR LAAIKTR **H**QA**C** GGS EAE**H**AAFEKE IAAFESE LQA**F** KGKG NPEVEALRKE AAAIRDE LQA**F**R**M**NGSGA	α_3D-CR1 + L21C, C28H, Y45F, H67L, Y70F	H18, C21, H28, M72
α_3D-CH4	MGSWAEFKQR LAAIKTR **C**QA**H** GGS EAE**H**AAFEKE IAAFESE LQAF KGKG NPEVEALRKE AAAIRDE LQAFR**M**NGSGA	α_3D-CR1 + H18C, L21H, C28H, Y45F, H67L, Y70F	C18, H21, H28, M72
α_3D-ChC2	MGSWAEFKQR **I**AA**C**KTR **H**QA**L** GGS EAE**L**AA**H**EKE IAAFESE LQAF KGKG NPEVEALRKE AAAIRDE LQAFR**L**NGSGA	α_3D-CH4 + L11I, I14C, C18H, H21L, H28L, F31H, M72L	C14, H18, H31

Residues that are underlined and bolded were changed from the previous design.

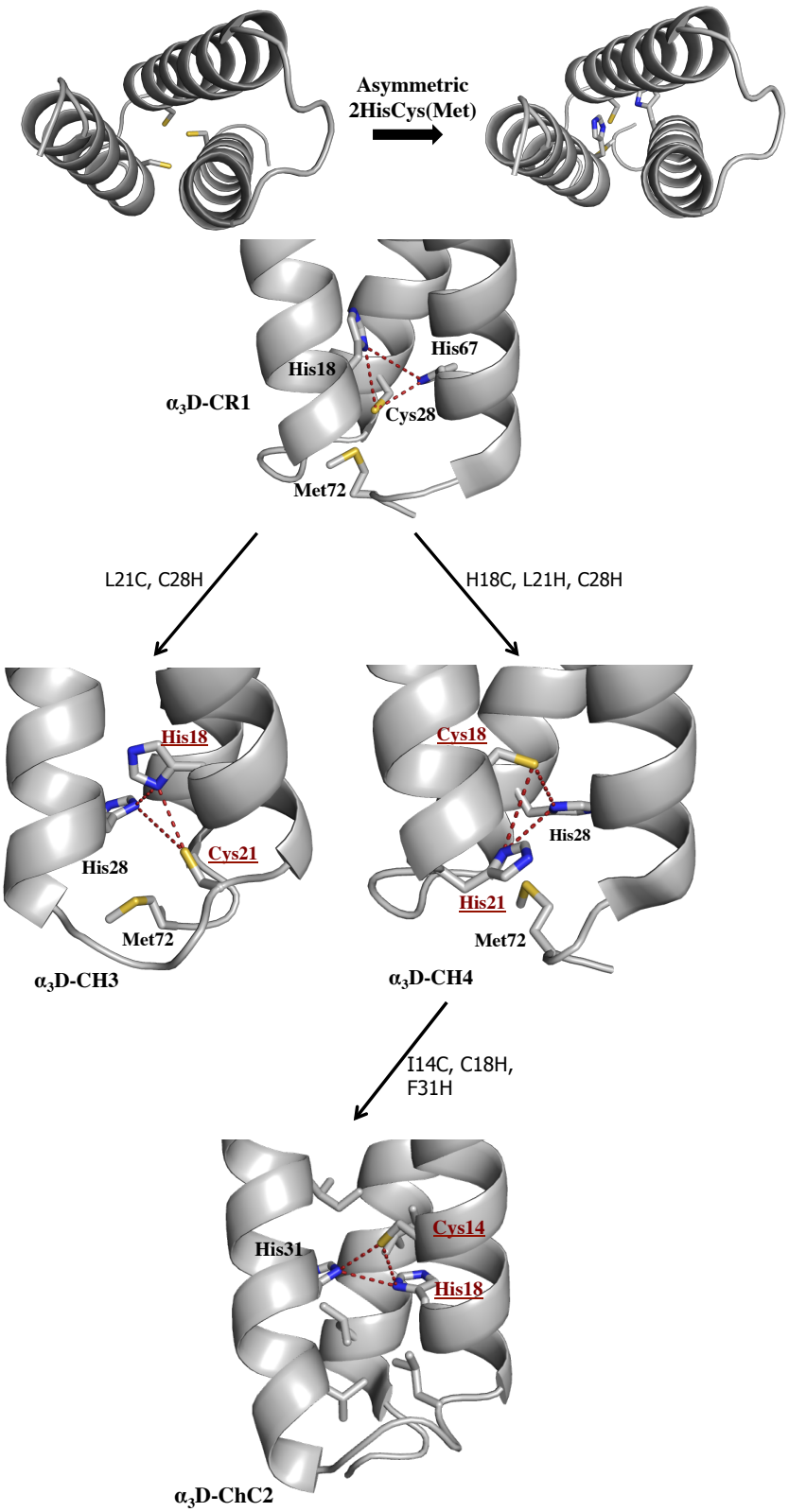

Figure III-2. Scheme representing transformation from core to chelate and chelate to chelate-core. Bolded residues indicate mutations at the metal binding site (for full mutation list see Table III-1). Bolded and underlined represent chelating residues.

Materials and Methods

Peptide Expression and Purification. A pET15B recombinant DNA plasmid that contains the gene for each construct was transformed and expressed in *E. coli* BL21(DE3) competent cells (Life Technologies). The plasmid for constructs α_3D-CR1, α_3D-CH3, α_3D-CH4 and α_3D-ChC2 were purchased from Celtek Genes. These proteins were overexpressed in self-inducing media for 18 hr, pelleted, resuspended in 1.0 mM phosphate buffer saline solution containing 2.0 mM dithiothreitol and lysed by sonication. The soluble protein was isolated after heat denaturation at 55 °C and acidification to pH 1.9. Lyophilized protein were redissolved and purified on a reversed-phase C18 HPLC using a flow rate of 20 mL/min and a linear gradient of 0.1% TFA in water to 0.1% TFA in 9:1 CH3CH:H_2O over 50 min. The purified proteins have a yield of 100 – 200 mg/L. The molecular weight is determined by ESI-MS (collected on a Micromass LCT Time-of-Flight Mass Spectrometer) and corresponds to the protein after the deletion of the N-terminal methionine residue (Table III-2). Protein concentrations were determined by measuring the absorbance at 280 nm using a determined $\varepsilon = 5650\ cm^{-1}\ M^{-1}$ (Trp) or $8215\ cm^{-1}\ M^{-1}$ (Trp and Tyr).

Table III-2. Molecular weight of CuT1 constructs.

Construct	Actual MW (Da)	Theoretical (MW)
α_3D-CR1	8282.98	8281.21
α_3D-CH3	8249.48	8249.22
α_3D-CH4	8249.21	8249.22
α_3D-ChC2	8196.37	8197.16

Circular Dichroism (CD) Spectroscopy. CD spectra were collected on an AVIV 202 CD Spectrometer at 25 °C using a 1 cm path length quartz cuvettes. Samples contained 10 mM phosphate buffer and 5 μM peptide and were prepared at pH 7.5. The mean residue ellipticities ([θ]) and percent folding was based on the presence of 55 helical residues, which was determined from the structure of α_3D**IV**, and were calculated using previously reported procedures.[19, 20] Guanidine hydrochloride (GuaHCl) titrations were performed using Microlab 500 series syringe-pump automatic titrator controlled by Aviv software. In a solution of 5 μM peptide in 10 mM phosphate buffer at pH 7.5, GuaHCl was titrated to a concentration of 5.25 M, while maintaining

the protein concentration. The change in molar ellipticity upon titration was fitted to a two-state unfolding model.[21]

Ultraviolet-Visible (UV-VIS) and Electron Paramagnetic Resonance (EPR) Spectroscopy. UV-vis spectra were recorded at 25 °C on a Cary 100 Bio UV-vis spectrometer using 1 cm path length anaerobic quartz cuvettes. X-band EPR spectra were collected on a Bruker EMX electron spin resonance spectrometer with a Varian liquid nitrogen cryostat at 77 K. For copper binding experiments, a stock solution of standardized copper chloride or copper acetate was the source of Cu(II) ions. A stock of cobalt nitrate was used in the cobalt comparative binding experiments. For copper UV-vis experiments, 50 μM of Cu(II) was added to a 100 μM apo peptide solution that contained 50 mM HEPES buffer solution. The pH of the apo solution was adjusted to 7.5. The spectrum was scanned from 800 – 300 nm every 2 minutes to track the bleaching effect caused by an autoredution reaction. The sample solutions in the cobalt UV-vis experiments were composed of 200 μM peptide, 100 μM Co(II) and 50 mM HEPES at pH 7.5. The EPR samples comprised of ~1 mM Cu(II)-peptide complex (at 1:2 Cu(II):peptide ratio), 50 mM HEPES solution and 30% glycerol. Each sample was then flashed frozen in liquid N_2. To obtain Cu(II) EPR parameters, each spectrum was simulated using SpinCount.

^{113}Cd-NMR Experiments. ^{113}Cadium(II) NMR experiments were performed on a Varian VNMRS 700 MHz equipped with a room temperature triple resonance switchable probe and were collected at 25°. ^{113}Cd(II) NMR spectra were referenced to $Cd(ClO_4)_2$, which has a literature chemical shift value of 642 ppm. The NMR parameters involved a spectral width of 96000 Hz, 5.0 μs 90° pulse and 0.05 s acquisition time with no delay between scans. Each sample was prepared by adding a small aliquot of $^{113}Cd(NO_3)_2$ (95% isotopically enriched ^{113}CdO purchased from Oak Ridge National Lab) to an apo peptide solution containing 15% D_2O/H_2O. The final solution yielded a ~1 mM ^{113}Cd-peptide (with 20% excess peptide) complex, and the pH was adjusted to 8.5 with concentrated KOH or HCl. The ^{113}Cd-NMR spectra were processed with MestreNova (version 10.0.0-14381) using a back Linear Prediction method.

Determination of Cu(I) Binding Constant. The K_d values of Cu(I) to peptide were determined using a competitive binding assay with disodium bathocuproindisulfonate (BCS) as the competitive chelator expressed by the chemical equation below:

$$Cu - Pep + 2BCS \rightleftarrows CuBCS_2 + Pep.$$

Each sample contained 25 μM of Cu(I)-pep (at a 1:2 ratio of Cu:pep) and 50 mM HEPES buffer set at pH 7.5. A small aliquot of BCS was titrated into a sample solution and mixed for 12 min. The titration experiments were completed triplicates. The formation of $CuBCS_2$ was tracked at 483 nm (ε = 13000 cm^{-1} M^{-1}), which has a $\log\beta_2$ of 19.8.[22] The binding constants were determined by fitting the Abs vs BCS concentration plots on Hyperquad 2006. This analysis fitted well to the chemical equation shown above and showed no evidence of the formation of a ternary complex.

XAS Analysis. Samples for XAS contained 1.0-2.0 mM Cu(I)-peptide complex, 50 mM buffer and 30% glycerol (prepared in an anaerobic box). Samples were loaded into lucite XAS sample cells, frozen by immersion in liquid N_2 and stored at this temperature until data collection. Data were collected at the Stanford Synchrotron Radiation Lightsource (SSRL) on beamline 7-3 with a Si(220) double-crystal monochromator, and a Rh-coated harmonic rejection mirror upstream of the monochromator with a 12 keV energy cut-off to reject harmonics. Data were measured in fluorescence mode using a high-count-rate Canberra 30-element Ge array detector, with maximum count rates held below 120 kHz per channel. A Ni filter was placed in front of the detector to reduce the elastic scatter peak and Soller slits were used to reduce the Ni Kβ fluorescence. An Oxford Instruments liquid helium cryostat was used to keep the samples below 10 K during data collection. Data were collected using 10 eV steps in the pre-edge region (8700-8950 eV), 0.25 eV for the edge (8950–9010eV) region and k=0.05 $Å^{-1}$ increments for the extended X-ray absorption fine structure (EXAFS) region to k=13.5 $Å^{-1}$. These collections had integration times of 1 s in the pre-edge and edge regions and 1-20 s (k^3 weighted) in the EXAFS region for a total scan time of ~40 min. Energies were calibrated by assigning the lowest-energy inflection point of a copper metal foil as 8980.4 eV, placed between the second (I_1) and third (I_2) ionization chamber. An initial E_0 value of 8990 eV was used to convert data to k space, and the

background was removed using a three-region cubic spline. Data from each detector channel were inspected for glitches before inclusion in the final average. For the XANES pre-edge, subtraction and normalization to McMaster[23] values were carried out using the program MBACK.[24]

Raw data were converted to EXAFS and fitted using the EXAFSPAK[25] suite of programs, with theoretical amplitude and phase parameters calculated using FEFF 9.[26] Each complex was fitted with four models: model 1 three-atom 1S(Cys)2N(His) fit, model 2 four-atom 2S2N(His) fit, model 3 four-atom SS'2N(His) fit and model 4 four-atom 1S1O2N(His) fit (see Table III-9). Imidazole outer-shell scattering was modeled and taken into account using phase and amplitude parameters calculated for an idealized $Cu(imid)_4$ structure. The imidazole Debye-Waller factors were defined by assuming that the σ^2 value for each scattering path increased proportionally from those calculated by Bunker and Dimakis for an ordered imidazole.[27] Two metal-ligand distances (R_{Cu-S}, R_{Cu-N}) and the Debye-Waller factors for the Cu-S and Cu-N shells ($\sigma^2_{Cu-S,}$ σ^2_{Cu-N}) were the only adjustable parameters, while E_0 was fixed at 0 eV for all the fits.

Results

Solution Stability of Apo Peptides. The CD spectra of the apo form of α_3D-CR1, α_3D-CH3, α_3D-CH4, and α_3D-ChC2 (at pH 7.5) were collected to examine the perturbation caused by the incorporation of bulky His residues, as well as a Cys residue on the overall fold of α_3D. As shown in Figure III-3A, each CD spectrum displays double minima bands with large negative molar ellipticity values [θ] at 208 and 222 nm, illustrating a CD profile of a well-folded α-helical scaffold.[28] The [θ] suggest that α_3D-CR1, α_3D-CH3 and α_3D-CH4 are 80 - 98% folded at pH 7.5. The same analysis performed on α_3D-ChC2, which buries the 2HisCys ligands deeper inside the bundle, reveals a protein that is ~20% less folded. Moreover, guanidine hydrochloride titration experiments (Figure III-3B) were performed to determine the Gibbs free energy of unfolding (ΔG_u) values, which were derived from a fit to a two-state unfolding model. From the shape of the denaturation curves, α_3D-CR1 and α_3D-CH3 appear to undergo a two-state transition; therefore, their chemically induced ΔG_u values are 1.4 (0.1) and 2.7 (0.5) kcal mol^{-1}, respectively

(Table III-3). α_3D-CH4 and α_3D-ChC generated broad denaturation shapes, which indicate unfolding through several intermediate states. The denaturation midpoints (C_M) were determined for all the constructs. The C_Ms of α_3D-CR1, α_3D-CH3 and α_3D-CH4 are at ~1.4 M, whereas α_3D-ChC2 has a value of 1.2 M.

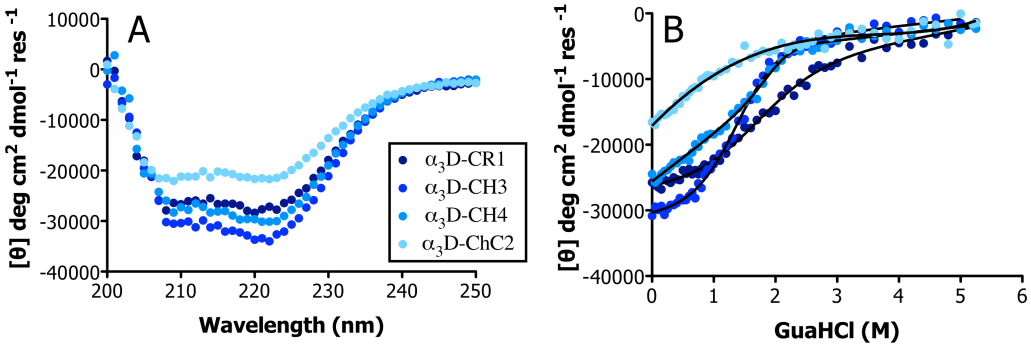

Figure III-3. Circular dichroism spectra and chemical denaturation plots of apo α_3D-CR1, α_3D-CH3, α_3D-CH4 and α_3D-ChC2. A) The CD spectra display two negative bands at 222 and 208 nm, demonstrating an α-helical structure. B) Guanidine hydrochloride denaturations were fitted to a two-state unfolding model. The shape of the denaturation curve of α_3D-CR1 and α_3D-CH3 appears to undergo a two state transition, while α_3D-CH4 and α_3D-ChC2 do not show a two-state transition.

Table III-3: Circular dichroism parameters of designed constructs.

Sample	% Folding[a]	$[\theta]_{222\,nm}/[\theta]_{208\,nm}$	C_M (M)[b]	ΔG_u[b] (kcal mol^{-1})	pH
α_3D-CR1	78 (2)	1.0	1.5 (0.1)	1.4 (0.1)	7.5
α_3D-CH3	98 (1)	1.1	1.4 (0.2)	2.7 (0.5)	7.5
α_3D-CH4	87 (1)	1.2	1.4 (0.1)	1.4 (0.1)[c]	7.5
α_3D-ChC2	63 (3)	1.0	1.2 (0.0)	1.2 (0.7)[c]	7.5
α_3D			2.8	5.1	5.0
α_3D**IV**	97		1.4	2.5	8.0
α_3D$\mathbf{H_3}$	82		1.9	3.1	9.0

All the averaged values were determined from duplicate experiments and the pH was set to 7.5. [a]Based on the presence of 55 helical residues, determined from the structure of α_3D**IV**. [b]Derived from a two-step unfolding model. [c]Does not display a two-step unfolding transition.

Characterization of Cu(II) Complexes. UV-VIS spectra were collected for the Cu(II) complex of α_3D-CR1, α_3D-CH3, α_3D-CH4 and α_3D-ChC2 (Figure III-4). This work is summarized in Table III-4. Cu(II)α_3D-CR1 displayed a CuT2 species with an LMCT absorption band at 380 nm (1565 M^{-1} cm^{-1}), a shoulder band at 550 (438 M^{-1} cm^{-1}), as well as a broad d-d like band between

600–800 nm (300 M^{-1} cm^{-1}). Cu(II)α_3D-CH3 forms a yellow copper species with an intense band at 400 nm (2619 M^{-1} cm^{-1}) and a broad band between 600–800 nm (300 M^{-1} cm^{-1}). Similarly, the Cu(II) adduct of α_3D-CH4 shows a λ_{max} at 377 nm (1840 M^{-1} cm^{-1}). This complex, however, has additional red shifted bands at 450 (1098 M^{-1} cm^{-1}) and 520 (600 M^{-1} cm^{-1}) nm, which could indicate slight weakening of the interaction between the S(Cys)σ and Cu $3d_{x^2-y^2}$ orbitals., Cu(II)α_3D-ChC2 exhibited two distinct intense LMCT bands at 401 nm (4429 M^{-1} cm^{-1}) and 499 (2020 M^{-1} cm^{-1}), which demonstrates that interaction between S(Cys)π and Cu $3d_{x^2-y^2}$ orbitals increased compared to Cu(II)α_3D-CH4. This complex formed a brown-orange copper species in solution (Figure III-5), which has been previously observed in the Met to Glu mutant of azurin[29] and rusticyanin.[30]

The Cu(II) adduct of α_3D-CR1, α_3D-CH3, α_3D-CH4 and α_3D-ChC2 has an R_ε value of 3.6, 11.9, 3.3 and 2.2, respectively. The R_ε value is widely used to categorize native and designed CuT1 centers and determined from the ratio of the molar extinction coefficient at ~400 (± 50) and ~600 nm (± 50). This value signifies the deviation from a trigonal pyramidal to a tetrahedral or tetragonal/square planar geometry: blue and green copper centers have an R_ε value < 0.1 (trigonal pyramidal) and 0.1 – 0.6 (pseudotetrahedral), respectively, while CuT2 centers such as nitrosocyanin have a ratio > 1.0 (tetragonal). The R_ε values for the designed constructs were derived from their λ_{max} (377 – 400 nm) and a second band between 500 – 550 nm. Moreover, upon the addition of Cu(II), the absorption profile of each complex faded, which had varying life time. This bleaching effect is due to a redox reaction between the copper and S(Cys) ligand, which reduces the Cu(II) ion.[31-33] The spectrum of Cu(II)α_3D-CR1 and Cu(II)α_3D-CH4 bleached after 10 min, while the Cu(II)α_3D-CH3 species slowly faded in a 4 hr time span, demonstrating a more stable Cu(II)-S(Cys) bond. The spectrum of Cu(II)α_3D-ChC2 persisted for ~15 hr, exhibiting the most stable Cu(II)-S(Cys) bond of the designed constructs. Overall, the Cu(II) absorption profile of the chelate-core construct indicates a significant perturbation of the tetragonal complex that forms in the core and chelate designs.

A copper EPR spectrum was collected for Cu(II)α_3D-CR1, Cu(II)α_3D-CH3, Cu(II)α_3D-CH4 and Cu(II)α_3D-ChC2 (Figure III-4B). The EPR parameters from the simulation are listed in

Table III-5. Each complex displayed an axial EPR spectrum and $g_{\parallel} > g_{\perp} > 2.0023$, which signifies a Cu(II) $3d_{x^2-y^2}$ ground state. The hyperfine coupling constants of each complex are comparable to the corresponding A_{II} for nitrosocyanin and CuT2 centers, with values greater than >100 x 10^{-4} cm^{-1}. Cu(II)α_3D-CR1, Cu(II)α_3D-CH3 and Cu(II)α_3D-CH4 have A_{II} values that range from 152 –185 x 10^{-4} cm^{-1}. Cu(II)α_3D-ChC2 has the respective value of 130 x10^{-4} cm^{-1}.

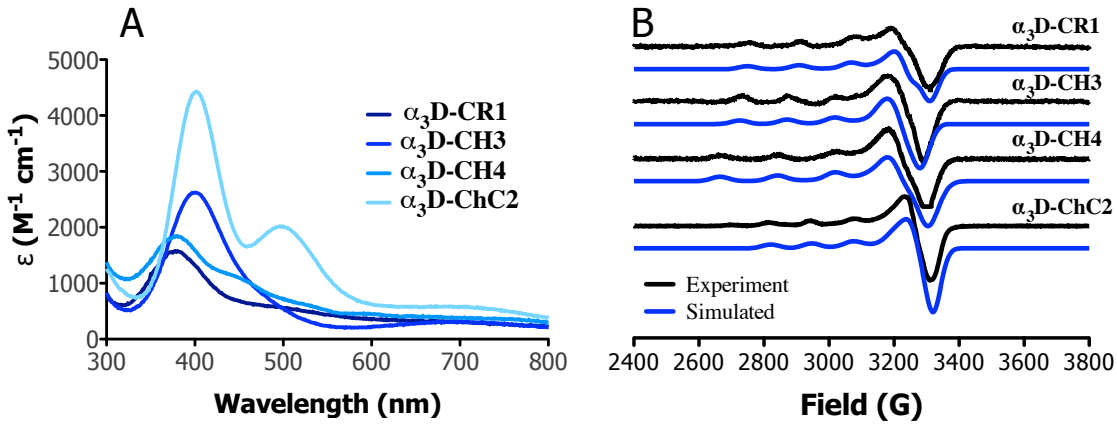

Figure III-4. Overlay of Cu(II) UV-VIS (A) and EPR (B) of designed constructs. Each EPR spectrum is aligned with their corresponding simulated spectrum.

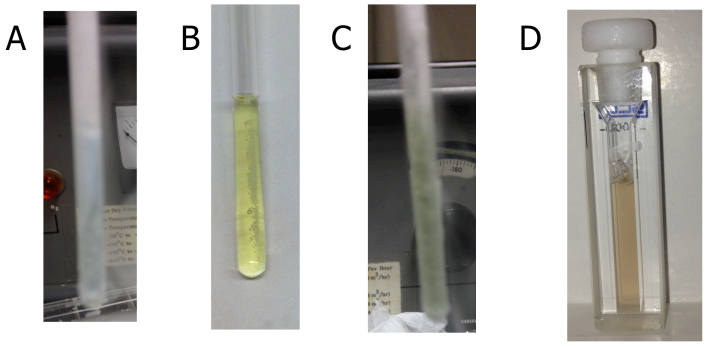

Figure III-5. Color of the Cu(II) species of designed constructs: (A-C): EPR sample of (A) α_3D-CR1, (B) α_3D-CH3 and (C) α_3D-CH4 (C) containing 1 mM Cu(II)Peptide complex at pH 7.5. (D) UV-vis sample of Cu(II)α_3D-ChC containing 50 uM Cu(II)Peptide complex at pH 7.5.

Table III-4. Absorption features of designed constructs.

Cu(II) Complex	λ nm (ε_λ M^{-1} cm^{-1})	R_ε	Half-life (min)
α_3D-CR1	380 (1565), 550 (438), 600 – 800 (300)	3.6 ε380 nm/ ε550 nm	~4.0
α_3D-CH3	400 (2619), 600- 800 (300)	11.9 ε400 nm/ ε550 nm	~130
α_3D-CH4	377 (1840), 450 (1098), 520 (600), 600 – 700 (380)	3.3 ε377 nm/ ε540 nm	~5
α_3D-ChC2	401 (4429), 499 (2020), 600 – 800 (550)	2.2 ε401 nm / ε499 nm	~460
Blue Copper Plastocyanin	460 (300), 597 (5200)	0.06 ε460 nm / ε597 nm	
Green Copper: Stellacyanin	448 (1150), 604 (4000)	0.30 ε448nm / ε604 nm	
Red Copper: Nitrosocyanin	390 (7000), 550 (2200)	3.20 ε390nm / ε550 nm	

Table III-5. EPR Parameters of designed constructs.

Cu(II) Complex	$A_{\|\|}$ (cm^{-1})	g_x, g_y, g_z
α_3D-CR1	163 x 10^{-4}	2.05, 2.05, 2.21 axial
α_3D-CH3	152 x 10^{-4}	2.04, 2.04, 2.24 axial
α_3D-CH4	185 x 10^{-4}	2.04, 2.04, 2.25 axial
α_3D-ChC2	130 x 10^{-4}	2.03, 2.03, 2.21 axial
Blue Copper plastocyanin	63 x 10^{-4}	2.05, 2.05. 2.23 axial
Green Copper: stellacyanin	36 x 10^{-4}	2.09, 2.02. 2.29 rhombic
Red Copper: nitrosocyanin	144 x 10^{-4}	2.02, 2.07, 2.25 axial

Comparative Metal-Binding Studies. Cobalt(II) and Cd(II) binding experiments were performed to probe the coordination environment of selected constructs further. A Co(II) UV-VIS spectrum

was obtained for α_3D-CR1, α_3D-CH3, α_3D-CH4, and α_3D-ChC2 at pH 7.5 (Figure III-6A). These spectra display maxima between 290 – 309 nm with molar extinction coefficients (ε) that range from 757 – 3743 M^{-1} cm^{-1} (Table III-6). These absorption features are indicative of a sulfur-to-Co(II) LMCT.[34, 35] With the exception of α_3D-CH4, three *d-d* transitions between 540 - 675 nm are observed in each spectrum, and the energies and intensities of these bands corroborate well with a four-coordinate environment.[36] Cobalt bound α_3D-CH4 displays one broad *d-d* band that signifies a higher coordination number (5-6).

To further confirm metal binding to the 2HisCys(Met) sites, ^{113}Cd-NMR spectra were collected for α_3D-CR1, α_3D-CH3 and α_3D-ChC2 (Figure III-6B). The ^{113}Cd nuclei is highly sensitive to its ligand field environment and has been widely used to probe the binding site of native metalloproteins.[37, 38] The ^{113}Cd-NMR spectrum of α_3D-CR1 and α_3D-CH3 displayed two resonance signals at 320 and 363 ppm and 344 and 369 ppm, respectively. Contrary, ^{113}Cd(II)α_3D-ChC2 exhibited a single resonance signal at 336 ppm. These results revealed that both α_3D-CR1 and α_3D-CH3 form two Cd(II) complexes in solution, whereas α_3D-ChC2 produces one species. Nevertheless, the species with a chemical shift between 300-340 ppm suggest a Cd(II) ion bound to at least a N_2S ligand set, while values at ~360 ppm indicates an addition of an S(Met) (S^*) and/or an O atom (from a water molecule or the peptide) ligand to yield an N_2SS^*O environment.[38] These chemical shift values are compared to cadmium-substituted native cupredoxins in Table III-6.

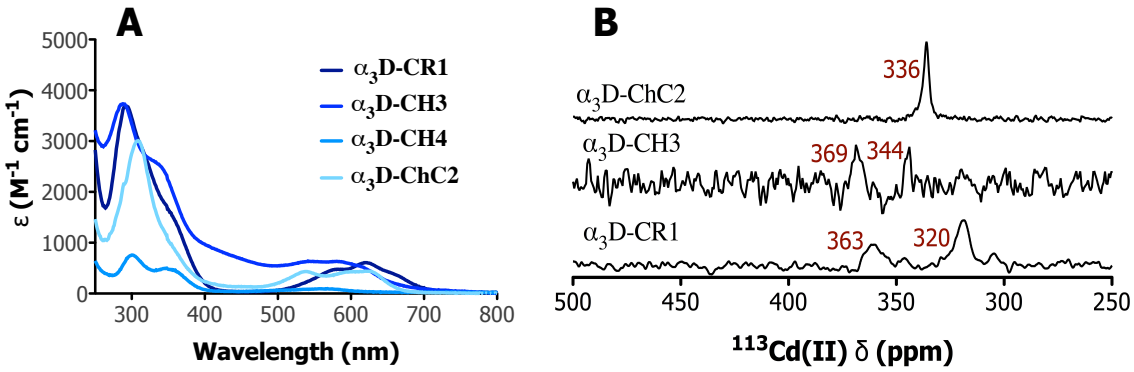

Figure III-6. A) Cobalt spectra of designed constructs. B) ^{113}Cd-NMR spectra of selected constructs.

Table III-6. Comparative metal binding results.

Construct	Co (II) UV/VIS λ nm ($\Delta\varepsilon_\lambda$ M^{-1} cm^{-1})	^{113}Cd-NMR δ (ppm)
α_3D-CR1	294 (3681), 320 (2652sh), 360 (1420sh), 583 (479), 622 (609), 675 (265)	320, 363
α_3D-CH3	290 (3743), 340 (2502sh), 541 (638), 580 (635), 630 (411)	344, 369
α_3D-CH4	300 (757), 358 (479), 573 (92)	
α_3D-ChC2	309 (3010), 539 (433), 600 (430), 620 (440)	336
Blue Copper: Plastocyanin	333 (2750), 385 (sh), 430 (sh), 508 (480), 650 (sh), 673 (480)[34, 35]	432[37, 38]
Blue Copper: Azurin	330 (2400), 375 (sh), 405 (1000), 522 (~300), 638, 645 (sh) (~400)[34, 35]	372-379[37, 38]
Green Copper: Stellacyanin	310 (sh), 365 (2000), 540 (300), 625 (450), 655 (450)[34, 35]	380[37, 38]

Characterization of Cu(I) Complexes. The binding constant and metrical parameters of Cu(I) adducts were correspondingly determined by a competition assay and X-ray absorption Spectroscopy (XAS). The Cu(I) dissociation constants (K_d) of α_3D-CR1, α_3D-CH3, α_3D-CH4 and α_3D-ChC2 were determined from a competition assay that utilized chelating agent bathocuproindisulfonate (BCS) ($CuBCS_2$: log β_2 = 19.8 and $\varepsilon_{483\ nm}$ = 13000 cm^{-1} M^{-1}).[22] This competition study produced K_d values of 10^{-14} – 10^{-17} M (Table III-7). Construct α_3D-CH4 has the largest K_d value of 1.13 (0.21) x 10^{-14} M. α_3D-CH3 and α_3D-ChC2 yielded K_d values that are within the same magnitude, 3.04 (0.68) x 10^{-15} and 2.02 (0.68) x 10^{-15} M, respectively. α_3D-CR1 formed the strongest complex and has a K_d value of 3.90 (2.33) x 10^{-16} M. The corresponding spectra and titration plots are shown in Figure III-7.

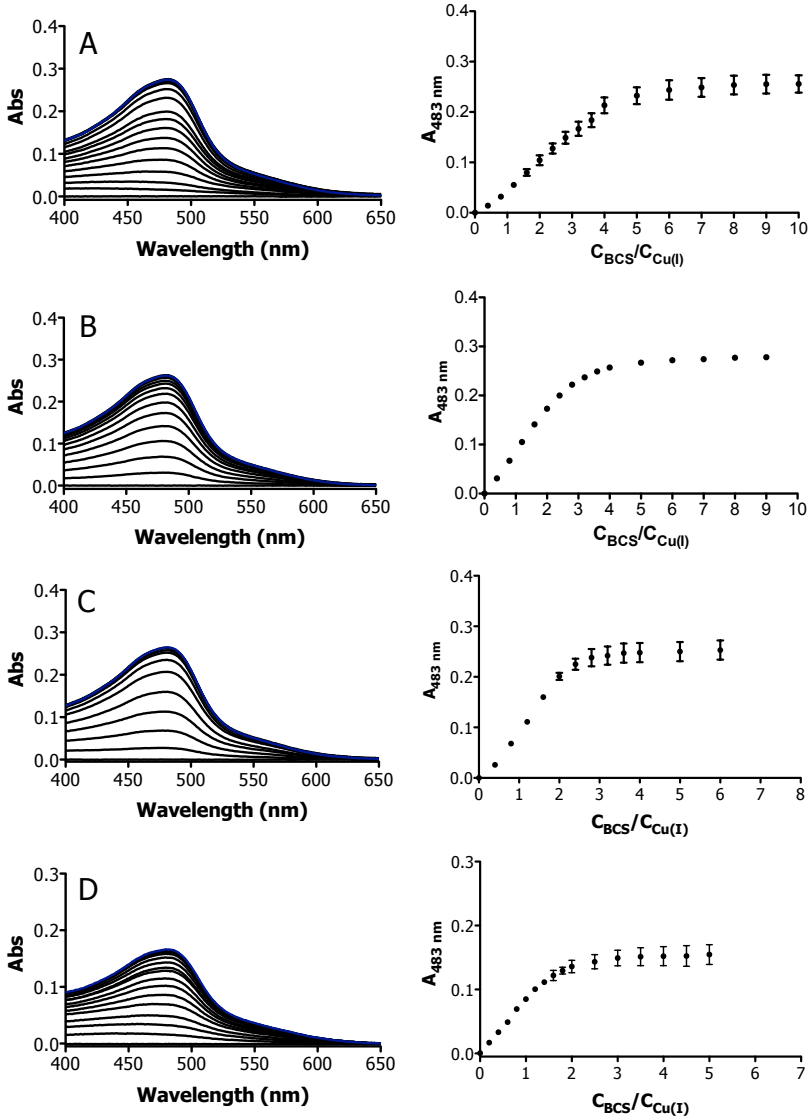

Figure III-7. Representative spectra for Cu(I) binding to designed constructs and titration curve. (A) α_3D-CR1. (B) α_3D-CH3. (C) α_3D-CH4. (D) α_3D-ChC2. Visible spectra for the titration of a solution containing Cu(I) (25 μM) and peptide (50 μM) and with sodium bathocuproine disulfonate (Na_2BCS) in H_2O (50 mM buffer HEPS, pH 7.5). The blue line in each spectrum represents the final addition of Na_2BCS.

Table III-7. Cu(I) binding constants of designed constructs.

Constuct	pH	K_d (M)
α_3D-CR1[a]	7.5	3.90 (2.33) x 10^{-16}
α_3D-CH3[a]	7.5	3.04 (0.68) x 10^{-15}
α_3D-CH4[a]	7.5	1.13 (0.21) x 10^{-14}
α_3D-ChC2[b]	7.5	2.02 (0.03) x 10^{-15}

[a]50 μM peptide, 25 μM Cu(I). [b]30 μM peptide, 15 μM Cu(I).

To further assess copper binding to the designed metal binding sites, the Cu(I) complexes of α_3D-CR1, α_3D-CH3, α_3D-CH4 and α_3D-ChC2 were analyzed by XAS. The X-ray absorption near edge structure (XANES) spectrum (Figure III-8) is consistent with those typically observed for a Cu(I) complex, exhibiting a Cu(I) pre-edge peak at ~8,984 eV that is attributed to 1s→4p transition.[39] The relative intense transition for Cu(I)α_3D-CR1 and Cu(I)α_3D-ChC2 is consistent with a three-coordinate species,[40] while the lower intensity for Cu(I)α_3D-CH3 and Cu(I)α_3D-CH4 suggests a four-coordinate geometry. Subsequently, an Extended X-ray Absorption Fine Structure (EXAFS) analysis was performed to obtain metrical parameters on the Cu(I) species (Table III-8). Each adduct was fitted to four models: CuN_2S (model 1), CuN_2S_2 (model 2), CuN_2SS (model 3) and CuN_2SO (model 4). The fits of all the samples have similar EXAFS spectra, with Fourier Transformed plots that are dominated by a single intense peak at R ~2 Å (Figure III-9) from a heavy scatterer such a sulfur atom. Each EXAFS spectrum display a weak outer-shell scattering pattern, which is consistent with multiple scattering from a His residue.

The Cu(I) adducts could be fit to a Cu–S and Cu–N scattering environment at ~2.2 Å and ~2.0 Å, respectively. The fitted Cu-nearest-neighbor distances vary as expected, given the apparent coordination numbers of 3 for Cu(I)α_3D-CR1 and Cu(I)α_3D-ChC2 and 4 for Cu(I)α_3D-CH3 and Cu(I)α_3D-CH4. The three-coordinate fits produced Cu-S(Cys) and Cu-2N(His) bond lengths at 2.16–2.18 Å and 1.92 Å, respectively. The four-coordinate fits yielded Cu-2S and Cu-2N(His) distances of 2.20–2.23 Å and 1.95–1.99 Å, respectively. Although some of the samples could be fit with a third scatters (either Cu-S or Cu-O) these models did improve in the fit quality and resulted in chemically unlikely distances and Debye-Waller factors (σ^2) (Table III-9). For instance, the best fits for Cu(I)α_3D-CH3 and Cu(I)α_3D-CH4 were obtained with a shell of two S atoms and Debye-Waller factor of 3–4 x 10^{-3} Å^2. In contrast, attempts to fit these data with only a single S atom resulted in high F values and small Debye-Waller factors (~2 x 10^{-4} Å^2). The opposite trend was observed for Cu(I)α_3D-CR1 and Cu(I)α_3D-ChC2. The best fits were obtained using a single Cu-S, and these fits produced reasonable Debye-Waller factors of 3–4 x 10^{-3} Å^2. Overall, the EXAFS analysis is consistent with the change in coordination number that is indicated by the XANES as a consequence of an additional S atom. The second S atom is predicted to originate from S(Met72) ligand. Even though these distances are ~0.6 Å shorter than

what is observed in the X-ray crystal structures of native cupredoxins, Cu(I)-thioether bonds at 2.20 Å have been measured in small molecule compounds (Table III-10).

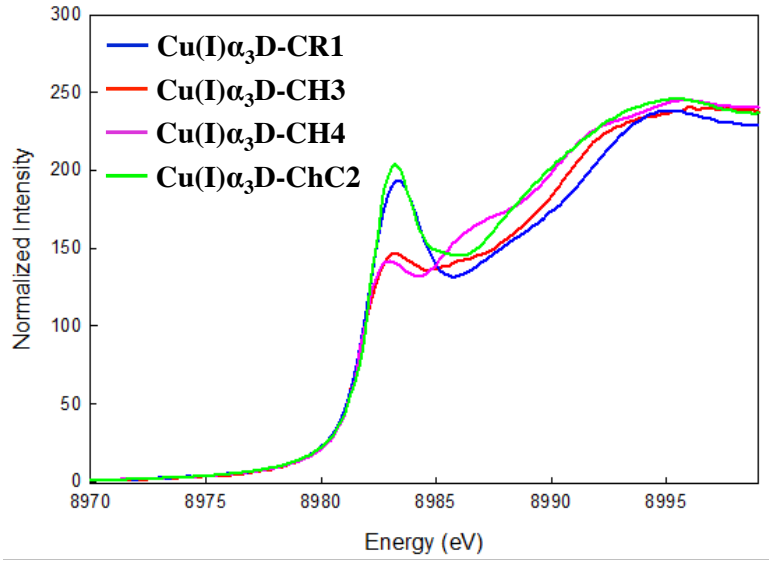

Figure III-8. Comparison of the XANES plot of Cu(I)α_3D-CR1 (blue), Cu(I)α_3D-CH3 (red), Cu(I)α_3D-Cu(I)CH4 (purple) and Cu(I)α_3D-ChC2 (green). In each plot, a resolved peak at ~8,984 eV is observed that is attributed to a Cu(I) 1s→4p transition.[39]

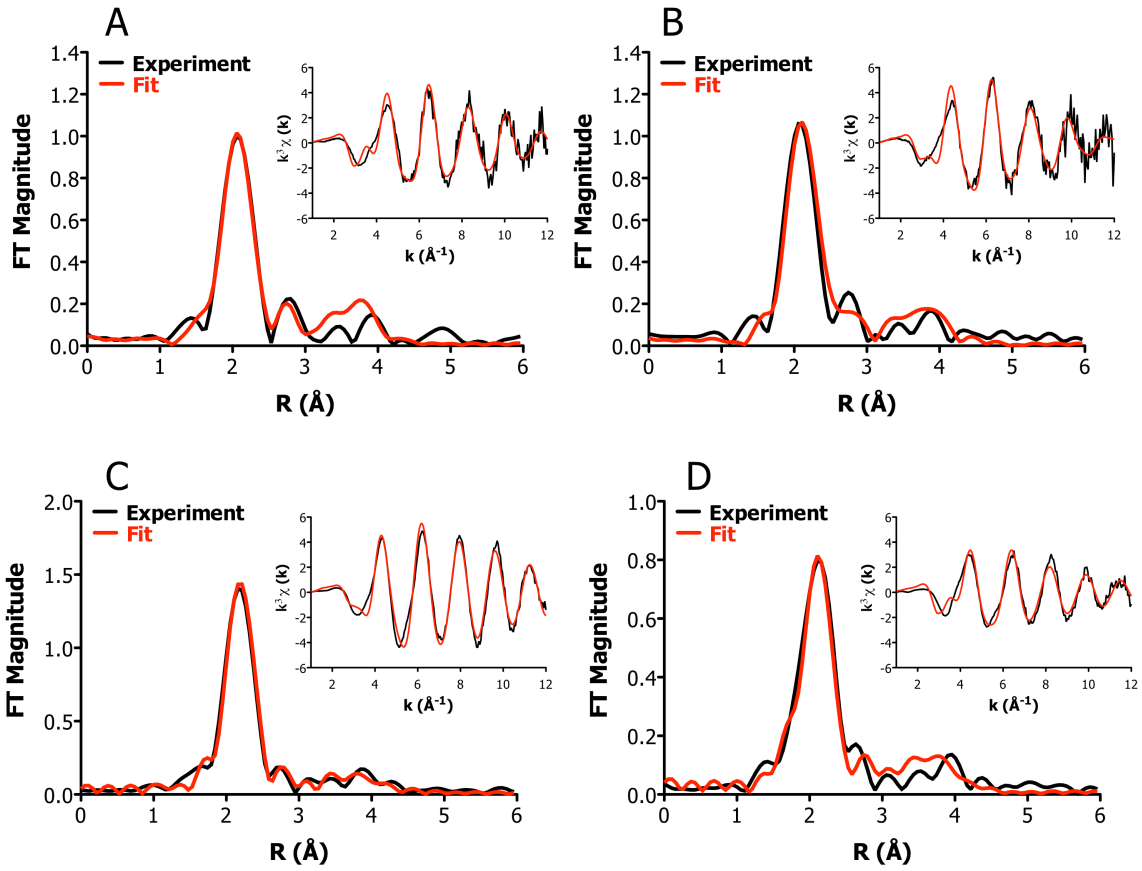

Figure III-9. EXAFS (as insets) and Fourier transform plot of Cu(I)α_3D-CR1 (A), Cu(I)α_3D-ChC2 (B), Cu(I)α_3D-CH3 (C) and Cu(I)α_3D-CH4 (D). These plots represent the best model for each Cu(I) complex: a three-atom fit for Cu(I)α_3D-CR1 and Cu(I)α_3D-ChC2 and a four-atom fit for Cu(I)α_3D-CH3 and Cu(I)α_3D-CH4.

Table III-8. EXAFS fitting parameters[a] of Cu(I) complexes.

Protein	Model	Cu-S		Cu-N		F	pH
		R (Å)	σ^2 (Å^2)	R (Å)	σ^2 (Å^2)		
α_3D-CR1	1	2.16	0.0034	1.92	0.0091	112	7.5
α_3D-CH3	2	2.20	0.0031	1.95	0.0074	143	7.5
α_3D-CH4	2	2.23	0.0039	1.99	0.0137	70	7.5
α_3D-ChC2	1	2.18	0.0042	1.92	0.0154	68	7.5
P. Aeruginosa azurin[41]		2.21	0.0031	2.00	0.0040		5.5
C. Sativus stellacyanin[42]		2.22	0.0016	2.02	0.0015		5.5
N. europea nitrosocyanin[43]		2.28	0.0005	1.96	0.0004		7.0

[a]N (number of scatter), R (distance), σ^2 (Debye-Waller factor) and F (goodness of fit).

Table III-9. Complete metrical parameters[a] from EXAFS analysis.

		α_3D-CR1		α_3D-CH3		α_3D-CH4		α_3D-ChC2	
Model 1: CN 3									
Cu(I)–X	N	R (Å)	σ^2 (Å^2)	R (Å)	σ^2 (Å^2)	R (Å)	σ^2 (Å^2)	R (Å)	σ^2 (Å^2)
Cu–SCys	1	2.16	0.0034	2.20	0.0008	2.23	0.0002	2.18	0.0042
Cu–NHis	2	1.92	0.0091	1.97	0.0089	1.99	0.0097	1.92	0.0154
Cu–C2/C5His	2	2.90	0.0131	2.98	0.0127	2.83	0.0140	2.90	0.0223
Cu–C2/C5His	2	2.93	0.0131	3.02	0.0127	2.86	0.0140	2.94	0.0223
Cu–N–C2/C5His	4	3.06	0.0112	3.15	0.0109	2.99	0.0120	3.06	0.0190
		F		F		F		F	
		112		175		172		68	
Model 2: CN 4									
Cu–SCy	2	2.15	0.0079	2.20	0.0031	2.23	0.0039	2.18	0.0085
Cu–NHis	2	1.95	0.0140	1.95	0.0074	1.99	0.0137	2.00	0.0303
Cu–C2/C5His	2	2.95	0.0202	2.95	0.0107	3.01	0.0197	3.02	0.0437
Cu–C2/C5His	2	2.98	0.0202	2.98	0.0107	3.04	0.0197	3.06	0.0438
Cu–N–C2/C5His	4	3.11	0.0173	3.11	0.0091	3.18	0.0169	3.19	0.0374
		F		F		F		F	
		150		143		70		94	
Model 3: CN 4									
Cu–SCys	1	2.16	0.0034	2.20	0.0031	2.22	0.0028	2.18	0.0043
Cu–S	1	3.24	0.0225	2.95	3.3701	2.23	0.0050	2.33	0.0355
Cu–NHis	2	1.92	0.0089	1.95	0.0074	1.99	0.0152	1.93	0.0187
Cu–C2/C5His	2	2.90	0.0128	2.95	0.0106	3.00	0.0220	2.91	0.0270
Cu–C2/C5His	2	2.93	0.0128	2.99	0.0107	3.04	0.0220	2.95	0.0270
Cu–N–C2/C5His	4								
		F		F		F		F	
		103		143		70		63	
Model 4: CN 4									
Cu–SCys	1	2.16	0.0034	2.21	0.0029			2.18	0.0041
Cu–NHis	2	1.92	0.0099	1.95	0.0072			1.91	0.0136
Cu–O	1	2.89	0.0057	2.83	0.0393			2.70	0.0031
Cu–C2/C5His	2	2.90	0.0143	2.95	0.0103			2.89	0.0195
Cu–C2/C5His	2	2.94	0.0143	2.98	0.0103			2.93	0.0195
		F		F				F	
		100		149				40	

[a]N (number of scatter), R (distance), σ^2 (Debye-Waller factor) and F (goodness of Fit).

Table III-10. Metrical parameters of Cu(I)-N_2SR_2 model compounds.

Compound	Refcode	Cu-N1 R (Å)	Cu-N2 R (Å)	Cu-S R (Å)
tetrakis(μ_2-N-(2- Isopropyl-6-((methylthio)methyl)phenyl)- N'-(2,6-di-isopropylphenyl)pentane-2,4- di-imidato-N,N',S)-tetra-copper(i)[44]	LEJDEK	1.953	1.928	2.164
hexakis(μ_2-1,1'-((2-(phenylsulfanyl)phenyl)methylene)bis(3, 5-dimethyl-1H-pyrazole))-hexa-copper(i) hexakis(tetrafluoroborate) dichloromethane solvate[45]	NEDSUM	1.977	2.007	2.164
bis(μ_2-2-(1-(3,5- diisopropyl-1H-pyrazol-1-yl)-3-(methylthio)propyl)-4-methoxy-3,5- dimethylpyridine)-di-copper(i) bis(tetrafluoroborate) tetrahydrofuran solvate[46]	TUGQOC	1.993	2.011	2.177
(5-(2-(pyridin-2-yl)ethyl)-1,5-thiazocane)-copper hexafluorophosphate[47]	GIXXOC	2.166	1.930	2.203
(26,28-bis(2-(Methylthio)ethoxy)-25,27-bis((1-methylimidazol-2-yl)methoxy)-5, 11,17,23-tetra-t-butylcalix(4)arene)- copper(i) hexafluorophosphate acetonitrile solvate[48]	ARAFOO	1.938	1.939	2.288
Average M-L		2.005 (0.092)	1.963 (0.042)	2.199 (0.052)

The M-L bond lengths represent one complex within a network.

Discussion

The well-defined fold of α_3D provides a novel *de novo* designed framework for further examining the unique copper site of native cupredoxins. The Pecoraro group have previously incorporated a thiol rich site within the α_3D scaffold to generate α_3D**IV** and demonstrated heavy metal binding (Cd, Hg and Pb).[14] As described in Chapter 2, I then solved the NMR structure of apo α_3D**IV** (PDB 2MQT), which showed that the α_3D fold is amenable to the incorporation of a metal binding site.[16] Subsequently, a second α_3D derivative, α_3D$\mathbf{H_3}$, was prepared to include a tris(histidine) metal binding site for zinc.[15] α_3D$\mathbf{H_3}$ was shown to catalyze the reversible interconversion between CO_2 and HCO_3^- performed by native carbonic anhydrase (CA) and is

only 11-fold slower than native CAIII. After establishing that the α_3D scaffold can accommodate cysteine ligands bound to a heavy metal and bulky His ligands that can coordinate a transition metal, here, I designed α_3D constructs that encompasses the asymmetric 2HisCys metal binding site of CuT1 centers (Figure III-12). The preassembled fold of α_3D provides a more direct incorporation of a mixed-ligand/asymmetric metal center, which has been challenge in current *de novo* designed scaffolds. This work allows for the investigation of whether the unique spectroscopic and structural properties of native CuT1 proteins can be retained in an unrelated α-helical fold and the knowledge gained from this work will lead to future ET studies.

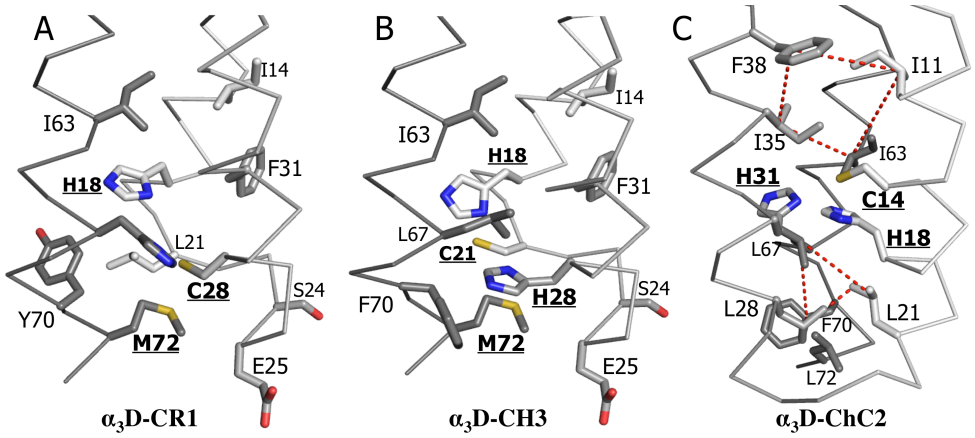

Figure III-10. A core (A), chelate (B) and chelate-core (B) CuT1 models based on the α_3D**IV** structure (varying shades of gray signify different α-helical strands). The 2His, Cys and/or Met ligands are bolded and underlined. Hydrophobic (I, L, F and Y) residues and possible competing ligands S24 and E25 are also labeled. A) α_3D-CR1 contains N_2SS^* ligands at the C-terminal end of the bundle, at positions 18, 67, 28 and 72. B) Chelate construct α_3D-CH3 possesses a His-X_2-Cys chelating motif at the 18th and 21st position, respectively, as well as the second His ligand at the 28th and Met ligand at the 72nd position. These ligands are also located at the C-terminal end. C) α_3D-ChC2, a chelate-core construct, N_2S CuT1 ligands are translated one layer above the prior two constructs towards the N-terminal end. This construct contains a C14-X_3-H18 chelating motif and a second His ligand at the 31st position, which are capped by hydrophobic planes (as indicated by the red dashed squares).

α_3D-CR1 incorporates the 2HisCys residues on three separate strands, at positions 18, 28 and 67, and a Met residue at position 72 (Figure III-10A). With the exception of Met72, this metal binding site mirrors the 3Cys positions in α_3D**IV**. The absorption spectrum of Cu(II)α_3D-CR1 exhibited the absorption features of CuT2 site with a λ_{max} at 380 nm (1565 $M^{-1}cm^{-1}$) and broad

d-d like bands between 600-700 nm (300 M^{-1} cm^{-1}). The EPR hyperfine coupling constant of this complex is ~60 x 10^{-4} cm^{-1} greater and R_ε value ($\varepsilon_{380\ nm}/\varepsilon_{550\ nm}$) ~4 times higher than the corresponding parameters for green copper sites.. The Cu(II) UV-VIS results of the α_3D-CR1 constructs closely match the spectral properties of a "normal" copper or CuT2 center and the cysteinated CuT2 site in CuZnSOD[49] and Bsco.[33] The strong absorption band at ~380 nm that dominates much of the spectrum of α_3D-CR1 stems from a S(Cys)σ → Cu $3d_{x^2-y^2}$LMCT. Moreover, as a result of the Jahn-Teller effect, it was determined that the Cu(II) ion in CuT2 centers dictates the geometry of the complex by establishing its preferred tetragonal or square planar geometry, instead of the characteristic trigonal pyramidal or distorted tetrahedral geometry observed in CuT1 sites enforced by the protein fold.[8, 50] Overall, the spectral properties of Cu(II) bound to α_3D-CR1 and the autoreduction reactions that are caused by an unstable Cu(II)-S(Cys) bond revealed that the metal binding site in such construct is not adequately well-formed to deter a tetragonal Cu(II) complex from forming.

The design concept of the second constructs was by inspired the L–X_n–L (L= His or Cys, n = #nonligating residues) chelate motif found in the loop regions of zinc finger proteins, as well as cupredoxins. CH constructs α_3D-CH3 and α_3D-CH4 possess a Cys–X_2–His chelate motif at end of helix 1, at positions 18 and 21, as well His 28 and Met 72 (Figure III-10B). Compared to the CR construct, the chelate group was designed to provide a strong Cys–Cu–His bond and requires one additional helix to provide the second His ligand. The 21st position, which is the first residue in loop 1, was chosen because the apolar group of Leu 21 in the α_3D**IV** structure is oriented towards the N-terminal end of bundle. Replacing Leu 21 with a Cys or His residue could provide an analogous rotamer. α_3D-CH3 has a His18–X_2–Cys21 chelate group, and α_3D-CH4 contains an inverted arrangement of this group (Cys18–X_2–His) and translates the Cys residue three positions towards the N-terminal end. In addition, Tyr45/70Phe substitutions were performed on both constructs to serve as a hydrophobic capping element, which could deter access by water molecules or competing ligands.

Even though both complexes generated spectra comparable to CuT2 centers, the absorption profile of Cu(II)α_3D-CH3 and Cu(II)α_3D-CH4 are distinctive. The Cu(II)α_3D-CH3 complex

formed a yellow tetragonal species, exhibiting an intense S(Cys)σ → Cu $3d_{x^2-y^2}$ transition at 400 nm (2619 $M^{-1}cm^{-1}$) and a broad band between 600 – 800 nm (300 $M^{-1}cm^{-1}$), as well as an R_ε value of 11.9 ($\varepsilon_{400\ nm}/\varepsilon_{550\ nm}$). Cu(II)$\alpha_3$D-CH4 also displayed a λ_{max} towards the UV range at 377 (1840 M^{-1} cm^{-1}). However, the inverted chelate group of α_3D-CH4 exhibited additional absorption bands at 450 and 520 nm and an R_ε value ($\varepsilon_{400\ nm}/\varepsilon_{540\ nm}$) that is 4 times lower than α_3D-CH3. Moreover, this complex formed a green color at a high concentration, revealing the additional transitions in the visible range (Figure III-5C). Unexpectedly, the $A_{||}$ value of Cu(II)α_3D-CH4 is ~30 x 10^{-4} cm^{-1} greater than the equivalent parameter of Cu(II)α_3D-CH3, yet both values are still within the range of CuT2 centers (>100 x 10^{-4} cm^{-1}). Overall, even though the Cu(II) complex of α_3D-CH3 and α_3D-CH4 displayed UV-VIS spectra that are indicative of tetragonal CuT2 species, the Cys/His18-X_2-Cys/His21 chelate group has a noteworthy effect on Cu(II) binding. The additional bands in the spectrum of α_3D-CH4 could signify a weakening of the interaction between the S(Cys)σ and Cu $3d_{x^2-y^2}$ orbital, perhaps as a consequence of placing the Cys residue closer to the hydrophobic core of the bundle. In terms of the α_3D-CH3 construct, the Cu(II) complex does not rapidly undergo an autoreduction reaction and can persevere for ~4 hr. This observation demonstrates that the chelate group in α_3D-CH3 is able to form a more stable Cu(II)-S(Cys) bond compared to α_3D-CR1 and α_3D-CH4.

The Cu(II) binding results revealed that the metal binding site of the core and chelate constructs was insufficient in forcing the Cu(II) to form an entatic state. That is, the Cu(II) ion is dictating the coordination environment by forming its preferred tetragonal complex. To improve on these previous results, the third construct was designed to incorporate a chelate group within the core of the α_3D scaffold, with the intention of constraining the metal binding site through steric interactions. From NMR studies, DeGrado and coworkers observed that the aromatic groups of Trp4, Phe7 and Tyr45 forced the methyl groups of Leu42, Val53 and Leu56 in an ordered and less dynamic state.[51] To achieve more control, we encapsulated the metal binding site of α_3D-ChC2 inside a hydrophobic box that could provide analogous steric pressure on the 2HisCys residues. The overall objective was to allow the protein environment to dictate the geometry of the copper complexes and deter the formation of a tetragonal species. The hydrophobic box comprises a plane formed by Leu21, Leu28, Leu67 and Phe70 at the C-terminal and Ile11, Ile25, Phe38 and Ile63 at the N-terminal end (Figure III-10C). α_3D-ChC2 possesses a

Cys14-X_3-His18 chelate motif, as well as His 31, modeling the metal binding site of plantacyanin and the CuT1 site in lacasse. In essence, α_3D-ChC2 contains the respective metal binding site of α_3D-CH4, translated one layer towards the N-terminal end of the bundle.

In contrast to the core and chelate constructs, Cu(II)α_3D-ChC2 displayed two intense CT bands at 401 (4429 $M^{-1}cm^{-1}$) and 499 (2020 $M^{-1}cm^{-1}$), producing a brown copper species with an R_ε ($\varepsilon_{401\ nm}/\varepsilon_{499\ nm}$) of 2.2. When compared to its Cu(II)α_3D-CH4, the λ_{max} of Cu(II)α_3D-ChC2 is red shifted by 24 nm and the intensity of this band increases by 2 fold. The second band at 499 nm (at 520 nm in Cu(II)α_3D-CH4) is more defined and intense than the corresponding bands in the previous constructs. The hyperfine coupling constant value of Cu(II)α_3D-ChC2 is 130 x 10^{-4} cm^{-1}, which is nevertheless ~70 x 10^{-4} cm^{-1} greater than the $A_{||}$ values of its native counterparts. Figure III-11 displays the relationship between the R_ε values and position of the Cys residue. This plot reveals that the Cys residue at the 21st position (of α_3D-CH3), which is located in loop 1, generated the highest R_ε value. In contrast, placing a Cys ligand deeper in the core of the bundle at the 14th position produced an R_ε value that is lower than a red copper center, nitrosocyanin, illustrating that the design strategy employed on α_3D-ChC2 is progressing towards green and blue copper sites. Moreover, the Cu(II) complex of α_3D-ChC2 is more long lived compared Cu(II)α_3D-CH3, showing that incorporating a metal binding site inside a hydrophobic environment results in a more stable Cu(II)-S(Cys) bond (Figure III-12).

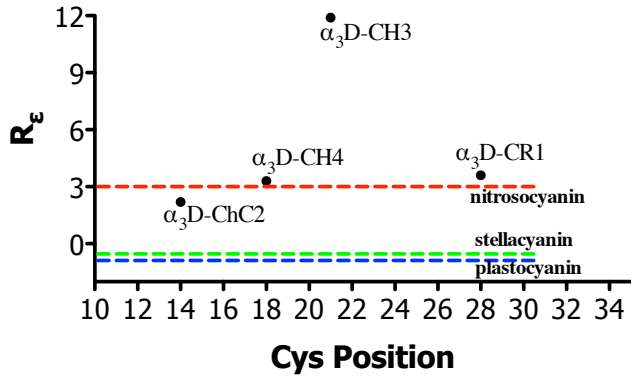

Figure III-11. Relationship between R_ε values and position of Cys residues.

It is conceivable that there are competing ligands that are provided by the peptide or the solvent that leads to tetragonal Cu(II) complexes. In able to test this hypothesis, comparative metal binding studies using Co(II) UV-Vis and ^{113}Cd(II)-NMR were performed. The pattern of the *d-d* bands from an absorption spectrum of the Co(II) complex can be used to elucidate coordination number and the chemical shift range. Similarly, ^{113}Cd(II)-NMR offers a sensitive method for determining the ligand environment for this slightly larger ion. The *d-d* transitions at 583, 622 and 675 nm observed for Co(II)α_3D-CR1 suggest the formation of a tetrahedral geometry is possible, which is the desired coordination environment. Likewise, the UV-VIS spectrum of the Co(II) complex of α_3D-CH3 show three *d-d* transition bands at 541, 580 and 630; as well as, the corresponding spectrum of Co(II)α_3D-ChC2, with bands at 539, 606 and 620. The Co(II) spectrum of α_3D-ChC2 nearly mirrors the respective *d-d* absorption bands in Co(II)–substituted stellacyanin, which possesses an N_2SO metal binding site.[34, 35] In contrast, Co(II)α_3D-CH4 show a weak *d-d* band at 573 nm, which implies a much higher coordination environment (5-6) compared to Co(II)α_3D-CH3.

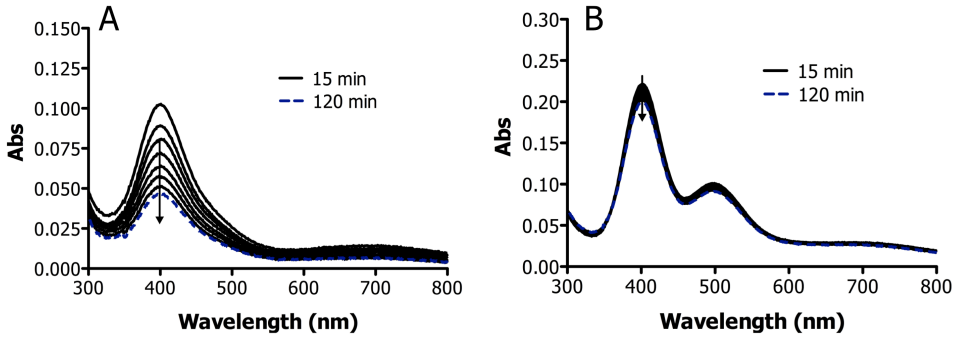

Figure III-12. Bleaching of the absorption features of Cu(II)α_3D-CH3 (A) and Cu(II)α_3D-ChC1 (B) species. A) After 120 min, about 55% of the Cu(II)α_3D-CH3 species has been lost. B) Cu(II)α_3D-ChC1 still maintained 90% of the Cu(II) complex after 120 min.

The ^{113}Cd(II)-NMR spectrum of α_3D-CR1 indicated the formation of competing species, which is presented by two resonance peaks at 320 and 363 ppm. ^{113}Cd(II)α_3D-CH3 also generated two resonance peaks at 344 and 369 ppm. Compared to the reported chemical shift values for native CuT1 proteins, the downfield resonance peak of ^{113}Cd(II)α_3D-CR1 and ^{113}Cd(II)α_3D-CH3 is 9–16 and 17 ppm upfield from azurin (373-379 ppm) and stellacyanin (380 ppm),[37, 38]

respectively, demonstrating that the ~360 ppm species share an equivalent donor set as their native counterparts. This comparison suggests that the S(Met) can serve as a fourth ligand, which is not evident in the Cu(II) binding studies. Moreover, the upfield species is within the range of CdN_3O (~310-330 ppm) and implies an N_2SO_x donor set, where the O ligands could stem from exogenous $^-OH/H_2O$ molecules or the side chain of residues on the first loop of the bundle, such as Ser24 or Glu25. Moreover, the ^{113}Cd-NMR spectrum of α_3D-ChC2 showed a single peak at 336 ppm that signifies the presence of a cadmium species with an N_2S or N_2SO_x donor set. Altogether, the Co(II) complex implied that a tetrahedral environment was achieved and the ^{113}Cd-NMR study revealed that two N_2S species were formed. These results offert insight into how Cu(II) binds to the designed CuT1 sites.

In order to gain deeper insight into the coordination environment of Cu(II)α_3D-ChC2, I compared the absorption spectrum of this complex to previously reported protein CuT1 models, as well as to native and mutated CuT1 proteins. I found that a redesigned thioredoxin model[52] that was imparted with a CuT1 site, a native CuT1 protein auracyanin D,[53] as well two CuT1 mutants rusticyanin Met148Glu[30] and azurin Met161Glu[41] demonstrate similar Cu(II) absorption features as our *de novo* designed α_3D-ChC2 construct. The Cu(II) complex of the thioredoxin model, Trx[BC]-4.1.1,[52] which possesses an 2HisCys ligand set, shows an intense band at 422 nm (1840 $M^{-1}cm^{-1}$) and a second weaker band at 540 nm (690 $M^{-1}cm^{-1}$), generating an R_ε value (422 nm /540 nm) of 2.7. After the addition of cyanide, the authors observed a red shift to 438 and 554 and an R_ε of ~1.0, reflecting the properties of stellacyanin. This result suggested that an exogenous water ligand was bound and then replaced with a stronger cyanide ligand. Albeit the absorption bands of Cu(II)α_3D-ChC2 are at 401 and 499 nm, this comparison confirms that the Cu(II) ion is binding to the designed N_2S ligand environment. The second comparison is with a native CuT1 protein auracyanin D. The auracyanin family, A-D, is found in filamentous anoxygenic phototroph *Chloroflexus aurantiacus* and serves as electron transfer proteins in aerobic respiration and anoxygenic photosynthesis.[53] Auracyanin A and C exhibit the spectral properties of a green copper center with R_ε values of 0.32 (450nm /593 nm) and 0.89 (442 nm/569 nm), respectively. Auracyanin B has a classic blue copper spectrum, with an R_ε of 0.16 (458 nm/600 nm) centers. In contrast, auracyanin D displays the most perturbed characteristics

with a λ_{max} at 426 nm (~3000 $M^{-1} cm^{-1}$) and a second less intense band at 569 nm (~2500 $M^{-1} cm^{-1}$), yielding an R_ε of 1.2. Based on sequence alignments with auracyanin A and B, auracyanin D was predicted to have an O(Gln) axial ligand instead of a S(Met) found in auracyanin A-C. This O(Gln) ligand was concluded to be the origin of the highly perturbed site. Although Cu(II)α_3D-ChC2 is still 25 – 70 nm blue shifted, its R_ε value is only augmented by 1, which could be due to a lack of an axial ligand. Lastly, to examine the role of the S(Met), a Met148Glu and Met121Glu mutation was performed on rusticyanin[30] and azurin,[41] respectively. At pH > 6.0, the Cu(II) absorption spectrum of rusticyanin Met148Glu displayed an intense band at 396 nm and a second peak at 518 nm, producing a "brown" copper protein. The $A_{||}$ of this complex has a value of 125 x 10^{-4} cm^{-1}, which is within the range of CuT2 centers and my designed brown copper construct. For azurin Met121Glu, the copper center changes from blue at pH 4, to green at pH 5 and finally to brown at pH > 6.0, which has absorption bands at 416 (2500 $M^{-1} cm^{-1}$) and 570 nm (~1000 $M^{-1} cm^{-1}$). This complex has an $A_{||}$ value more similar to native CuT1 centers of 97 x 10^{-4} cm^{-1}. Overall, these comparisons confirm that a core-chelate design was able to recapitulate a CuT1 like site within the α_3D fold, and most importantly, these comparable results provide insight into future design of core-chelate constructs that includes an axial ligand bound in the Cu(II) state.

One of the characteristic physical properties of native cupredoxins is their short Cu-S(Cys) bond. To determine if the designed constructs can reproduce the reduced form of CuT1 proteins, XAS analysis was performed on the Cu(I) adduct of α_3D-CR1, α_3D-CH3, α_3D-CH4 and α_3D-ChC2. The XANES plot of the Cu(I) complexes showed an inflection point at ~8,984 eV, which is a characteristic of a Cu(I) 1s → 4p transition.[39] In addition, the XANES results reveal a trend that indicated that the coordination environment of these Cu(I) complexes. That is, the XANES spectra of Cu(I)α_3D-CR1 and Cu(I)α_3D-ChC2 overlay well, as does the corresponding plot for Cu(I)α_3D-CH3 and Cu(I)α_3D-CH4, revealing that each set of Cu(I) complexes share a similar coordination environment. The former set was concluded to show a XANES pre-edge feature indicative of a three coordinate complex, whereas the latter was assigned a four coordinate environment. These conclusions were substantiated with the EXAFS analysis. The Cu(I) adducts of α_3D-CR1 and α_3D-ChC2 fitted well to a three-atom environment that consists of an S atom

and two N atoms. Cu(I)α_3D-CR1 has a Cu(I)-S(Cys) bond at 2.16 Å, while the corresponding bond in the chelate-core design of α_3D-ChC2 elongates slightly to 2.18 Å. The Cu(I)-2N(His) bonds in both complexes are equivalent with a bond length of 1.92 Å. Since α_3D-ChC2 possesses a 2HisCys binding site, this construct should favor the formation of a three coordinate Cu(I) complex, therefore, the Cu(I)α_3D-ChC2 complex can be viewed as a pseudo internal standard for validating the coordination number of Cu(I)α_3D-CR1. Therefore, the XANES and EXAFS analysis demonstrated that Cu(I)α_3D-CR1 and Cu(I)α_3D-ChC2 form a Cu(I)N_2S complex.

Moreover, a similar comparison of the Cu(I) complex of α_3D-CH3 and α_3D-CH4 can be established. Cu(I)α_3D-CH3 fitted well to a 2S-2N four-atom model (model 2). The Cu(I)-2S has a bond length at 2.20 Å, where one of the sulfur ligands originates from a Cys residue, and the Cu(I)-2N(His) has a bond distance of 1.95 Å. Cu(I)α_3D-CH4 also fitted well to model 2. This complex contains a Cu(I)-2S and Cu(I)-2N(His) bond at 2.23 and 1.99 Å, respectively. The identity of the second sulfur ligand in both complexes is likely to originate from S(Met72), however the Cu(I)-S(Met) bond in native CuT1 centers have a longer bond length of 2.6 – 2.9 Å.[5] However, a Cu(I)-SR_2 bond at ~2.2 Å has been observed in the X-ray crystal structure of small molecule compounds. Thus, it is possible that such a short Cu(I)-S(Met) bond can form in α_3D-CH3 and α_3D-CH4 but not in native cupredoxins because the distance of the axial ligand from the copper center is controlled by aromatic side chains. Additionally, the EXAFS analysis implies that location of the metal binding site of α_3D-CH3 and α_3D-CH4 is arranged at the perimeter of the bundle. As a consequence, the copper complex is at the interface of the C-terminal end and allows for the S(Met) ligand to form a short bond as illustrated in Figure III-12.

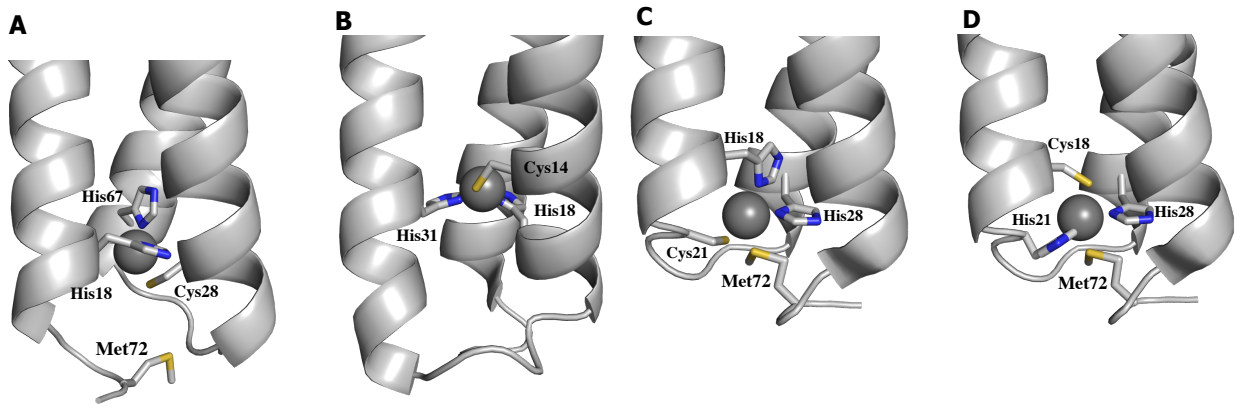

Figure III-13. Models of the reduced state based on the EXAFS analysis of the designed constructs. (A) Cu(I)α_3D-CR1. (B) Cu(I)α_3D-ChC2. (C) Cu(I)α_3D-CH3. (D) Cu(I)α_3D-CH4. The chelate constructs are able to form a short Cu-S(Met) bond at ~2.2 Å, which indicates that the copper ion is closer to loop 1 at the C-terminal end compared to the Cu(I) complex in α_3D-CR1.

Native CuT1 centers have a uniquely short Cu-S(Cys) bond with an average distance range between ~2.07 - ~2.25 Å, which for normal cysteine coordination is usually 2.3 – 2.4 Å.[5,8] The bond lengths from the EXAFS analysis were compared to the corresponding derived values of native CuT1 proteins. The bond lengths of the desgined Cu(I) adducts are compared to the reduced state of a blue (*P. aeruginosa* azurin),[54] green (*C. sativus* stellacyanin)[42] and red (*N. europea* nitrosocyanin) copper center.[43] Azurin contains a five-coordinate, trigonal bipyramidal copper complex, where the copper ion is bound to an N_2SS^*O(Gly backbone) ligand set. The copper complex in stellacyanin displays a distorted tetrahedral geometry, composing of a copper ion bound to an N_2SO ligand, with an O(Gln) serving as the axial ligand. The X-ray crystal structure of the reduced state of nitrosocyanin revealed a Cu(I)N_2SO four-coordinate complex, instead of a five-coordinate, square pyramidal complex that was observed in the oxidized state, where a water molecule provided the fifth ligand. The axial ligand of nitrosocyanin is occupied by an O(Glu). The EXAFS analysis on the Cu(I) adducts of the designed constructs exhibited metal centers with bond lengths and coordination numbers that are comparable to their native counterparts. The Cu(I)-S(Cys) bond of Cu(I)α_3D-CR1 and Cu(I)α_3D-ChC2 deviate the most from the native examples by ~0.04 Å, which demonstrates that these two complexes have a three-coordinate environment. The four-coordinate model of Cu(I)α_3D-CH3 and Cu(I)α_3D-CH4 has a Cu(I)-S(Cys) bond that is virtually equivalent to the respective bond in azurin and stellacyanin but ~0.05 Å shorter than nitrosocyanin. This comparison indicates that the

coordination environment of Cu(I)α_3D-CH3 and Cu(I)α_3D-CH4 is more similar to a blue or green than a red copper center. By and large, the XAS analysis illustrates that the designed constructs were able to recapitulate the reduced form of CuT1 centers within the α_3D scaffold.

Conclusions

De novo protein design provides a novel approach in studying the metal centers of native metalloproteins. In this work, I modeled the ET site of type-one copper centers within an unrelated three-helix bundle fold of α_3D to further examine the inherent stability and rack-induced bonding concept used to describe these unique copper sites. Moreover, I examined if unique spectroscopic and structural properties of cupredoxin proteins can be retained in the designed constructs. The first construct (α_3D-CR1) incorporated the 2HisCys residues at positions 18, 28 and 67 and produced tetragonal CuT2 Cu(II) species that displayed a dominating absorption band at ~390 nm. The second designs were imparted with a His-X_2-Cys chelate motif that is utilized by native proteins. These chelate constructs also produced CuT2 centers, however such designs generated more stable Cu(II) species (α_3D-CH3) and displayed additional bands (α_3D-CH4) > 400 nm that reveals some CuT1-like properties. Overall, the core and chelate constructs demonstrated that the C-terminal end of the α_3D fold was insufficient in applying the proper constraint to achieve an entatic complex.

The knowledge gained from the core and chelate studies was used as a foundation for the core-chelate construct. This design translated the His-X_2-Cys chelate motif one layer towards the N-terminal end of the bundle. α_3D-ChC2 produced a brown Cu(II) species that has been observed in mutated azurin and rusticyanin and share similar absorption features as native CuT1 auracyanin D. Furthermore, the XAS analysis on the Cu(I) adducts showed that these constructs were successful in recapitulating the reduced form of CuT1 centers, as indicated by a short Cu(I)-S(Cys), which is a unique characteristic of these native proteins. Overall, this current work shows that the 2HisCys site of CuT1 centers require a unique protein fold that is described by the rack-induced bonding model. When bound to Cu(II), this metal binding site is not inherently stable and is prone to an undesirable autoreduction reaction. Of the many metal sites the Pecoraro group has modeled, the most challenging to recapitulate in an α-helical bundle so far

has been a CuT1 center, which demonstrates that the β-barrel motif may confer a special ability to constrain the oxidized state of copper. Nonetheless, the results from this study, specifically the results from the work on α_3D-ChC2, will allow us to prepare cupredoxin centers within the hydrophobic core of the α_3D scaffold.

References

[1] Winkler, J. R., and Gray, H. B. (2014) Electron flow through metalloproteins, *Chem. Rev. 114*, 3369-3380.

[2] Winkler, J. R. (2011) Long-Range Electron Transfer in Biology, *Encyclopedia of Inorganic and Bioinorganic Chemistry*.

[3] Holwerda, R. A., Wherland, S., and Gray, H. B. (1976) Electron transfer reactions of copper proteins, *Annu. Rev. Biophys. Bioeng. 5*, 363-396.

[4] Regan, J. J., Di Bilio, A. J., Langen, R., Skov, L. K., Winkler, J. R., Gray, H. B., and Onuchic, J. N. (1995) Electron tunneling in azurin: the coupling across a β-sheet, *Chem. Biol. 2*, 489-496.

[5] Hart, P. J., Nersissian, A. M., and George, S. D. (2011) Copper Proteins with Type 1 Sites, *Encyclopedia of Inorganic and Bioinorganic Chemistry*.

[6] Lu, Y. (2003) Electron Transfer Cupredoxin, In *Comprehensive Coordination Chemistry II: From Biology to Nanotechnology* (Que, J., L., and Tolman, W. B., Eds.), pp 91-122, Elsevier Ltd., San Diego, CA, USA.

[7] Malmstrom, B. G. (1994) Rack-induced bonding in blue-copper proteins, *Eur. J. Biochem. 223*, 711-718.

[8] Solomon, E. I., Szilagyi, R. K., DeBeer George, S., and Basumallick, L. (2004) Electronic structures of metal sites in proteins and models: contributions to function in blue copper proteins, *Chem. Rev. 104*, 419-458.

[9] Solomon, E. I., and Hadt, R. G. (2011) Recent advances in understanding blue copper proteins, *Coord. Chem. Rev. 255*, 774-789.

[10] Lu, Y., Berry, S. M., and Pfister, T. D. (2001) Engineering Novel Metalloproteins: Design of Metal-Binding Sites into Native Protein Scaffolds, *Chem. Rev. 101*, 3047-3080.

[11] Yu, F., Cangelosi, V. M., Zastrow, M. L., Tegoni, M., Plegaria, J. S., Tebo, A. G., Mocny, C. S., Ruckthong, L., Qayyum, H., and Pecoraro, V. L. (2014) Protein design: toward functional metalloenzymes, *Chem. Rev. 114*, 3495-3578.

[12] Plegaria, J. S., and Pecoraro, V. L. (2015) Sculpting Metal-binding Environments in *De Novo* Designed Three-helix Bundles, *Isr. J. Chem. 55*, 85-95.

[13] DeGrado, W. F., Summa, C. M., Pavone, V., Nastri, F., and Lombardi, A. (1999) *De novo* design and structural characterization of proteins and metalloproteins, *Annu. Rev. Biochem 68*, 779-819.

[14] Chakraborty, S., Kravitz, J. Y., Thulstrup, P. W., Hemmingsen, L., DeGrado, W. F., and Pecoraro, V. L. (2011) Design of a three-helix bundle capable of binding heavy metals in a triscysteine environment, *Angew. Chem. Int. Ed. Engl. 50*, 2049-2053.

[15] Cangelosi, V. M., Deb, A., Penner-Hahn, J. E., and Pecoraro, V. L. (2014) A *de novo* designed metalloenzyme for the hydration of CO_2, *Angew. Chem., Int. Ed. Engl. 53*, 7900-7903.

[16] Plegaria, J. S., Dzul, S., Zuiderweg, E. R., Stemmler, T. L., and Pecoraro, V. L. (2015) Apoprotein Structure and Metal Binding Characterization of a *De Novo* Designed Peptide, α_3DIV, that Sequesters Toxic Heavy Metals, *Biochemistry*.

[17] Walsh, S. T., Cheng, H., Bryson, J. W., Roder, H., and DeGrado, W. F. (1999) Solution structure and dynamics of a *de novo* designed three-helix bundle protein, *Proc. Natl. Acad. Sci. U.S.A. 96*, 5486-5491.

[18] Lovejoy, B., Choe, S., Cascio, D., McRorie, D., DeGrado, W., and Eisenberg, D. (1993) Crystal structure of a synthetic triple-stranded α-helical bundle, *Science 259*, 1288-1293.

[19] Luo, P., and Baldwin, R. L. (1997) Mechanism of helix induction by trifluoroethanol: a framework for extrapolating the helix-forming properties of peptides from trifluoroethanol/water mixtures back to water, *Biochemistry 36*, 8413-8421.

[20] Rohl, C. A., and Baldwin, R. L. (1997) Comparison of NH exchange and circular dichroism as techniques for measuring the parameters of the helix-coil transition in peptides, *Biochemistry 36*, 8435-8442.

[21] Santoro, M. M., and Bolen, D. W. (1988) Unfolding free energy changes determined by the linear extrapolation method. 1. Unfolding of phenylmethanesulfonyl .α.-chymotrypsin using different denaturants, *Biochemistry 27*, 8063-8068.

[22] Xiao, Z., Loughlin, F., George, G. N., Howlett, G. J., and Wedd, A. G. (2004) C-terminal domain of the membrane copper transporter Ctr1 from *Saccharomyces cerevisiae* binds four Cu(I) ions as a cuprous-thiolate polynuclear cluster: sub-femtomolar Cu(I) affinity of three proteins involved in copper trafficking, *J. Am. Chem. Soc. 126*, 3081-3090.

[23] McMaster, W. H., Del Grande, N. K., Mallett, J. H., and Hubbell, J. H. (1969) *Compilation of X-Ray Cross Sections*, Lawrence Livermore National Laboratory Report.

[24] Weng, T. C., Waldo, G. S., and Penner-Hahn, J. E. (2005) A method for normalization of X-ray absorption spectra, *J. Syn. Rad. 12*, 506-510.

[25] George, G. N., and Pickering, I. J. (2000) EXAFSPAK.

[26] Rehr, J. J., Kas, J. J., Vila, F. D., Prange, M. P., and Jorissen, K. (2010) Parameter-free calculations of X-ray spectra with FEFF9, *Phys. Chem. Chem. Phys. 12*, 5503-5513.

[27] Dimakis, N., and Bunker, G. (2002) Group-fitted ab initio single- and multiple-scattering EXAFS Debye-Waller factors, *Phys. Rev. B 65*.

[28] Chen, Y. H., Yang, J. T., and Chau, K. H. (1974) Determination of the helix and beta form of proteins in aqueous solution by circular dichroism, *Biochemistry 13*, 3350-3359.

[29] Murphy, L. M., Strange, R. W., Karlsson, B. G., Lundberg, L. G., Pascher, T., Reinhammar, B., and Hasnain, S. S. (1993) Structural characterization of azurin from *Pseudomonas aeruginosa* and some of its methionine-121 mutants, *Biochemistry 32*, 1965-1975.

[30] Hall, J. F., Kanbi, L. D., Strange, R. W., and Hasnain, S. S. (1999) Role of the Axial Ligand in Type 1 Cu Centers Studied by Point Mutations of Met148 in Rusticyanin, *Biochemistry 38*, 12675-12680.

[31] Kitajima, N. (1992) Synthetic Approach to the Structure and Function of Copper Proteins, In *Adv. Inorg. Chem.*, pp 1-77, Elsevier, Ltd.

[32] Mizoguchi, T. J., Di Bilio, A. J., Gray, H. B., and Richards, J. H. (1992) Blue to type 2 binding. Copper(II) and cobalt(II) derivatives of a Cys112Asp mutant of *Pseudomonas aeruginosa* azurin, *J. Am. Chem. Soc. 114*, 10076-10078.

[33] Siluvai, G. S., Mayfield, M., Nilges, M. J., Debeer George, S., and Blackburn, N. J. (2010) Anatomy of a red copper center: spectroscopic identification and reactivity of the copper centers of *Bacillus subtilis* Sco and its Cys-to-Ala variants, *J. Am. Chem. Soc. 132*, 5215-5226.

[34] McMillin, D. R., Rosenberg, R. C., and Gray, H. B. (1974) Preparation and spectroscopic studies of cobalt(II) derivatives of blue copper proteins, *Proc. Natl. Acad. Sci. U. S. A. 71*, 4760-4762.

[35] Strong, C., Harrison, S. L., and Zeger, W. (1994) Preparation and characterization of cobalt(II)-substituted rusticyanin, *Inorg. Chem. 33*, 606-608.

[36] Bertini, I., and Luchinat, C. (1984) High spin cobalt(II) as a probe for the investigation of metalloproteins, *Adv. Inorg. Chem. 6*, 71-111.

[37] Öz, G., Pountney, D. L., and Armitage, I. M. (1998) NMR spectroscopic studies of I= 1/2 metal ions in biological systems, *Biochem. Cell Biol. 76*, 223-234.

[38] Engeseth, H. R., McMillin, D. R., and Otvos, J. D. (1984) Comparative Cd-113 Nuclear Magnetic Resonance Studies of Cd(II)- substituted Blue Copper Proteins, *J. Biol. Chem. 256*, 4822-4826.

[39] Kau, L. S., Spira-Solomon, D. J., Penner-Hahn, J. E., Hodgson, K. O., and Solomon, E. I. (1987) X-ray absorption edge determination of the oxidation state and coordination number of copper. Application to the type 3 site in *Rhus vernicifera* laccase and its reaction with oxygen, *J. Am. Chem. Soc. 109*, 6433-6442.

[40] Chen, K., Yuldasheva, S., Penner-Hahn, J. E., and O'Halloran, T. V. (2003) An atypical linear Cu(I)-S_2 center constitutes the high-affinity metal-sensing site in the CueR metalloregulatory protein, *J. Am. Chem. Soc. 125*, 12088-12089.

[41] Karlsson, B. G., Tsai, L. C., Nar, H., Sanders-Loehr, J., Bonander, N., Langer, V., and Sjolin, L. (1997) X-ray structure determination and characterization of the *Pseudomonas aeruginosa* azurin mutant Met121Glu, *Biochemistry 36*, 4089-4095.

[42] DeBeer George, S., Basumallick, L., Szilagyi, R. K., Randall, D. W., Hill, M. G., Nersissian, A. M., Valentine, J. S., Hedman, B., Hodgson, K. O., and Solomon, E. I. (2003) Spectroscopic investigation of stellacyanin mutants: axial ligand interactions at the blue copper site, *J. Am. Chem. Soc. 125*, 11314-11328.

[43] Basumallick, L., Sarangi, R., DeBeer George, S., Elmore, B., Hooper, A. B., Hedman, B., Hodgson, K. O., and Solomon, E. I. (2005) Spectroscopic and density functional studies of the red copper site in nitrosocyanin: role of the protein in determining active site geometric and electronic structure, *J. Am. Chem. Soc. 127*, 3531-3544.

[44] Aboelella, N. W., Gherman, B. F., Hill, L. M., York, J. T., Holm, N., Young, V. G., Jr., Cramer, C. J., and Tolman, W. B. (2006) Effects of thioether substituents on the O_2 reactivity of beta-diketiminate-Cu(I) complexes: probing the role of the methionine ligand in copper monooxygenases, *J. Am. Chem. Soc. 128*, 3445-3458.

[45] Bassanetti, I., Mezzadri, F., Comotti, A., Sozzani, P., Gennari, M., Calestani, G., and Marchio, L. (2012) Influence of anions in silver supramolecular frameworks: structural characteristics and sorption properties, *J. Am. Chem. Soc. 134*, 9142-9145.

[46] Gennari, M., Lanfranchi, M., and Marchiò, L. (2009) Novel carbon-centered heteroscorpionate ligands: Cu(I) complexes and luminescence properties, *Inorg. Chim. Acta 362*, 4430-4438.

[47] Tano, T., Mieda, K., Sugimoto, H., Ogura, T., and Itoh, S. (2014) A copper complex supported by an N2S-tridentate ligand inducing efficient heterolytic O-O bond cleavage of alkylhydroperoxide, *Dalton Trans. 43*, 4871-4877.

[48] Cao, Y.-D., Zheng, Q.-Y., Chen, C.-F., Hu, H.-M., and Huang, Z.-T. (2004) Synthesis of a novel three-coordinate copper(I) complex: a structural mimic of the reduced form of type 1 site in copper protein, *Inorg. Chim. Acta 357*, 316-320.

[49] Lu, Y., Roe, J. A., Bender, C. J., Peisach, J., Banci, L., Bertini, I., Gralla, E. B., and Valentine, J. S. (1996) New Type 2 Copper-Cysteinate Proteins. Copper Site Histidine-to-Cysteine Mutants of Yeast Copper-Zinc Superoxide Dismutase, *Inorg. Chem. 35*, 1692-1700.

[50] Solomon, E. I. (2006) Spectroscopic methods in bioinorganic chemistry: blue to green to red copper sites, *Inorg. Chem. 45*, 8012-8025.

[51] Walsh, S. T. R., Lee, A. L., DeGrado, W. F., and Wand, A. J. (2001) Dynamics of a *De Novo* Designed Three-Helix Bundle Protein Studied by ^{15}N, ^{13}C, and ^{2}H NMR Relaxation Methods, *Biochemistry 40*, 9560-9569.

[52] Hellinga, H. W. (1998) Construction of a blue copper analogue through iterative rational protein design cycles demonstrates principles of molecular recognition in metal center formation, *J. Am. Chem. Soc. 120*, 10055-10066.

[53] King, J. D., McIntosh, C. L., Halsey, C. M., Lada, B. M., Niedzwiedzki, D. M., Cooley, J. W., and Blankenship, R. E. (2013) Metalloproteins diversified: the auracyanins are a family of cupredoxins that stretch the spectral and redox limits of blue copper proteins, *Biochemistry 52*, 8267-8275.

[54] DeBeer, S., Wittung-Stafshede, P., Leckner, J., Karlsson, G., Winkler, J. R., Gray, H. B., Malmström, B. G., Solomon, E. I., Hedman, B., and Hodgson, K. O. (2000) X-ray absorption spectroscopy of folded and unfolded copper(I) azurin, *Inorg. Chim. Acta 297*, 278-282.

Chapter IV. Electron Transfer Characterization of *De Novo* Designed Copper Metallopeptides

Introduction

Electron transfer (ET) is a fundamental step of the energy transduction pathways in many biological systems including photosynthesis and respiration. Together with iron and redox-active molecules, type-one or cupredoxin proteins (CuT1) function in electron transfer reactions as freely diffusible, membrane-bound or as part of a large complex in various organisms, including bacteria, plants and humans. For this reason, CuT1 proteins plastocyanin and azurin have been extensively studied to elucidate this essential reaction in nature.

There are three important factors that dictate the efficiency of electron transfer, and these factors are described in the semi-classical Marcus equation[1-3] (Equation IV-1):

$$k_{ET} = \sqrt{\frac{4\pi^3}{\hbar^2 \lambda RT}} H_{AB}^2 \exp[-\frac{(\Delta G° + \lambda)^2}{4\lambda RT}] \qquad \textbf{Equation IV-1}$$

where $-\Delta G°$ (the driving force) is the difference in reduction potential (E°) between the donor and the acceptor sites, H_{AB} is the donor-acceptor electron coupling and λ is the reorganization energy associated with ET. The λ factor covers the outer-sphere (λ_{out}), which is influenced by solvation of the ET site, and inner sphere (λ_{in}) nuclear rearrangement that occurs during electron transfer. The balance between these factors has been observed to be significantly influenced by the protein's overall and local (ET site) structure. Cupredoxin proteins have provided an excellent platform for investigating this synergy.[3, 4]

Cupredoxin centers display highly positive reduction potentials (Table IV-1), providing the suitable driving force for electron transfer. The E° value of normal aqueous copper salts, $CuCl_4$, is ~150 mV (vs. NHE). In contrast, cupredoxins express values that range from +180 to

Electrochemistry work were performed at University of Paris, Diderot, Department of Molecular Electrochemistry, in collaboration with Dr. Cedric Tard and the under the supervision of Dr. Matteo Duca. Photophysical measurements were performed at CEA, Saclay, France, Department of Bioenergetics, Structural Biology and Mechanisms, in collaboration with Dr. Winfried Leibl and Dr. Annamaria Quaranta.

+800 mV, with the lower and upper range observed in green copper (stellacyanin) and blue copper centers (plastocyanin and CuT1 site in laccase and human ceruloplasmin), respectively. The perturbed blue copper center in stellacyanin[5] and nitrite reductase,[6] which both exhibit a stronger bond with its axial ligand, has a range of +180 to +280 mV. Centers that lack an axial ligand(s), such as the CuT1 center in laccase,[7] have larger values of +354 – +800 mV, and the sites at the upper end of this range are proposed to constantly remain in a reduced state. This broad range of positive reduction potentials allows CuT1 proteins to be versatile ET agents in diverse physiological environments. Table IV-I lists the reduction potential of various cupredoxin proteins.

As introduced above, the reduction potentials of these metal centers are significantly influenced by the interaction between the copper ion and axial ligand (Met or Gln), as well as the hydrogen bonding and solvent exposure around the redox site. From site-directed mutagenesis studies, it was observed that the weaker the axial ligand, the higher the reduction potential value. Blue copper proteins plastocyanin,[8, 9] azurin[9-11] and rusticyanin[12] possess a weakly bound S(Met) ligand and have E° values that span the range from +250 to +680 mV.[13, 14] When S(Met) ligand in rusticyanin was mutated to a non-coordinating Leu residue, a reduction potential (at pH 3.2) of 800 mV was achieved.[15] Mutation studies that examined the hydrogen bonding networks around the CuT1 center in azurin revealed that these noncovalent interactions play a significant role in fine-tuning its redox property, producing E° values that span from -2 to +706 mV.[16] Moreover, rusticyanin has a longer metal binding loop that protects the copper center from the solvent environment and embeds it within a β-barrel fold; and as a result, possessing one of the highest reduction potentials of its family. Overall, the high reduction potential of native CuT1 proteins are attributed to the primary and secondary coordination environments, as well as the low dielectric environment of the β-barrel fold.

Table IV-1. Reduction potential of native cupredoxins.

Protein	$Cu^{(II/I)}$ +E° (mv vs. NHE)	pH	Sample Condition
Plastocyanin[8]	372 (5)	7.0	0.01M phosphate buffer, 0.05M NaCl
Azurin[10]	308	7.0	0.1 M phosphate
Rusticyanin[12]	670	2.2	0.5 M Na_2SO4
Stellacyanin[5]	184	6.5	8.3 mM NaH_2PO_4, 5.9 mM Na_2HPO_4, 8.3 mM Na_2SO_4
Nitrosocyanin[17]	85	7.0	0.05 M phosphate, 0.1 M KCl
Auracyanin A[18]	238	7.0	0.1 mM phosphate, 200 mM KCl
Auracyanin B	230		
Auracyanin C	423		
Auracyanin D	83		

The ET rate through a protein is subject to the electron coupling matrix element, H_{AB}, which is influenced by the distance that an electron must travel between the donor and acceptor, as well as the covalency of the metal-ligand complex as in the case for CuT1 proteins. A large H_{AB} involves a short donor and acceptor ET transfer distance and highly covalent metal-ligand bonds. For instance, plastocyanin contains two ET sites (Figure IV-1). The first is located ~6 Å from the copper and involves the second His ligand that is encompassed by a hydrophobic patch. The second site is an acidic patch of residues (42-45 & 59-61) that surrounds a surface-exposed Tyr residue that is ~13 Å removed from the copper center and was proposed to use the Cu-S(Cys) bond as a conduit for ET. [4, 19-28] Interestingly, even though the Tyr site is twice as far from the copper center, the ET rates from the two proposed sites to the copper center are similar, which demonstrates the highly covalent Cu-S(Cys) bond more than compensates for a longer distance.

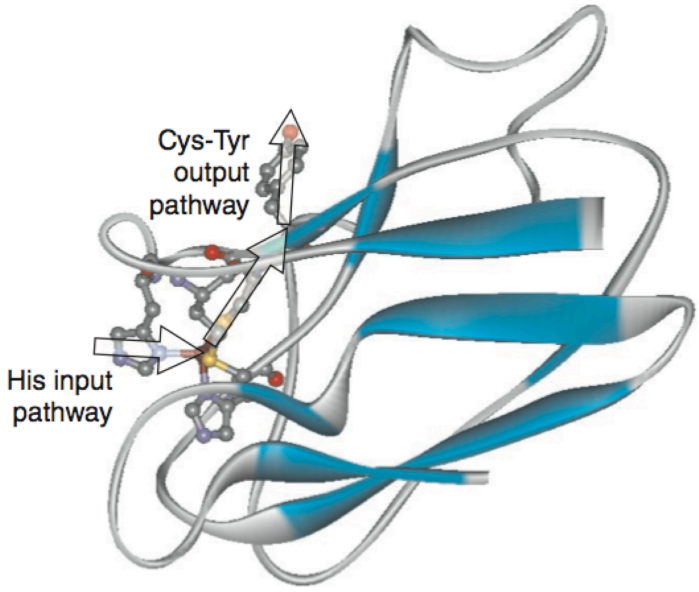

Figure IV-1 Proposed electron transfer pathways in plastocyanin.[28] Reprinted with permission from Ref 28. Copyright 2002 Elsevier Science Ltd.

The third factor in ET is minimizing the total reorganization energy ($\lambda_{total} = \lambda_{inner\text{-}sphere} + \lambda_{outer\text{-}sphere}$) during electron transfer. The protein fold serves a vital role in lowering this energy. It was determined that a low-dielectric cavity, such as a hydrophobic environment, can decrease the outer-sphere reorganization energy, while constraining the coordination environment of the metal center results in an equivalent effect on the inner-sphere reorganization energy. "Normal" copper salts show relatively high λ_{total} values as a result of the structural changes that are required for the Cu(II)/Cu(I) redox couple. For instance, $[Cu(phen)_2]^{2+/+}$ was determined to have a λ_{total} of 2.4 eV.[29] Conversely, ET studies on ruthenium modified azurins and plastocyanins produced λ_{total} in the range of ~ +0.7 to +1.2 eV.[30-34] These low values are attributed to the entatic state that the protein fold enforces on the CuT1 centers, where upon ET, the nuclear rearrangement at copper center is constrained by the coordination environment. This physical property is clearly evident in the overlay of the reduced and oxidized centers of cupredoxin proteins shown in Figure I-12. Furthermore, an inner-sphere reorganization energy range of +0.2 to +0.8 eV was obtained from reduced/oxidized crystal structures,[35] Resonance Raman distortion analysis,[36] as well as computational studies.[37] This range is significantly lower than the experimental value of ~1.4 eV obtained for a copper tetramine complex.[38] Ultimately, the $\lambda_{inner\text{-}sphere}$ of CuT1 centers is much

lower than "normal" copper compounds because, upon oxidation, the copper site avoids major structural transformations caused by a Jahn-Teller distortion as demonstrated in Figure IV-2.[39]

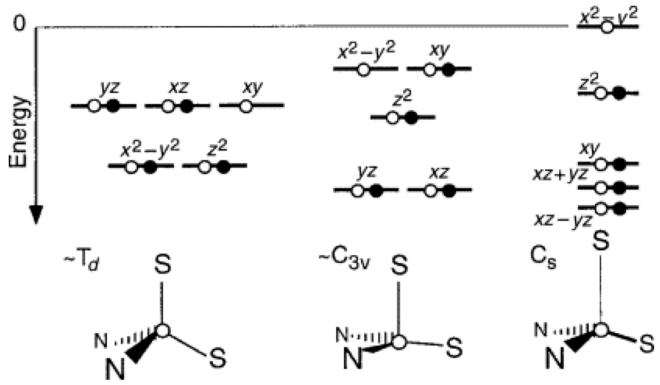

Figure IV-2. Representation of d-orbital splitting of three different symmetries in a d^9 system.[39] As result of a weakly bound axial ligand and a short Cu-S(Cys) bond, blue copper centers have a C_s symmetry, where the Jahn-Teller distortion is eliminated by lifting the HOMO degeneracy in the T_d or C_{3V} symmetry. This symmetry lowers the reorganization energy during electron transfer. Reprinted with permission from ref 39. Copyright 2000 Society of Biological Inorganic Chemistry.

In this chapter, we explore the redox and electron transfer properties of our designed cupredoxin constructs starting at the reduced state. Our objective is to determine if we are capable of sculpting an electron transfer site within the antiparallel three-helix bundle framework of α_3D. To achieve our objectives, we aimed to obtain the reduction potential and ET rates of selected constructs. The former parameter is examined by protein film voltammetry (PFV)[40] and the latter with a photophysical[41] method to generate a photo-oxidant that can interact with the Cu(I)-peptide species. In addition to examining these important ET parameters, this work allows us to reexamine the 2HisCys metal binding site and its redox and ET properties in an unrelated fold. Ultimately, the knowledge gained from this work will provide us a foundation for utilizing *de novo* protein design to prepare bifunctional/bimetallic α_3D constructs that possess an electron transfer site and a catalytic center.

Methods

Protein film voltammetry[40] offers a practical approach in examining ET and redox-coupled reactions, including catalysis or ion transport. As shown in Figure IV-3, the active site (in this case the copper center of the designed metalloprotein) is confined on an appropriate electrode surface to form a stable electroactive mono- or submono-layer film that allows for

facile electron transfer. Remarkably, the film resembles membrane-bound proteins in cells that are involved in bioenergetics processes. The applied potential forces electrons in and out of the metal center resulting in an observable signal (current). Even though the proteins in the film are not completely immobilized ("rocking" motion is possible), PFV can circumvent problems of sluggish diffusion and kinetics at the electrode surface; thereby, providing an electrochemical tool for controlling, detecting and quantifying complicated redox-coupled chemical reactions. Moreover, this method can be performed with a small amount of protein, typically in the range of 10^{-12} – 10^{-11} mol/cm^2 and at scan rates beyond 1000 V/s or below 1 mV/s. As the scan rate is varied, the separation between the oxidation and reduction peak potentials produces information on the ET kinetics. The average of these two peaks provides a good approximation of the reduction potential, which is the main focus of utilizing this technique.

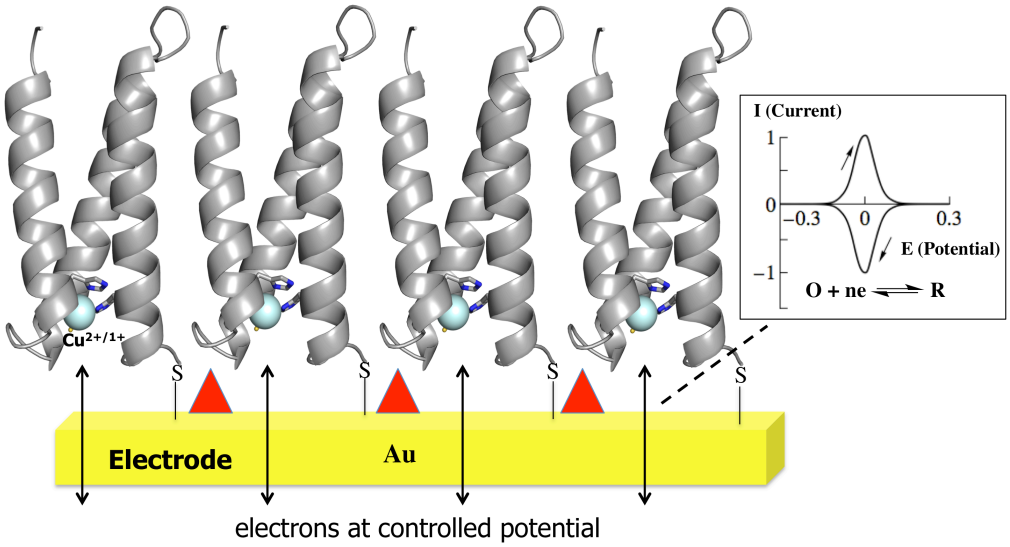

Figure IV-3. Cartoon showing chemically absorbed protein on a gold electrode. Tethering the designed copper metallopeptides, via Au-S(Cys77), bond to the working electrode surface establishes a mechanically robust system to study ET. The red triangles represent co-adsorbates, such as alkane-thiol molecules, that can be used to stabilize the protein film further. The reduction potential of a reversible ET process is determined from the average of the oxidation and reduction peak potentials.

Our second objective is to examine the ET activity of our copper metallopeptides using laser-flash photolysis (LFP). This technique is widely used to study light-induced transient species, such as radicals or excited states, in chemical and biological systems. In this work, ruthenium(II)trisbipyridine, Ru(II)bpy$_3$ was excited with a nanosecond laser flash to produce a highly oxidizing transient species and determined if the designed constructs (starting at the Cu(I) state) can interact with this species via an ET reaction. Ruthenium(II)trisbipyridine is a

commonly used photosentisizer for LFP and has many advantages. For instance, it displays an intense metal-to-ligand charge transfer band (MLCT) at 460 nm (ε~14,000 $M^{-1}\,cm^{-1}$), which allows selective excitation in the visible. Moreover, the excited state is long-lived (600 ns – 1 μs) and generates a highly reducing Ru(I) or oxidizing Ru(III) stable adduct after a redox reaction with a (sacrificial) electron donor or acceptor, respectively.

In this flash-quench experiment, a laser flash excites (at 460 or 520 nm) $Ru(II)bpy)_3$ to a singlet (S_1) excited state, which, in less than 1 ps, goes through an intersystem crossing pathway to reach a triplet excited state (T_1) to produce $^{*}Ru(II)bpy)_3$ species (Figure IV-4). An electron acceptor, ruthenium(III)hexamine (reaction I, k_1), interacts with this excited state to yield $Ru(III)bpy)_3$, a highly oxidizing species with a reduction potential of 1.3 V (vs. NHE).[41] In reaction II, the Cu(I)-peptide complex is present to reduce this oxidant (k_3), forming a transient Cu(II) species that can be detected by its absorbance. Finally, the electron acceptor reduces the oxidized copper complex (k_5), at this point all the species are restored to their respective ground state (reaction III). The absorbance of the transient $Ru(III)bpy)_3$ and Cu(II)-peptide species can be measured at a fixed time (Δt) or at a fixed wavelength (λ) after excitation. The measured absorbance is a difference spectrum (ΔA) of the ground and excited state. The absorption spectrum at a fixed Δt shows the disappearance of $Ru(III)bpy)_3$ and formation of Cu(II)-peptide species, which should corroborate with its corresponding Cu(II) absorption spectrum covered in Chapter 3. Moreover, the ET rate constants (k_3) of the Cu(II) formation are derived from the kinetic measurements at a fixed λ, where the copper species displays an absorbance. The ET reactions are summarized in Figure IV-4 and the equation scheme below.

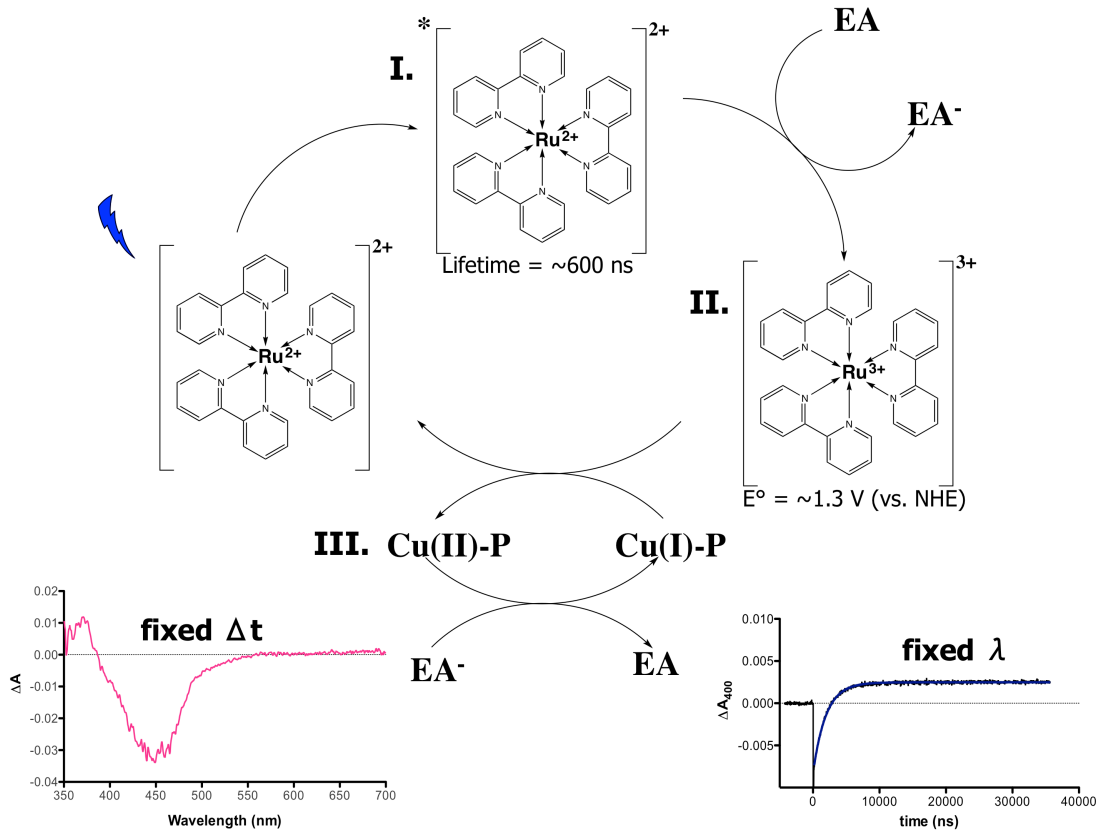

Figure IV–4. Representation of the flash-quench experiment: I. excited rutheniumtrisbipyridine is oxidized by an electron acceptor; II. the produced ruthenium(III)trisbipyridine species oxidizes Cu(I)-peptide complex; and III. the EA reduces the Cu(II)-peptide species, regenerating the ground state. The ΔA of the transient species can be measured at a fixed Δt or λ.

$$ {}^{*}A_{red} + B_{ox} \underset{}{\overset{K_{d1}}{\rightleftharpoons}} {}^{*}A_{red}/B_{ox} \underset{k_2}{\overset{k_1}{\rightleftharpoons}} A_{ox}/B_{red} \qquad \textbf{Equation IV-2} $$

$$ A_{ox} + C_{red} \underset{}{\overset{K_{d2}}{\rightleftharpoons}} A_{ox}/C_{red} \underset{k_4}{\overset{k_3}{\rightleftharpoons}} A_{red}/C_{ox} \qquad \textbf{Equation IV-3} $$

$$ B_{red} + C_{ox} \underset{}{\overset{K_{d3}}{\rightleftharpoons}} B_{red}/C_{ox} \underset{k_6}{\overset{k_5}{\rightleftharpoons}} B_{ox}/C_{red} \qquad \textbf{Equation IV-4} $$

$^{*}A_{red} = {}^{*}[Ru^{2+}(bpy)_3]^{2+}$ $B_{ox} = [Ru^{3+}(NH_3)_6]^{3+}$ $C_{red} = [Cu^{+}P]$ or P
$A_{red} = [Ru^{2+}(bpy)_3]^{2+}$ $B_{red} = [Ru^{2+}(NH_3)_6]^{2+}$ $C_{ox} = [Cu^{2+}P]^{+}$ or $P^{\bullet}$
$A_{ox} = [Ru^{3+}(bpy)_3]^{3+}$ (P = designed peptide)

Materials

Expression and Purification of Ala77Cys constructs. Ala77Cys derivatives of α_3D-CR1, α_3D-CH3, α_3D-CH4 and α_3D-ChC2 were prepared for the protein film voltammetry work. GeneArt® Site-Directed Mutagenesis System (Life Technologies) was used to mutate the codon for Ala77 to Cys within the pET15b vector. The product plasmid was transformed and overexpressed in *Escherichia. coli* BL21(DE3) cells and purified as described in Chapter 2. For the laer flash photolysis experiments, peptides α_3D-CR1, α_3D-CH3, α_3D-CH4 and α_3D-ChC2 were prepared.

Electrochemisty. Cyclic voltammetry measurements were obtained on a Metrohm AUTOLAB potentiostat and performed in the Molecular Electrochemistry Department at the University Paris-Diderot, in Paris, France, under the supervision of Drs. Cédric Tard and Matteo Duca. The electrochemical apparatus contained a gold (Au) disk working electrode (0.008 cm^2), a platinum wire counter electrode and an aqueous Saturated Calomel Electrode (SCE) as the reference electrode (0.241V + SCE = Normal Hydrogen Electrode). In the following order, the gold surface was polished with 1 μM, 0.3 μM and 0.05μM alumina. Subsequently, the Au electrodes were conditioned in an electrochemical cell (under Ar_g), which contained 0.5 M H_2SO_4, by scanning 20 times from –300 mV to +1500 mV (vs. SCE) at 500 mV/s until the cyclic voltammograms (CVs) overlay well, which is an indication of a homogenous surface. The working electrode is also conditioned in the experiment cell, which comprised 0.1 M phosphate buffer and 0.1 M Na_2SO_4, scanning 10 times from –300 mV to +600 mV at 50 and 100 mV/s. After each electrode has been polished and conditioned, 20 – 50 μL of a 0.5 mM Cu(I)-Peptide Ala77C solution was grafted on the Au surface in an anaerobic for 1 – 2 hr. CVs were collected at varying scan rates and at room temperature (~22 °C). Additional cyclic voltammetry experiments were performed on a BASi Epsilon potentiostat. A platinum wire counter, working Au (0.0201 cm^2) and Ag/AgCl (3.0 M NaCl) (0.210V + Ag/AgCl = NHE) reference electrode was used in this experiment. This Au electrode was polished and conditioned, and the CVs were obtained using a similar procedure as described above.

Nanosecond Laser Flash photolysis. Transient absorption kinetics and time-resolved spectra were collected on an Edinburgh Instruments LP920 flash photolysis spectrometer system that includes a Continuum Surelite OPO for sample excitation. The OPO was pumped with a

Continuum Q-switched Nd:YAG laser operating at 355 nm. The LP920 system utilizes a pulsed 450 W xenon arc lamp as the probe for the transient absorption measurements. The sample chamber was maintained at 20 °C by a water circulation system. Each sample contained Cu(I)-Peptide complex (0.9:1 Cu:peptide ratio), 10-20 μM Ru(II)trisbipyridine[41, 42] as the photo-inducible chromophore, 20 mM Ru(III)hexamine (0.10 V vs. NHE)[43] as the electron acceptor and 50 mM phosphate buffer. Samples were prepared in quartz anaerobic cuvettes and were bubbled with Ar for 10 min before each measurement. Samples with an absorbance $A_{460} = 0.3 – 0.4$ were excited at 460 or 520 nm. Additional chromophores were acquired for the rate versus driving force study. These include two rutheniumtrisbipyridine analogues with two and four ester groups,[44] which were provided by Dr. Christian Herrero, rutheniumtrisphenanthroline[45] (Sigma-Aldrich) and a zinc-porphyrin compound (ZnTMpyP)[46] obtained from Dr. Georgios Charalampidis. These measurements were performed at the CEA facility in Saclay, France by Dr. Annamaria Quaranta. The kinetics of the transient Cu(II)-peptide species fitted well to a mono-exponential decay equation and performed on Origin 8.5 software.

Results

Electrochemical Properties of Designed Constructs. To study the redox properties of our designed constructs, we introduced a terminal cysteine residue, via an Ala77Cys mutation, to constructs α_3D-CR1, α_3D-CH3, α_3D-CH4 and α_3D-ChC2 and chemically absorbed the Cu(I) form to generate electroactive protein film on a gold electrode surface. Our main objective is to utilize protein film voltammetry to determine the Cu(II/I) reduction potential for each construct. As discussed in the Introduction section, this parameter is one of three important factors in an electron transfer reaction as it is related to the driving force.

The electrochemical data are plotted using the European convention, that is the cathodic current is to the right (oxidation peak) and anodic to the left (reduction peak). Figure IV-5 shows the cyclic voltammograms (CVs) of Cuα_3D-CH3 and Cuα_3D-CR1 compared to their apo form. The CVs of the metallated peptides show oxidation (E_{pa}) and reduction peaks (E_{pc}), which are absent in the apoprotein. This comparison demonstrates that the ET reaction between the working gold electrode stems from the copper center and not the protein. Further, this illustrates

that these constructs formed an electroactive protein film that is capable of serving as ET centers. The same results were observed for Cuα_3D-CH4 and Cuα_3D-ChC2.

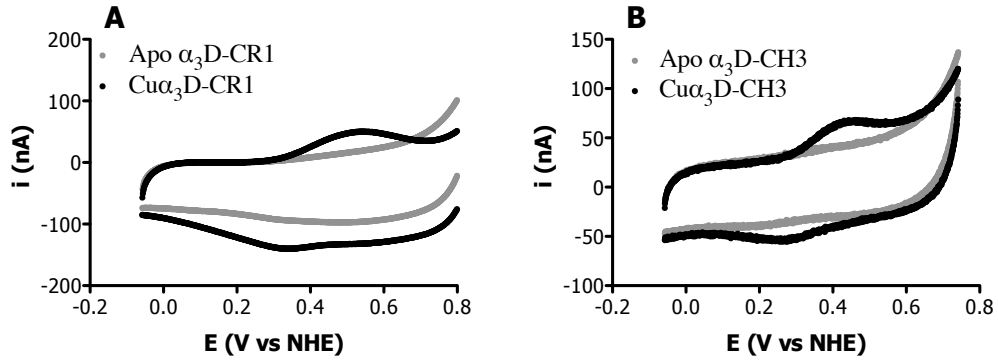

Figure IV–5. Cyclic voltammograms of designed constructs. A) Cuα_3D-CR1 at 50 mV/s. B) Cuα_3D-CH3 at 100 mV/s. This comparison shows that oxidation and reduction peaks stem from the copper center and not the protein. Samples contained 100 mM phosphate buffer and 100 mM Na_2SO_4.

Figure IV-6 shows the electrochemical stability of the protein film under two different scenarios. The first scenario examines the stability of the E_{pa} and E_{pc} peaks during multiple CV scans. A modest decrease in the intensity of both peaks is observed after several scans, indicating a slight depletion of the protein film. This observation is more pronounced in the second scenario, which involved collecting a CV (at 100 mV/s) at different points of the experiment during a ~2-3 hr period. In Figure IV-6B, the intensity of the oxidation and reduction peaks decreased from run 1 (time = 0 min) to run 16 (time = ~ 120 min). Nonetheless, even though the intensity of the peaks decreased over time, the peak positions did not vary.

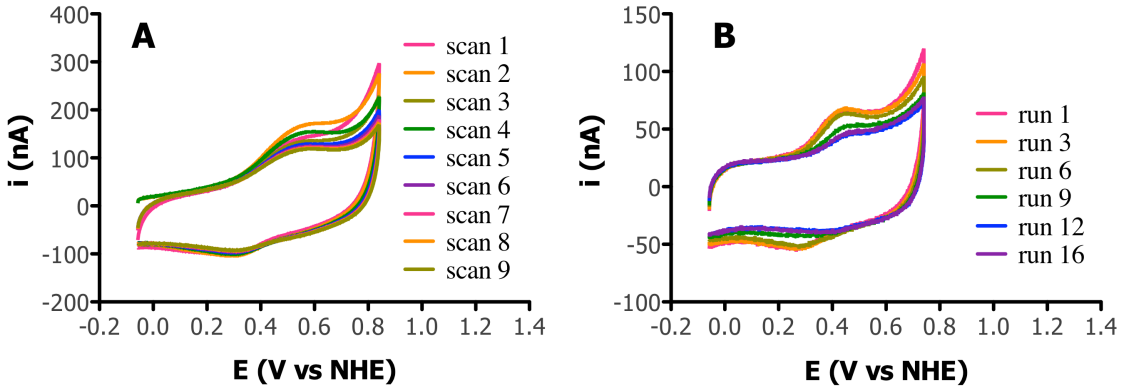

Figure IV–6. Electrochemical stability of designed constructs. A) Cyclic voltammograms of Cuα_3D-CR1 (at 50 mV/s), 9 continuous scans. B) Cyclic voltammograms of Cuα_3D-CH3 (at 100 mV/s), 6 separate scans in a course of an experiment.

Determination of reduction potential. The reduction potentials of Cuα_3D-CR1, Cuα_3D-CH3, Cuα_3D-CH4 and Cuα_3D-ChC2 were determined from a trumpet plot analysis. This analysis involved determining the oxidation and reduction positions as a function of scan rate. The reduction potential is produced from the average of both peaks at a slow scan rate: at 1 mV/s for Cuα_3D-CR1, Cuα_3D-CH3 and Cuα_3D-CH4 and 10 mV for Cuα_3D-ChC2. These results are summarized in Table IV-2. The reduction potential values of Cuα_3D-CR1, Cuα_3D-CH3 and Cuα_3D-CH4 are within the same range of 364 – 399 (±20) mV (vs. NHE). The core-chelate construct, α_3D-ChC2, displays an E° value of 462 (14) mV. The current versus scan rate plots in Figure IV-8 demonstrate a linear trend, which is indicative of a surface confined electrochemical reaction instead of a solution process. Furthermore, even at slow scan rates, we observed a considerable anodic and cathodic peak separation of 22 – 132 mV. This signifies a quasi-reversible ET reaction. Nonetheless, the comparison of the E° values of our designed constructs to those of native proteins, (Table IV-2) shows that we were successful in achieving a desired CuT1 characteristic.

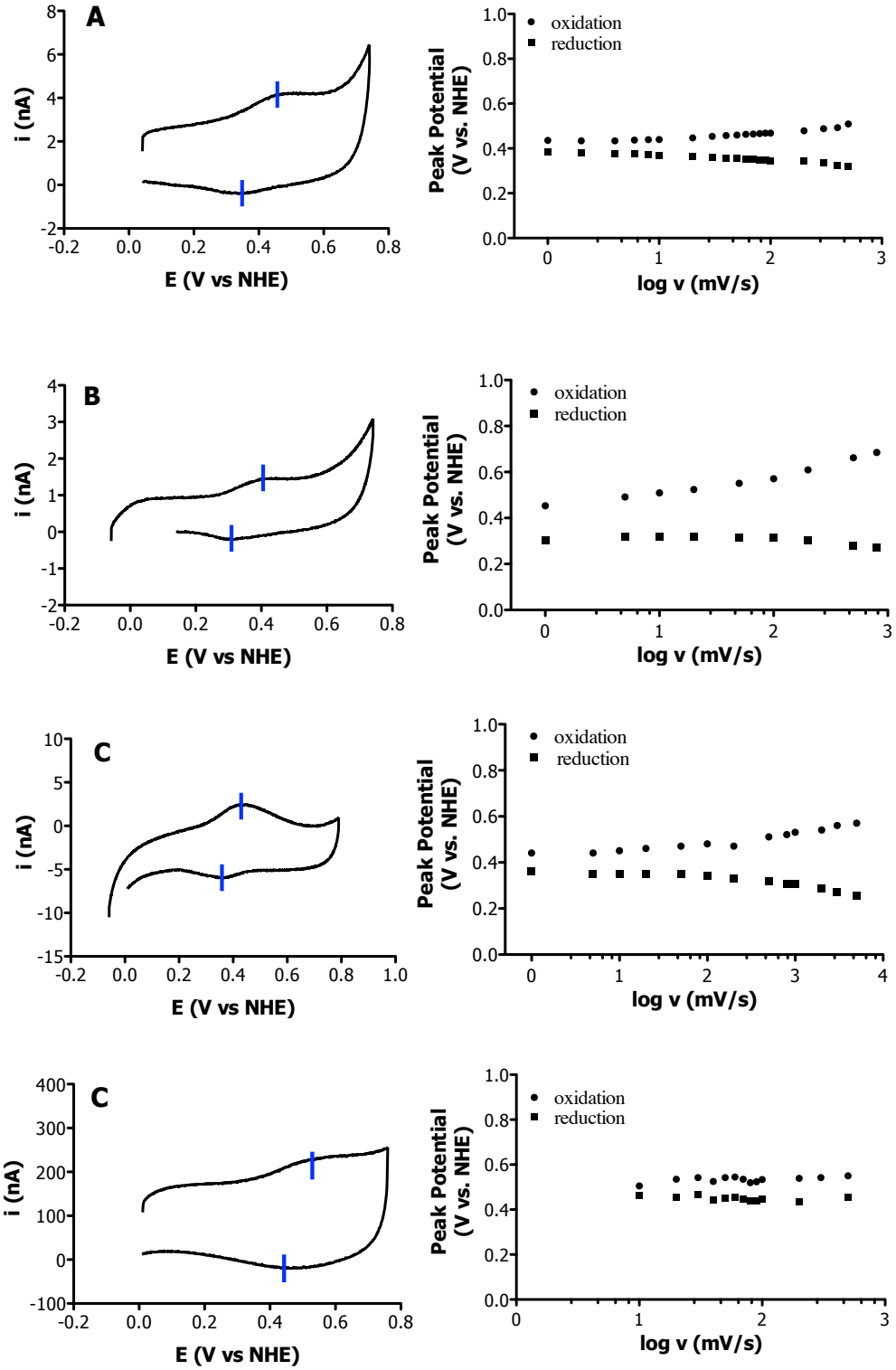

Figure IV–7. Cyclic voltammograms of designed constructs at a slow scan rate and representative trumpet plot (right). Blue lines show oxidation and reduction peaks. A) Cuα_3D-CR1 at 1 mV/s and pH 8.0. B) Cuα_3D-CH3 at 1 mV/s and pH 7.5. C) Cuα_3D-CH4 at 1 mV/s and pH 7.5. D) Cuα_3D-ChC2 at 10 mV/s and pH 7.5. Samples contained 100 mM phosphate buffer and 100 mM Na_2SO_4.

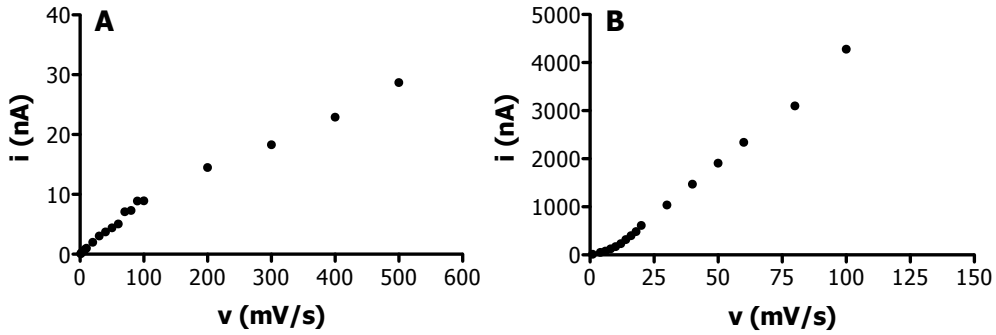

Figure IV–8. Current versus scan rate plots. A) Cuα_3D-CR1. B) Cuα_3D-CH3. Linear trend demonstrates a surface confined electrochemical reaction.

Table IV- 2. Reduction potential of designed constructs.

Protein	pH	Cu(II/I) E° (mV vs. NHE)	ΔE_p (mV)	Sample Conditions
α_3D-CR1 A77C[a]	8.0	+398 (23)	89 (58)	0.1 M phosphate, 0.1 M Na_2SO_4
α_3D-CH3 A77C[a]	7.5	+364 (19)	122 (43)	0.1 M phosphate, 0.1 M Na_2SO_4
α_3D-CH4 A77C[a]	7.5	+399 (3)	74 (8)	0.1 M phosphate, 0.1 M Na_2SO_4
α_3D-ChC2 A77C[b]	7.5	+462 (14)	45 (26)	0.1 M phosphate, 0.1 M Na_2SO_4
Plastocyanin (C-C)[9 c]	7.1	+404 (10)	63-87	0.1 M potassium phosphate
Azurin K27C[9 d]	7.4	+391-406	35-75	0.1 M potassium phosphate
Azurin S118C		+361-401	15-70	
Azurin[11]	4	+368 (3)[e]	4 (1)	0.1 M Na_2SO_4
	4	+318 (3)[f]	11-12	2.0 M NaCl
	8.5	+241 (3)[f]	16-18	2.0 M NaCl

[a]Scan rate 1.0 mV/s. [b]Scan rate 10.0 mV/s. [c]Grafted on am Au surface via disulfide bond. [d]Grafted on an Au surface via a Cys residue. [e]Adsorbed on Au, at 10 mV/s. [f]Adsorbed on pyrolytic graphite electrode, at 10 mV/s.

Investigation of ET reaction with a photo-oxidant. Using laser flash photolysis, photophysical measurements were obtained for α_3D-CR1, α_3D-CH3, α_3D-CH4 and α_3D-ChC2. Our objective was to examine the electron transfer reaction of these constructs with a light-induced photo-oxidant, rutheniumtrisbipyridine $Ru(bpy)_3$.

Figure IV-9 illustrates the absorption spectra of the transient species at different delays from laser pulse of $Ru(bpy)_3$ and $Ru(NH_3)_6$ only, apo α_3D-CH3 [with $Ru(bpy)_3$ and $Ru(NH_3)_6$] and Cu(I)α_3D-CH3 [with $Ru(bpy)_3$ and $Ru(NH_3)_6$]. At 100 ns $^*Ru(II)(bpy)_3$ is similarly present in all the samples, which is indicated by the small absorption at ~380 nm and a large depletion band at 450 nm (Figure IV-9A). At 1 μs (Figure IV-9B), as result of an ET reaction with $Ru(NH_3)_6$, the depletion band is modified and corresponds to the presence of $Ru(III)(bpy)_3$ species. Figure IV-9B displays that the amplitude of the negative band of the photo-oxidant is smaller by one-third in the Cuα_3D-CH3 spectrum, demonstrating a reduction of this species. Subsequently, the positive band at 400 nm in the 100 μs spectrum (Figure IV-9C) reveals that Cu(I)α_3D-CH3 reduced the $Ru(III)(bpy)_3$ species, and the ground state of the photo-oxidant is completely restored as signified by zero absorbance at 450 nm. Both the apo and $Ru(bpy)_3$ spectra still display residual $Ru(III)(bpy)_3$ species. Lastly, the absorption profile of Cuα_3D-CH3 at 10 ms (Figure IV-9D) shows that a recombination reaction had occurred between the Cu(II)-peptide species and $Ru(NH_3)_6$ while in the control samples, the $Ru(III)(bpy)_3$ species is reduced by the electron acceptor. Overall, these transient spectra exhibit that the Cu(I) adduct of α_3D-CH3 is able to participate in an ET reaction with the photo-oxidant.

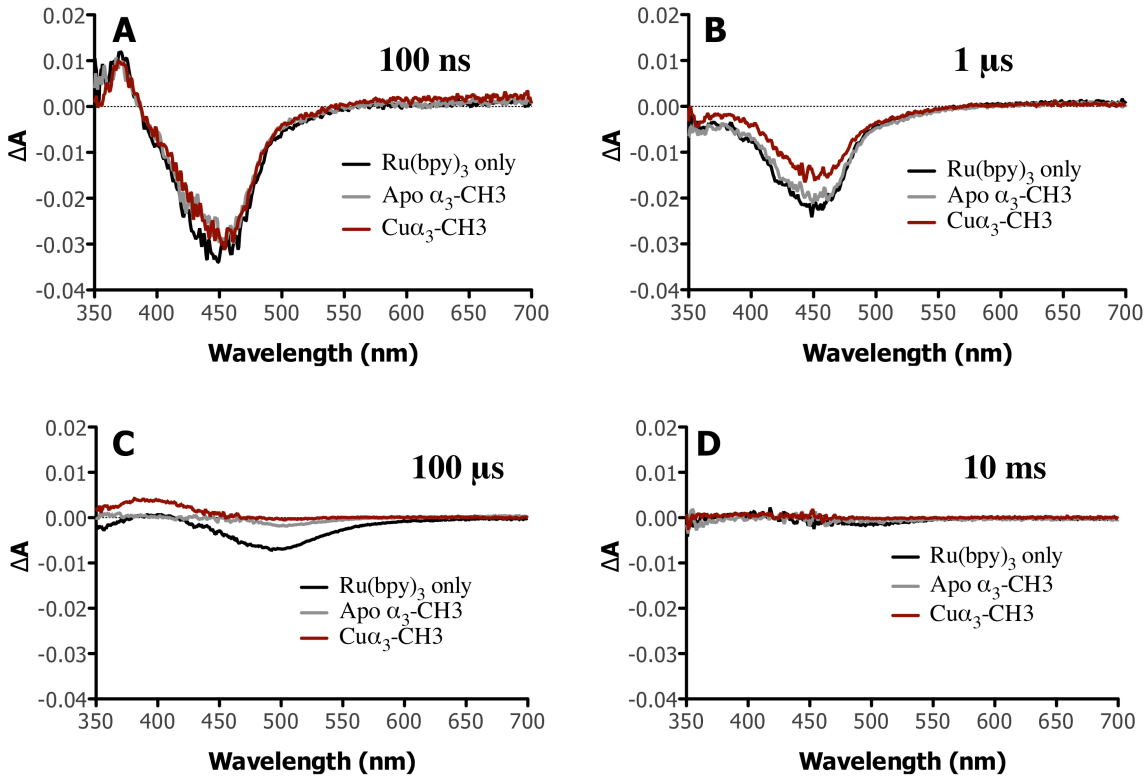

Figure IV–9. Transient absorption spectra of Cu(I)α_3D-CH3, apo α_3D-CH3 and $Ru(bpy)_3$. A) 100 ns. B) 1 µs. C) 10 µs. D) 10 ms. Each sample contained 140 µM $Ru(bpy)_3$ and 20 mM $Ru(NH_3)_6$. Cu-peptide sample contained 250 µM Cu(I) α_3D-CH3 complex, while the apo control had 250 µM α_3D-CH3. $Ru(bpy)_3$ was excited at 520 nm. Samples contained 50 mM phosphate buffer and pH adjusted at 7.5.

The same photophysical analysis was performed on Cuα_3D-CR1, Cuα_3D-CH4 and Cuα_3D-ChC2 to determine if these constructs will undergo an ET reaction with $[Ru(bpy)_3]^{3+}$, as demonstrated in the Cuα_3D-CH3 experiment. Figure IV-10 displays the absorption spectra of each construct at different time points and the spectrum that is generated from kinetic traces (plots on the right). The Cu(II) species of α_3D-CR1 (Figure IV-10A) is formed at 10 µs and corroborates with its kinetic spectrum at 30 µs. The transient spectra of Cuα_3D-CH4 (Figure IV-10C) do not display a definitive feature of an oxidized Cu(II) state; however, the spectrum extracted from kinetics reveals that the Cu(II) species was produced. Finally, oxidation of the Cu(I)α_3D-ChC2 species appears to be present at 200 µs, as shown in Figure IV-10D, but the kinetic trace at 400 nm displays zero absorbance (*vide infra*). For this reason, kinetic traces were not collected for this construct. Overall, the λ_{max} observed in the flash photolysis studies are

comparable to the UV-Vis experiments (Table IV-3), demonstrating that the Cu(II) form of Cuα_3D-CR1 and Cuα_3D-CH4 were generated as result of an ET reaction with the photo-oxidant.

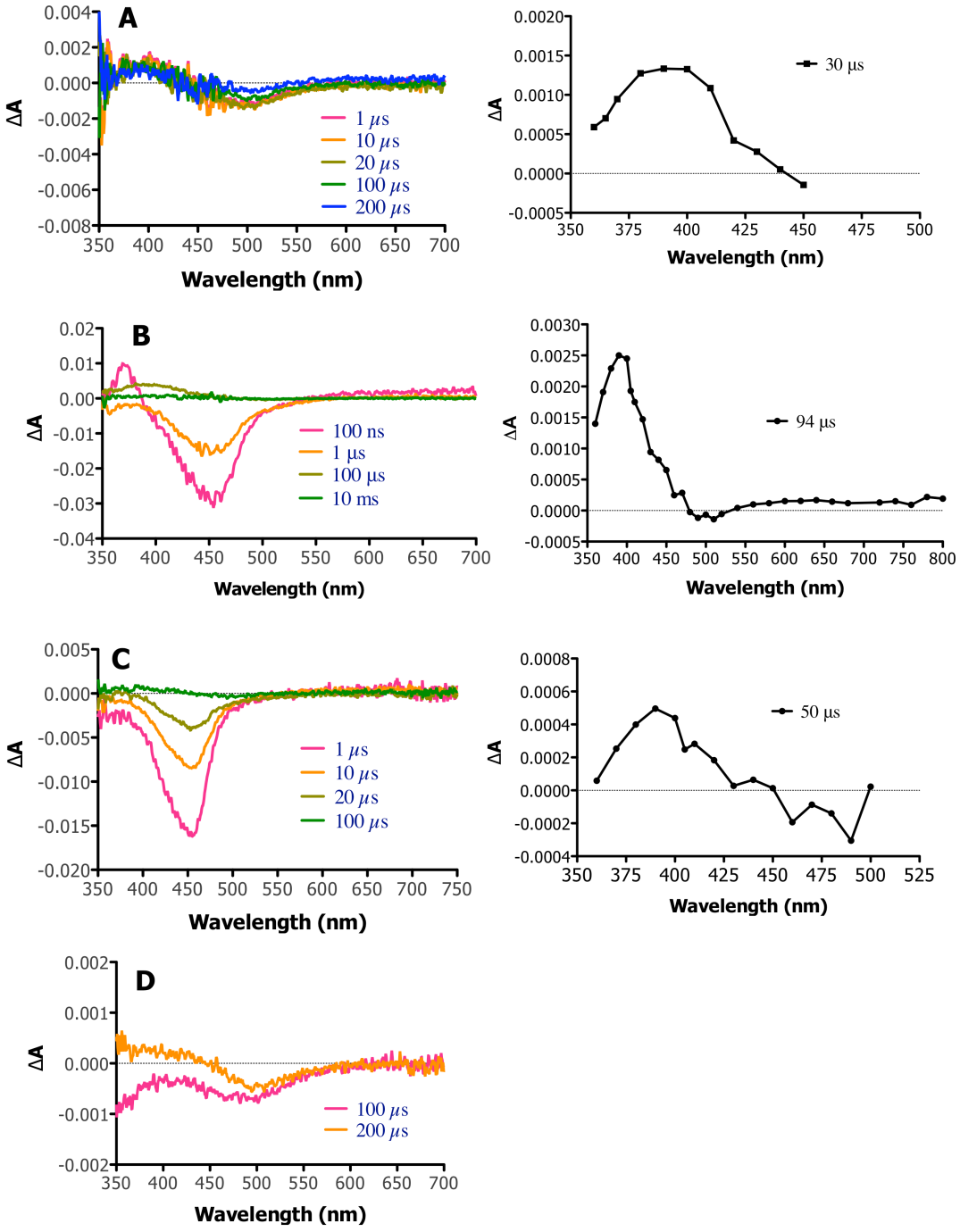

Figure IV–10. Transient absorption spectra of designed proteins. A) α_3D-CR1 [500 μM Cu(I)α_3D-CH3, 140 μM $Ru(bpy)_3$ and 20 mM $Ru(NH_3)_6$. $Ru(bpy)_3$ was excited at 520 nm]. B) α_3D-CH3 (same sample conditions as in Figure IV-9). C) α_3D-CH4 [100 μM Cu(I)α_3D-CH3, 10 μM $Ru(bpy)_3$ and 20 mM $Ru(NH_3)_6$. $Ru(bpy)_3$ was excited at 460 nm]. D) α_3D-ChC2 [100 μM Cu(I)α_3D-CH3, 140 μM $Ru(bpy)_3$

and 20 mM $Ru(NH_3)_6$. $Ru(bpy)_3$ was excited at 460 nm.]. Since Cu(II) species was not detected, transient spectra at different wavelengths were not collected for this construct.

Table IV-3. Absorption of Cu(II) species derived from photophysics.

Sample	λ_{max} (ε M^{-1} cm^{-1})	
	Flash Photolysis[a]	UV-Vis
Cuα_3D-CR1	~375-380	373 (1386)
Cuα_3D-CH3	390-400	397 (2464)
Cuα_3D-CH4	~380	376 (1810)
Cuα_3D-ChC2	-	401 (4135)

[a]Determined from absorption spectra generated from kinetic traces (see Figure IV-10 right plots).

Determination of first order rate constants (k_3). The kinetic traces at 400 nm were collected for Cuα_3D-CR1, Cuα_3D-CH3, Cuα_3D-CH4 and Cuα_3D-ChC2 and their apo form (Figure IV-11). The samples for these experiments contained 100 μM copper-peptide complex (except for Cuα_3D-CR1 where 500 μM complex was used because it was collected prior to the rate vs. concentration study). These kinetic plots show the decay of the photo-oxidant and formation of the Cu(II)-peptide species, characterized by a positive absorbance at 400 nm Cuα_3D-CR1 and Cuα_3D-CH3 displays an intense absorbance at 400 nm, compared to the kinetic plots of Cuα_3D-CH4 and Cuα_3D-ChC2. Cuα_3D-CH4 is slightly more positive than its apo control, exhibiting the formation of the Cu(II) species; while, the equivalent plot of Cuα_3D-ChC2 and apo are nearly identical. This reveals that in Cu(I)α_3D-ChC2 the Cu center is not oxidized by the photo-oxidant. Moreover, the $k_{3app\ CuP}/k_{3app\ ApoP}$ ratio can be used to compare the interaction of the metallated and apo peptide with the photo-oxidant. Apo α_3D-CR1 depletes the photo-oxidant at a similar rate as Cuα_3D-CR1, which is 1.1 times more efficient. However, the positive absorbance in the kinetic trace of Cuα_3D-CR1 clearly shows that the copper center was oxidized and reveals that the apoprotein, perhaps due to Tyr 70 oxidation, is the rate-limiting step. The rate of Cuα_3D-CH3 is 2.9 times faster than its apo control, while Cuα_3D-CH4 is only 1.6 more efficient than apo α_3D-CH4. The oxidation of Cuα_3D-CH4 could also require a preceding protein oxidation, similar to Cuα_3D-CR1; however, this construct, with the exception of the metal binding site, lacks redox active residues in its second coordination sphere like a Tyr or Trp residue. The efficiency of Cuα_3D-CH4 compared to its apo form could be a consequence of poor accessibility by the photo-oxidant. The corresponding comparison for α_3D-ChC2 again showed nearly identical rates,

which again signifies that the copper center does not interact with the photo-oxidant. The first order rate constants are summarized in Table IV-4. Overall, it is evident that presence of the peptide accelerates the decay of Ru(III)(bpy)$_3$ and with the exception of α_3D-CH3 has a mild effect on the ET kinetics.

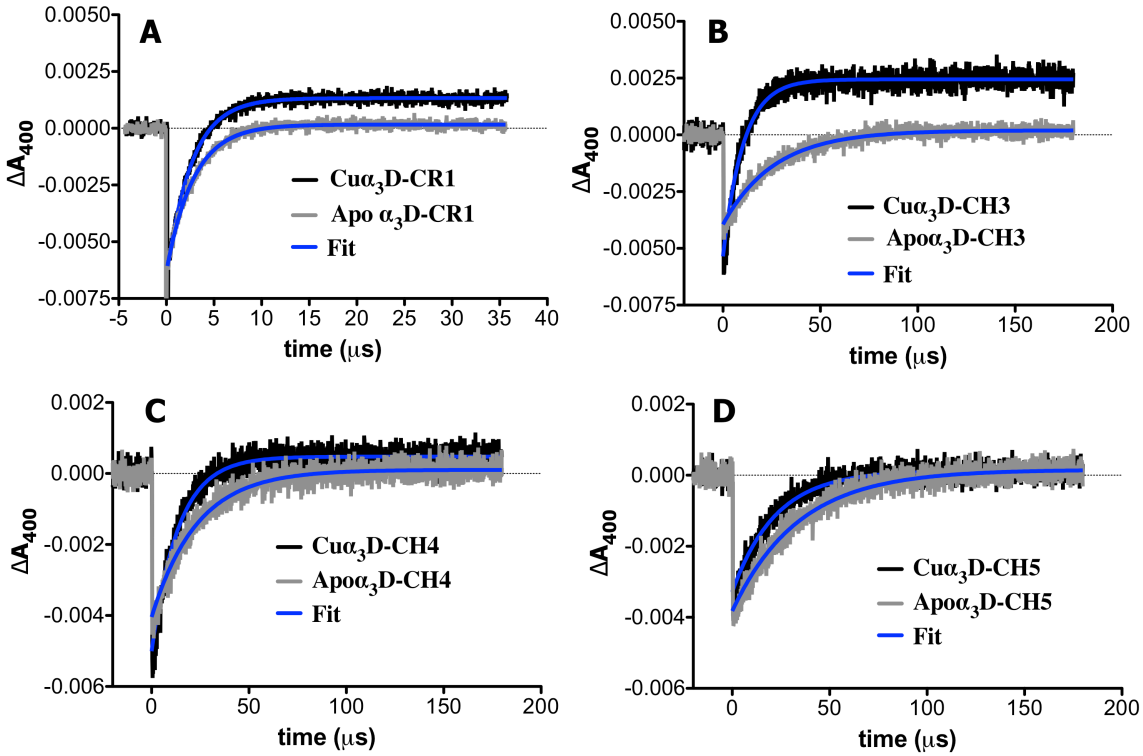

Figure IV–11. Kinetic traces at 400 nm. Fitted to a mono-exponential equation to determine the apparent rate constants k_{3app}. These traces show the decay of the Ru(III) species as result of an ET reaction with Cu(I)-P. The positive absorbance reveal the formation of Cu(II)-P. A) Cuα_3D-CR1 (500 μM Cu-P complex). B). Cuα_3D-CH3 (100 μM Cu-P complex). C) Cuα_3D-CH4 (100 μM Cu-P complex). D) Cuα_3D-ChC2 (100 μM Cu-P complex). Trace A and B display a distinct positive absorbance at longer time scans, while C has a slight absorbance. Trace D exhibit no such absorption, demonstrating Cu(I)α_3D-ChC2 was not oxidized by Ru(III)(bpy)$_3$.

Table IV-4. First-order rate constant of metallated and apo peptides.

Sample	k_{3app} (x10^5 s^{-1})[a]	k_{3app} (s^{-1})/ k_{2app} (s^{-1})[b]	$k_{3app\ CuP}$ (s^{-1})/ $k_{3app\ ApoP}$ (s^{-1})
Apo α_3D-CR1[c]	3.51	8.8	
Cuα_3D-CR1[c]	3.82	9.6	1.1
Apo α_3D-CH3	0.393 (0.007)	3.7	
Cuα_3D-CH3	1.15 (0.01)	10.8	2.9
Apo α_3D-CH4	0.457 (0.007)	4.3	
Cuα_3D-CH4	0.744 (0.07)	7.0	1.6
Apo α_3D-ChC2	0.445 (0.190)	4.2	
Cuα_3D- ChC2	0.440 (0.120)	3.8	0.99

[a]Derived from a kinetic trace at 400 nm. [b]Ratio between the k_{3app} of the apoprotein or Cu-protein and k_{2app} of $Ru(bpy)_3$ in the presence of only $Ru(NH_3)_6$. [c]500 μM Cu-peptide complex and rates derived from a single experiment.

Rate versus pH. This experiment was performed to determine if the reduction rate of the photo-oxidant is pH dependent, which provides insight into the mechanism of the ET reaction such as a proton-coupled reaction. This study was performed on Cuα_3D-CH3 and rates are summarized in Table IV-5. Figure IV-12 shows that the rate modestly increases with pH. However, the pH has a moderate effect on the k_{app} values, as the rate at pH 8.5 is only 3 times greater than pH 5.5.

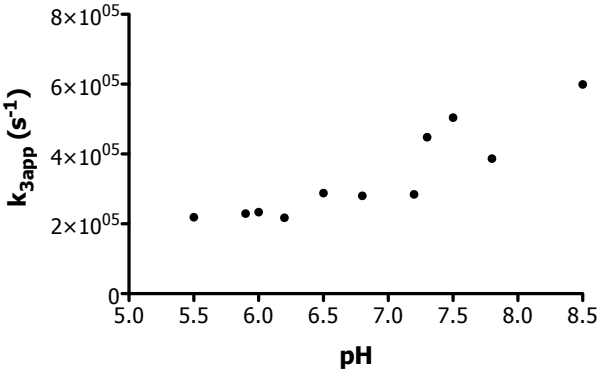

Figure IV−12. Rate versus pH plot of Cuα_3D-CH3. Samples contained 500 μM Cu(I)α_3D-CH3, 140 μM $Ru(bpy)_3$ and 20 mM $Ru(NH_3)_6$. $Ru(bpy)_3$ was excited at 520 nm.

Rate versus Concentration. A rate versus concentration plot was produced for Cuα_3D-CH3 to determine if the bimolecular ET reaction with the photo-oxidant is affected by the concentration of copper-protein complex. This construct was chosen because it was demonstrated to be the most reactive with the photo-oxidant, and since the overall structure and charge are homologous, the results from this study can be applied to all the constructs. The rates from this work are listed in Table IV-5 and plotted in Figure IV-I3. Kinetic traces (400 nm) were obtained at a concentration of 75 to 1000 μM copper-peptide complex, and the rates were derived from a mono-exponential fit. Figure IV-13A exhibits a Stern-Volmer plot, demonstrating a linear regression trend from 75 to 400 μM. Table IV-5 shows that at concentrations greater than 400 μM a precursor complex might form, conditions at which ET does not occur in a bimolecular fashion. The kinetic traces at two different concentrations (at 100 and 600 μM) in Figure IV-12B display a mono-phasic decay of the Ru(III)bpy$_3$ species and do not reflect the formation of a precursor complex, which would express bi-phasic behavior. However, a bi-phasic reaction cannot be ruled out since a two-step reaction is not easily distinguished in these intermolecular experiments. Saturation of the rates at high concentrations could also stem poor solvent diffusion or a gated ET, which will be described further in the Discussion section. Moreover, a bimolecular rate constant of 6.2 x 10^8 M^{-1} s^{-1}, where rate is linear with the concentration, is derived for Cuα_3D-CH3 (Figure IV-13A).

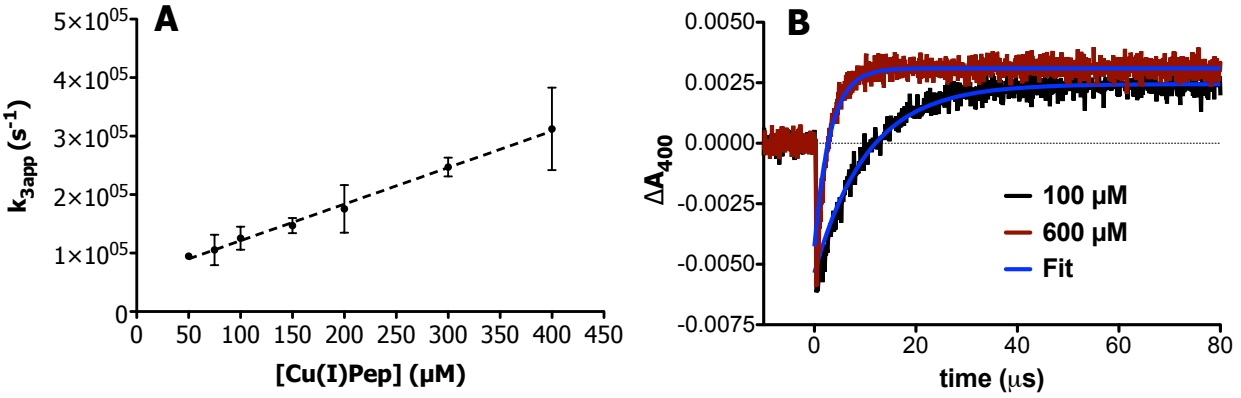

Figure IV–13. Rate versus concentration study performed on Cuα_3D-CH3. A) Stern-Volmer plot shows a linear regression trend between the rate and concentration from 50 to 400 μM Cu(I)Pep. Subsequent measurements were performed at 100 μM copper-peptide complex. Moreover, from this study, a bimolecular rate constant is derived for Cuα_3D-CH3. B) Kinetic traces at 100 and 600 μM show a mono-exponential decay of the $[Ru(bpy)_3)]^{3+}$ species.

Table IV-5. First-order rate constants of Cuα_3D-CH3 as a function of pH and Cu(I)Pep concentration.

pH	Cuα_3D-CH3 k_{3app} (x10^5 s^{-1})[a]	Cuα_3D-CH3 Concentration (μM)	$k_{3\ app}$ (x10^5 s^{-1})[b]
5.5	2.19	75	1.05 (0.26)
5.9	2.29	100	1.25 (0.20)
6.0	2.33	150	1.47 (0.13)
6.2	2.17	200	1.76 (0.41)
6.5	2.88	300	2.47 (0.16)
6.8	2.80	400	3.12 (0.71)
7.2	2.84	500	4.39 (1.16)
7.3	4.48	600	4.08 (0.39)
7.5	5.04	750	4.39[c]
7.8	3.87	1000	5.07[c]
8.5	5.99		

[a]Derived from a kinetic trace at 400 nm from a single experiment, with 500 μM Cu(I)-peptide complex. [b]Derived from a kinetic trace at 400 nm and performed in duplicates. [c]Determined from a single experiment.

Effect of Driving Force on Rate. The ET properties of Cuα_3D-CH3 and Cuα_3D-CH4 were further investigated by performing a rate versus driving force study. The objective of this work is to obtain approximate values for two important factors in ET: the reorganization energy (λ_{total} or $\lambda_{observed}$) and coupling factor ($H_{ABobserved}$, where A= peptide and B= photo-oxidant). The rate constants of Cuα_3D-CH3 and Cuα_3D-CH4 were determined using five different photo-oxidants, with potentials that range from 1.2 – 1.7 V (vs. NHE) (Figure IV-14). The results are listed in Table IV-6. The driving force (ΔG) values were derived from the difference of the E° between the photo-oxidant and the copper-peptide. The k_{3app} of Cuα_3D-CH3 range from 0.79 to 1.15 x 10^5 s^{-1}, demonstrating a moderate increase as a function of driving force. In contrast, the corresponding rates of Cuα_3D-CH4 span from 0.38 to 1.43 x 10^5 s^{-1}. Moreover, the rates vs. driving force plots were fitted to the Marcus equation (Eq IV-I) to determine the $\lambda_{observed}$ and $H_{ABobserved}$. Cuα_3D-CH3 shows a $\lambda_{observed}$ of 1.05 eV and $H_{ABobserved}$ of 0.025 cm^{-1}. The corresponding parameters for Cuα_3D-CH4 are slightly larger: 1.21 eV and 0.027 cm^{-1}.

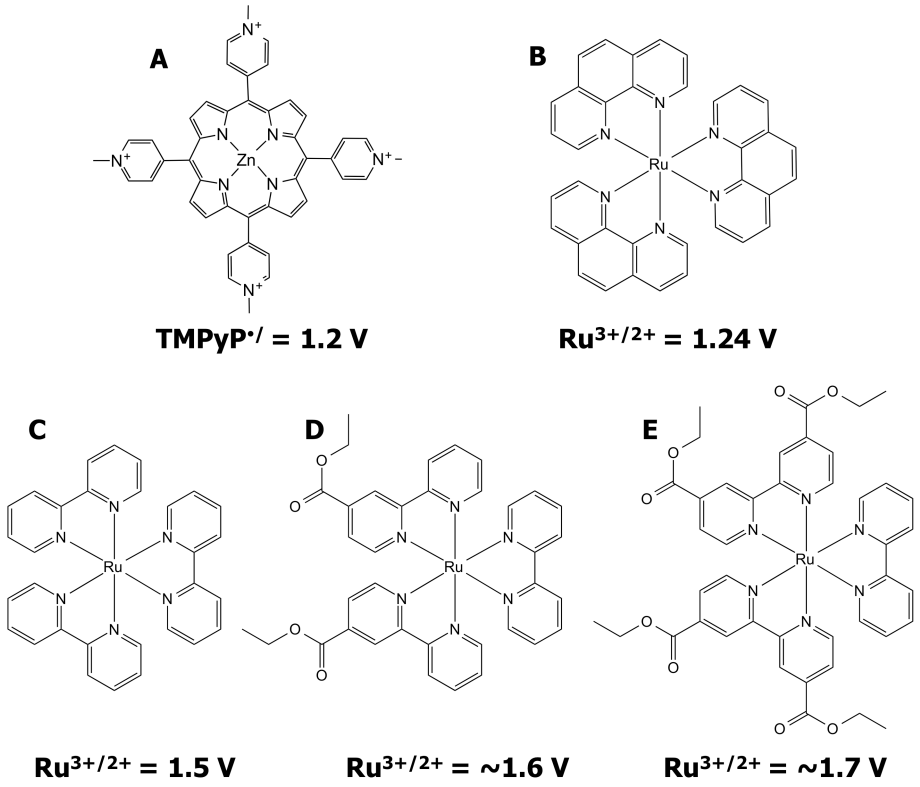

Figure IV–14. Photo-oxidants used in the rate versus driving force study and their corresponding reduction potential. (A) ZnTMPyP.[46] (B) Ru(phenanthroline)$_3$.[45] (C) Ru(bipyridine)$_3$.[41, 42] (D) 2Ester Ru(bipyridine)$_3$.[44] E) 4Ester Ru(bipyridine)$_3$.[44]

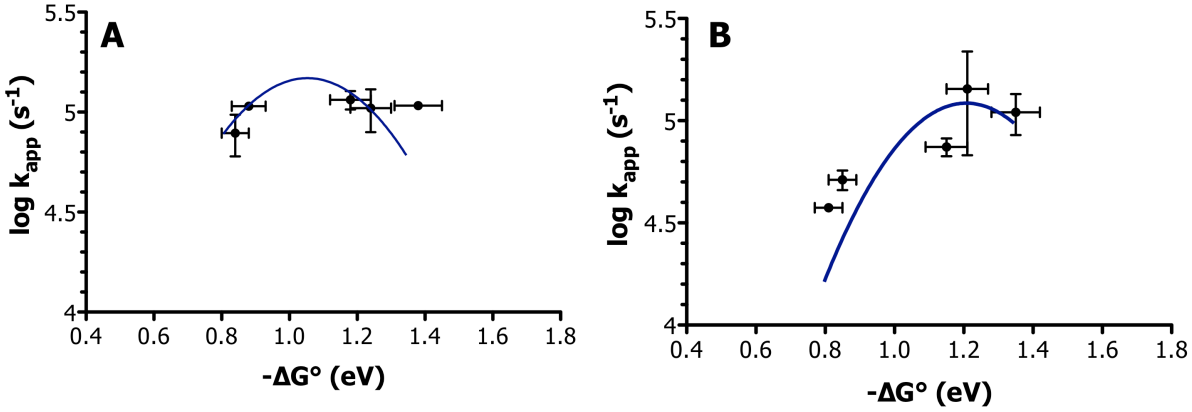

Figure IV–15. Rate versus driving force plots fitted to the Marcus equation (blue curve). A) Cuα_3D-CH3. B) Cuα_3D-CH4.

Table IV-6. Rate constants derived from rate versus driving force study.

Sample	k_{3app} (x10^5 s^{-1})[a]	$k_{3app\ sample}$ (s^{-1})/ $k_{2app\ photooxidant}$ (s^{-1})	$-\Delta G$ (eV)[b]
4EsterRu(bpy)$_3$	0.32 (0.23)		
Cuα_3D-CH3 + 4EsterRu(bpy)$_3$	1.08 (-)	3.4	1.38 (0.07)
Cuα_3D-CH4 + 4EsterRu(bpy)$_3$	1.10 (0.25)	3.4	1.35 (0.07)
2EsterRu(bpy)$_3$	0.11		
Cuα_3D-CH3 + 2EsterRu(bpy)$_3$	1.05 (0.25)	9.5	1.24 (0.06)
Cuα_3D-CH4+ 2EsterRu(bpy)$_3$	1.43 (0.75)	13.0	1.21 (0.06)
Ru(bpy)$_3$	0.11 (0.02)[c]		
Cuα_3D-CH3 + Ru(bpy)$_3$	1.15 (0.12)	10.5	1.18 (0.06)
Cuα_3D-CH4+ Ru(bpy)$_3$	0.74 (0.07)	6.7	1.15 (0.06)
Ru(phen)$_3$	0.18 (0.08)		
Cuα_3D-CH3 + Ru(phen)$_3$	1.07 (-)	5.9	0.88 (0.05)
Cuα_3D-CH4+ Ru(phen)$_3$	0.51 (0.06)	2.8	0.85 (0.04)
ZnTMPyP	0.036[d]		
Cuα_3D-CH3 + ZnTMPyP	0.79 (0.19)[d]	21.9	0.84 (0.04)
Cuα_3D-CH4 + ZnTMPyP	0.38 (0.01)[d]	10.5	0.81 (0.04)

[a]Derived from a kinetic trace at 400 nm and performed in duplicates. [b]Driving force: difference in the reduction potential of photo-oxidant and Cu-peptide. [c]Derived from kinetic trace at 450 nm. [c]Kinetic trace at 415 nm. The rates that do not contain an error were derived from a single experiment.

Discussion

Cupredoxin proteins function as electron transfer centers in many organisms, including plants, bacteria and humans. The semi-classical Marcus equation points to three factors that dictate the ET rate reorganization energy (λ_{total}), electronic coupling (H_{AB}) and driving force (-ΔG). These factors were determined to be significantly influenced by local (e.g., redox site) and global (e.g., fold and charge) protein structure. The $-\Delta$G is derived from the difference in the reduction potential of ET partners and biological driving force tends to be small. Therefore, for efficient ET, native proteins have evolved to optimize the λ_{total} and H_{AB} factors. In cupredoxins, the reorganization energy is controlled by forcing the copper center in an entatic state and a low dielectric environment. The coupling factor is enhanced through the incorporation of recognition or docking sites for their redox partners, which are composed of hydrophobic or acidic motifs on the protein surface that are conserved across the cupredoxin family. In this work, we examine the ET properties by determining such factors. Using protein film voltammetry, we determined

Cu(II/I) reduction potential values to show that our designed constructs are capable of serving as redox active molecules within the standard biological range. We then evaluated the intermolecular ET activity of these constructs with a photo-induced oxidant utilizing laser flash photolysis. This method allowed us to investigate further the ET properties of two designed constructs by determining the reorganization energy and coupling factor. Overall, this chapter aims to establish that we were successful in imparting the α_3D with a biologically relevant copper ET site.

Reduction Potential of Designed Constructs.

Cupredoxin centers possess positive reduction potential values that range from 180 – 800 mV (vs. NHE), producing highly redox active metal centers. The E° values of our designed constructs were determined using protein film voltammetry. These results are compared to the corresponding values of their native counterparts in Table IV-2, which were also derived from the same method. The values for α_3D-CR1, α_3D-CH3 and α_3D-CH4, which span from 364 to 399 mV, are similar to the reported values for native CuT1 proteins plastocyanin and azurin. Azurin has a weakly associated fifth carbonyl ligand from the peptide backbone. One of the key differences using helical bundles is that these carbonyl groups are unavailable due to H-bonding that are required to form the α-helix. Given that this extra ligand controls structure and potential, it is an important structural difference that cannot be emulated by a helical protein. However, clearly, this is not important for achieving the equivalent potential.

α_3D-ChC2 possesses a higher value of 462 mV. This reduction potential is only ~200 mV lower than rusticyanin, which is shown to display one of the highest reported E° values. This unique physical trait was attributed to the protein structure of the copper center. The metal binding loop of rusticyanin is extended compared to plastocyanin, and the extra residues form a "flap" that allows the copper site to be more buried, resulting in a high E° value. This observation can be also attributed to α_3D-ChC2. When compared to α_3D-CR1, α_3D-CH3 and α_3D-CH4, the metal-binding site of α_3D-ChC2 is placed one layer towards the N-terminal end and sandwiched between apolar residues (see Figure III-12C), thus producing a lower di-electric environment around the copper center. Moreover, the cyclic voltammograms of α_3D-ChC2 display less pronounced oxidation and reduction peaks (Figure IV-7D). The metal binding site

of α_3D-CR1, α_3D-CH3 and α_3D-CH4 are at the C-terminal of the bundle. These copper sites are ~15 Å from the terminal Cys residue that binds to the gold surface and their exposed site allow for facile ET. In contrast, the copper center of α_3D-ChC2 is ~25 Å from the terminal Cys, forcing the electron to traverse a longer distance, as well as several apolar residues.

Electrochemical Behavior of Designed Constructs.

In addition to observing the proper reduction potential, the PFV study showed that designed constructs undergo a quasi-reversible ET reaction with the gold surface. This behavior is demonstrated by peak-peak separations between the oxidized and reduced states in the trumpet plots. At fast scan rates, the corresponding peaks diverge, but this separation persists at slow scan rates, indicating a non-ideal ET process. A quasi-reversible ET reaction has been observed in plastocyanin grafted[9] and azurin[11] adsorbed on an electrode surface. In the latter example, the authors proposed two models that results in quasi-reversible reaction. The first model describes a sluggish redox reaction that occurs on the electrode surface during a fast ET reaction with the metal center. That is, as a potential is applied towards the reductive limit, the reductive peak of azurin is observed; and concurrently, the surface undergoes a redox reaction with an independent potential ($E°'_{surface}$). As the oxidative limit is reached, a corresponding peak is detected but with a modestly altered potential as a consequence of $E°'_{surface}$. Therefore, a peak separation perseveres at slow scan rates. The second model proposes that azurin is adsorbed on the surface in multiple conformations, and the population of each state affects the redox properties during ET. This model also accounts for broad peaks that the authors observed at slow scan rates, which were also present in this present work. We can propose that model 2 is a more likely scenario in this system and future work can be initiated to elucidate this electrochemical behavior. Overall, the results from the PFV study demonstrate that the desired reduction potential naturally observed in a β-barrel fold can be achieved within an unrelated *de novo* designed α-helical fold.

Electron Transfer Activity of Designed Constructs.

The electron transfer activity of α_3D-CR1, α_3D-CH3 α_3D-CH4 and α_3D-ChC2 with a photo-oxidant, $Ru(III)bpy)_3$, was examined using laser-flash photolysis. This highly oxidizing species is generated via an excitation to a triplet-excited state followed by an redox reaction with

an electron acceptor. This species can then interact with the Cu(I)-peptide complex via an ET reaction or recombine with the electron acceptor. To examine these reactions, we collected transient absorption spectra at varying time and absorption transients at varying wavelengths. The transient spectra of Cu(I) bound α_3D-CR1, α_3D-CH3 and α_3D-CH4 in Figure IV-10 show oxidation of the copper center by the photo-oxidant. This ET reaction is confirmed by the absorption band at ~400 nm in the transient spectra at 100 μs and the spectra produced from their kinetic traces, which correlates with their respective UV-vis spectra. Interestingly, the core-chelate construct, α_3D-ChC2, does not display ET activity with the photo-oxidant. Its transient spectra at 100 and 200 μs lack the strong absorption bands at 400 and 500 nm that were observed in the UV-vis experiments.

First order rates (k_{3app}) of decay of the photo-oxidant as a consequence of an ET reaction with the Cu(I)-peptide complex is determined by fitting the kinetic traces at 400 nm, where the Cu(II)-peptide absorbs, to a mono-exponential equation. Cuα_3D-CR1 and Cuα_3D-CH4 are 1.1 and 1.6, respectively, times faster at reducing the photo-oxidant than their apo form. This reveals that a protein oxidation is the rate-limiting step. Cuα_3D-ChC2 depletes the photo-oxidant at the same rate as its apo state. In contrast, Cuα_3D-CH3 is 2.9 times more efficient at performing the corresponding ET reaction, and its k_{3app} is almost one magnitude greater. Even though the kinetic rates of Cuα_3D-CR1 and Cuα_3D-CH4 are almost equivalent to their apo control, it is clear that their copper center is oxidized because a positive absorbance appears at 400 nm after the photo-oxidant has been completely reduced. On the other hand, Cuα_3D-ChC2 shows no sign of Cu(I) oxidation in its kinetic trace at 400 nm and transient spectra. The similarities of the first order rates constants can be attributed to the oxidation of the side chains of redox active residues (*e.g.*, Cys, His, Met, Trp and Tyr) or accessibility by the photo-oxidant. The Cys, His and Met residues make up the copper binding site, thus they are along the pathway for oxidation of the Cu(I) center and can be oxidized prior to the metal center. Tyr residues are present at the 45th and 70th position in construct α_3D-CR1. The 70th position is in the vicinity of the metal binding site, at the C-terminal end of the bundle, and can also serve as a conduit for ET, limiting the rate of this reaction. Tyr 45 and Trp 4 are at the N-terminal end and could act as non-productive ET pathways, which would diminish the rate of ET.

Table IV-7. Reduction potential and spectral features of amino acid radicals.

Amino Acid	$X^{\bullet}$/ +E° (mv vs. NHE)	pH	$X^{\bullet}$ λ (ε cm^{-1} M^{-1})
$Cys^{\bullet}$/Cys	920[47]	7.0	~330 nm (300 –1200)[48]
$His^{\bullet+}$/His	1170[49]	7.0	300 (5600), 360 (2000)[50] pH 5
$Met^{\bullet}$/Met	~1457[51]	8.2	380 – 390[52]
$Trp^{\bullet+}$/Trp	1015[53]	7.0	335 (4750), 560 (3000)[54] pH 3 $TRPH^{\bullet+}$ 325 (3670), 510 (2300)[54] pH 7-10 $TRP^{\bullet}$
$Tyr^{\bullet+}$/Tyr	930[53]	7.0	~280 (~4500), 410 (~3000)[55] pH 7.8 TyrOH → $TyrO^{\bullet}$

The formation of amino acid radicals is a feature observed in many biological processes including photosynthesis and synthesis of deoxyribonucleotide. Table IV-7 summarizes the reduction potential (at relevant pH conditions) redox active amino acid residues and the absorption features of their radical form. The apo form of α_3D-CR1 has several redox active residues: Cys28, His18 and 67, Met72, Trp4 and Tyr45 and 70. Tyrosine 70 is at the C-terminal end near the 2HisCysMet metal binding site and Trp4 and Tyr45 are located at the N-terminal end of the bundle. Because Cys and Tyr residues possess lower reduction potential values, their side chain is the most likely the target for the photo-oxidant. The transient spectra of apo α_3D-CR1 (Figure IV-16A) show no clear indications of a Tyr70 radical. The generated spectrum displays a weak band between 375 – 410 nm, but this feature stems from the photo-oxidant as indicated by the negative absorbance at 450 nm (see Figure IV-16A, 100 ns spectrum). That is, this spectrum contains the excited state of the chromophore. Cys radical absorbs at 330 nm, a wavelength that could not be experimentally measured with the photophysical apparatus. Cys28 can nevertheless serve as the ET partner of the photo-oxidant. The next likely residue is the Trp 4 residue, which forms a radical that absorbs at ~510 nm (deprotonated, neutral species). The transient spectra in Figure IV-16A do not exhibit the presence of a Trp radical. In addition, Table IV-8 shows that the oxidation rate of the photo-oxidant is uniform (10^5 s^{-1}) from 360 – 450 nm, suggesting that the system is undergoing one reaction (Eq. IV-3). Even though the oxidation of a redox active residues were not observed, the k_{3app} of apo α_3D-CR1 and Cuα_3D-CR1 are similar in values, which suggests that the oxidation of the copper center of Cu(I)α_3D-CR1 is preceded by

an ET reaction between the peptide and the photo-oxidant. In native cupredoxins, the highly covalent Cu-S(Cys) bond have been proposed to function as a super-exchange pathway for electron transfer.[56] Since a Tyr or Trp radical is not observed, it is possible that the bound Cys of α_3D-CR1 serves as conduit for ET between the photo-oxidant and Cu(I) metal ion (Figure IV-17A). A similar hypothesis can be made for α_3D-CH3 and α_3D-CH4 (Figure IV-17B).

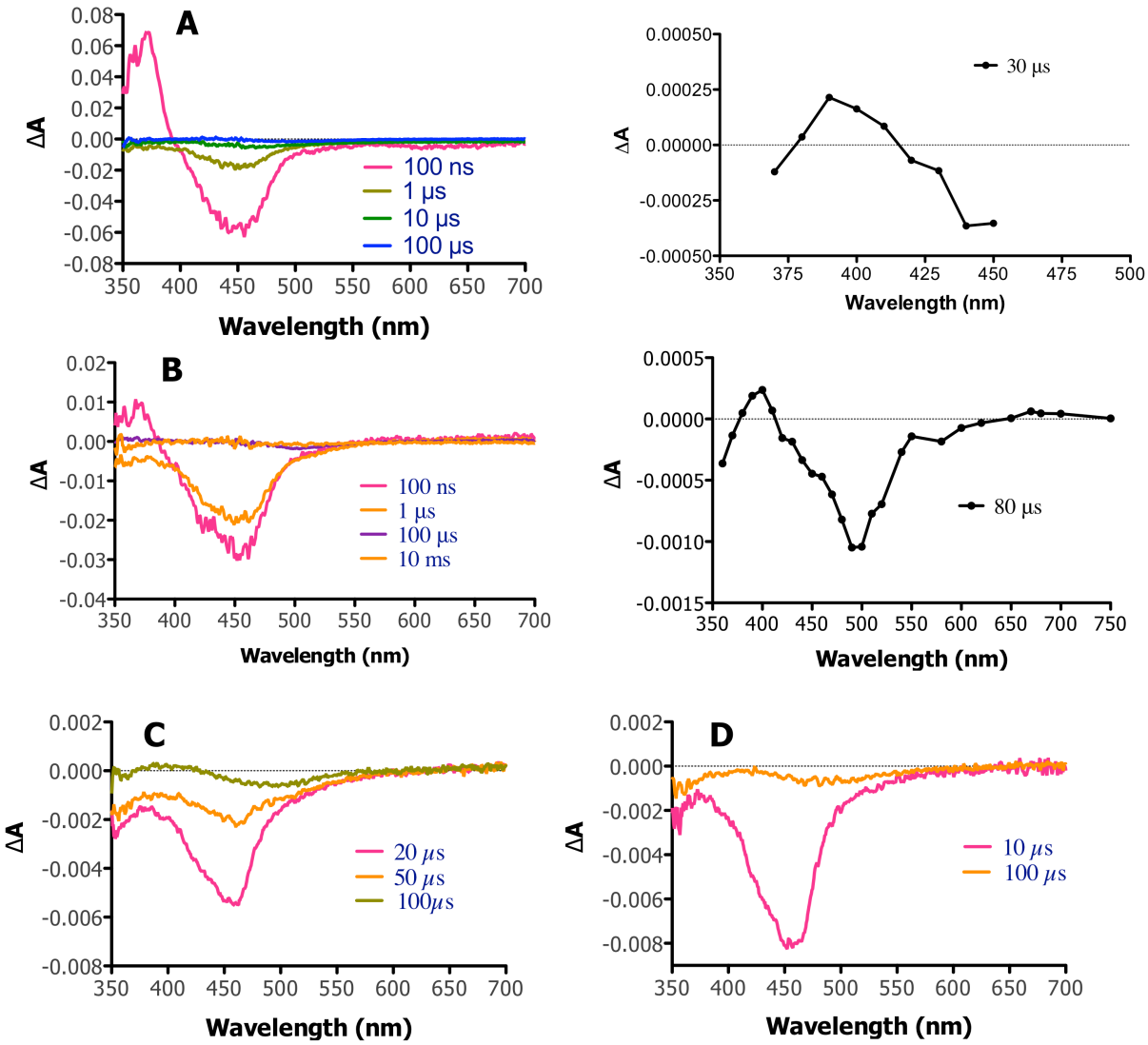

Figure IV–16. Transient spectra of apo proteins. A) α_3D-CR1 and on the right spectrum generated from kinetic traces, which displays an absorption band at 380 nm that stems from the photo-oxidant. B) α_3D-CH3 and generated spectrum on the right. Again the generated spectrum shows the presence of the photo-oxidant. C) α_3D-CH4. D) α_3D-ChC2.

Table IV-8. First-order rate constant of Cuα_3D-CR1 at varying wavelengths.

λ	k_{3app} (x10^5 s^{-1})[a]	λ	k_{3app} (x10^5 s^{-1})[a]
360	3.66	410	3.72
370	3.62	420	4.27
380	3.70	430	4.25
390	3.82	440	4.13
400	3.83	450	3.98

[a]500 μM Cu(I)-peptide.

The kinetic trace at 400 nm of Cuα_3D-CR1 and Cuα_3D-CH3 show formation of a prominent absorbance when compared to Cuα_3D-CH4 and Cuα_3D-ChC2. This observation can be attributed to the accessibility of the copper center by the photo-oxidant. The 2HisCys metal binding residues of α_3D-CR1 are located on three separate strands and could cause the C-terminal end of the bundle to expand, allowing the Cu(I) center to be more easily accessible (see Figure III-12). Similarly, Cuα_3D-CH3 contains a His18-X_2-Cys21 chelate motif and the location of the Cys residue on the loop could result in a more solvent exposed Cu(I) site, therefore providing facile interaction with the photo-oxidant. The second chelate construct, Cuα_3D-CH4, has the corresponding chelate group, but inverted. This construct moves the Cys residue to the 18th position toward the core of the bundle and places the bulkier His ligand in the 21st position. It is conceivable that the Cu(I) center of α_3D-CH4 is somewhat more buried than in α_3D-CH3 and is not as accessible by the photo-oxidant, resulting in a less intense absorption profile as observed in its transient spectra. As previously described, Cuα_3D-ChC2, incorporates the 2HisCys metal binding site deep inside the hydrophobic core of the bundle, one layer removed from the C-terminal end. To access the Cu(I) adduct of Cuα_3D-ChC2, the photo-oxidant would require side-on approach at the helical interface of the peptide, which could be deterred by the salt-bridges between the helices and packing of the hydrophobic residues that encapsulate this metal center (Figure IV-17C).

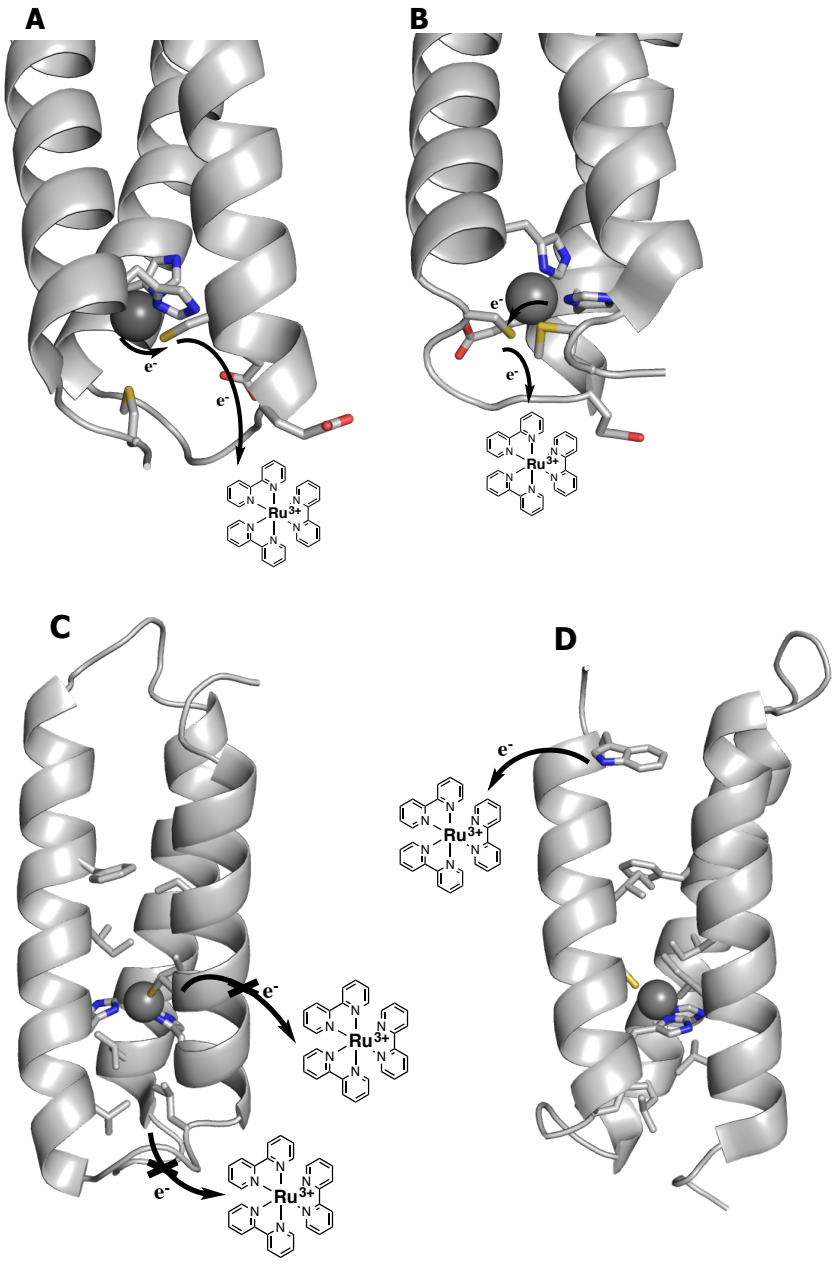

Figure IV–17. Proposed electron transfer pathway in designed constructs. A) The Cys residue in the metallated form of α_3D-CR1 could facilitate ET between the Cu(I) center and photo-oxidant. B) For Cuα_3D-CH3, the Cys residue can also provide a pathway for ET. C) The Cu(I) center of α_3D-ChC2, which is encapsulated by apolar residues, is not accessible to the photo-oxidant. D) It is likely that the Trp residue of apo and metallated α_3D-ChC2 is responsible for reducing the photo-oxidant.

Furthermore, the kinetic trace at 400 nm of apo and Cuα_3D-ChC2 provide insight into the oxidation of all the apo forms and could prove to be not as straightforward as previously discussed. The first order rate constants (k_{3app}) of the apo form of α_3D-CR1 and α_3D-CH4, as well as α_3D-ChC2 were described as originating from the oxidation of amino acid side chains by

the photo-oxidant, most like the Cys ligand. The k_{3app} values of apo α_3D-ChC2 and Cuα_3D-ChC2 are nearly identical (see Table IV-5). Accordingly, if the photo-oxidant can oxidize the Cys residue of apo α_3D-ChC2, it is also conceivable that the Cu(I) center in the metallated form can be accessed in a similar manner. However, the transient spectra and kinetic traces for Cuα_3D-ChC2 lack the signature for a Cu(II) species. It is possible that in both the apo and metallated form that Trp4 reduces the photo-oxidant as shown in Figure IV-17D. Using mutated derivatives of this peptide system, future work could focus on elucidating the ET mechanism of the CuT1 models. Nonetheless, despite the unclear nature of the apoprotein experiments and ET pathway, the copper center of α_3D-CR1, α_3D-CH3 and α_3D-CH4 were successful in participating in an intermolecular ET reaction with Ru(III)(bpy)$_3$. The bimolecular rate constants of these reactions are compared in Table IV-9 to its native counterparts that were derived from a similar measurement (but without the use of an electron acceptor). This comparison shows that the designed constructs reduces Ru(bpy)$_3$ species with similar efficiency as plastocyanin, azurin and stellacyanin.

Table IV-9. Bimolecular rate constant of designed constructs.

Sample	$k_{ET\ app}$ (x10^8 M^{-1} s^{-1})
Cuα_3D-CR1[a]	7.6
Cuα_3D-CH3[b]	6.2
Cuα_3D-CH4[c]	7.4
Plastocyanin[d 57]	19
Azurin[d 57]	6.5
Stellacyanin[d 57]	4.0

[a]500 μM Cu(I)-peptide. [b]Determined from the rate versus concentration study. [c]100 μM Cu(I)-peptide. [d]Sensitizer [*Ru(bpy)$_3$]$^{2+}$, Cu(I)-protein, pH 7.0 and 25 °C, ref 55.

Effect of Concentration on Rate.

The effect of concentration on rate was performed to determine the second order rate constant for Cuα_3D-CH3 and examine if the ET rate increases with the Cu-P concentration, which is indicative of a bimolecular reaction. The rate versus concentration plot (Figure IV-12A) shows that the rate modestly saturates at 400 μM Cu-P concentration. An alternative explanation to the saturation of the rate at high concentrations is the gated mechanism.[58, 59] This process

occurs when the ET step is coupled to non-ET adiabatic reactions, such as a slow conformational or chemical change, thereby influencing the rate of ET. Such reactions will alter ET parameters including the driving force, reorganization energy and coupling because ET is not the rate-limiting step. Gated ET reactions have been observed in multi-exponential decay of an excited stated[60] and in other reports that varied the sample condition, such viscosity or pressure, to ascertain the conformational steps prior to ET.[61-63] Therefore, it is possible that at high Cu-P concentrations the ET reaction between the copper center and the photo-oxidant is gated by a global conformational change that is not apparent in the kinetic traces. The conformation change could be a consequence of a decrease in the protein or diffusion motion as a consequence of a more "viscous" condition at higher concentrations, affecting the interaction Cu-P and $Ru(III)(bpy)_3^{3+}$.

Implications of the Reorganization Energy on Design.

The reorganization energy of $Cu\alpha_3$D-CH3 and $Cu\alpha_3$D-CH4 were obtained from the rate versus driving force study. This parameter was determined by applying the Marcus equation to the rate versus driving force plot. Table IV-10 compares the reorganization energy of the designed constructs to its native counterparts and an inorganic compound. $Cu\alpha_3$D-CH3 and $Cu\alpha_3$D-CH4 have λ values that are ~1.2 eV lower than $[Cu(phen)_2]^{2+}$. Compared to native cupredoxins and cytochrome *c*, the designed constructs are equivalent to the upper limit and ~0.5 eV higher than the lower limit. This comparison shows that we can achieve ET reorganization energy within a comparable range as native proteins. However, note that these are approximate λ values and future work is required to develop this study fully, which would require the use of additional photo-oxidants to add more data points on the rate versus driving force plots. By doing so, the fit to Marcus equation will improve and provide a more precise value for the reorganization energy.

Nevertheless, the approximate λ values offer insight into the geometry change during electron transfer. In chapter 3, from the XAS analysis, the Cu(I) adducts of $Cu\alpha_3$D-CH3 and $Cu\alpha_3$D-CH4 show a similar coordination environment as its native counterparts. However, the absorption spectra of the Cu(II) state reveals the formation of tetragonal or square planar species.

The 2.4 eV of $[Cu(phen)_2]^{2+}$ stems from a tetrahedral to a pure tetragonal geometry during ET. Since the corresponding value of Cuα_3D-CH3 and Cuα_3D-CH4 is ~1.2 eV lower, it can be proposed that the copper coordination environment of these constructs requires less geometry change, and instead, transitions between a pseudo-tetrahedral and pseudo-tetragonal geometry. Therefore, future CuT1 designs will focus on forcing the Cu(II) state into a tetrahedral geometry in order to lower the reorganization energy between the Cu(II/I) couple.

Table IV-10. Reorganization energy of designed constructs.

Complex	λ (eV)
Cuα_3D-CH3	1.05
Cuα_3D-CH4	1.21
$[Cu(phen)_2]^{2+}$ [29]	2.4
Plastocyanin and Azurin[30, 33, 34, 64]	0.7 – 1.2
Cytochrome *c*[65]	0.74

Conclusion

The main goal in this chapter was to characterize the redox and electron transfer properties of the designed constructs α_3D-CR1, α_3D-CH3, α_3D-CH4 and α_3D-ChC2. The first objective was to determine the Cu(II/I) reduction potential of such constructs, and this was achieved using protein film voltammetry. From this study, it was determined that Cuα_3D-CR1, Cuα_3D-CH3, Cuα_3D-CH4 have E° values that range from 364 – 399 mV, which are within the observed values for plastocyanin and azurin. This result shows that redox properties that are naturally observed in β-barrel fold, with accessible carbonyl groups from the protein backbone, can be achieved in an α-helical bundle. The more buried copper center of α_3D-ChC2 possesses a much higher E° value of 462 mV. Overall, this result exhibits the success of building a metal center with the proper redox property within an unrelated protein α-helical fold.

Moreover, the ET activity of α_3D-CR1, α_3D-CH3, α_3D-CH4 and α_3D-ChC2 were examined using flash-laser photolysis. It was observed from the transient spectra of Cuα_3D-CR1, Cuα_3D-CH3 and Cuα_3D-CH4 that the copper center of these constructs participated in an ET

reaction with the photo-oxidant. However, Cuα_3D-ChC2 showed no sign of ET, which is attributed to an inaccessible copper center. The first order rate constants (k_{3app}), which is related to the reduction of the photo-oxidant and the appearance of a Cu(II) species, of Cuα_3D-CR1, Cuα_3D-CH3 and Cuα_3D-CH4 are 10^5 s^{-1} and the corresponding bimolecular rate constants are 10^8 M^{-1} s^{-1}, which are comparable to the reported values for native cupredoxins. Additionally, approximate values of the ET reorganization energy of Cuα_3D-CH3 and Cuα_3D-CH4 were determined. These values are ~1.2 eV lower than the same parameter for a copper compound, $[Cu(phen)_2]^{2+}$ and equivalent to or ~0.5 eV higher than native ET proteins.

References

[1] Marcus, R. A., and Sutin, N. (1985) Electron transfers in chemistry and biology, *Biochim. Biophys. Acta, Rev. Bioenerg. 811*, 265-322.

[2] Marcus, R. A. (1993) Electron transfer reactions in chemistry. Theory and experiment, *Rev. Mod. Phys. 65*, 599-610.

[3] Gray, H. B., and Winkler, J. R. (2003) Electron tunneling through proteins, *Q. Rev. of Biophys. 36*, 341-372.

[4] Sykes, A. G. (1985) Tilden Lecture. Structure and electron-transfer reactivity of the blue copper protein plastocyanin, *Chem. Soc. Rev. 14*, 283.

[5] Sailasuta, N., Anson, F. C., and Gray, H. B. (1979) Studies of the thermodynamics of electron transfer reactions of blue copper proteins, *J. Am. Chem. Soc. 101*, 455-458.

[6] Olesen, K., Veselov, A., Zhao, Y., Wang, Y., Danner, B., Scholes, C. P., and Shapleigh, J. P. (1998) Spectroscopic, kinetic, and electrochemical characterization of heterologously expressed wild-type and mutant forms of copper-containing nitrite reductase from *Rhodobacter sphaeroides* 2.4.3, *Biochemistry 37*, 6086-6094.

[7] Xu, F., Berka, R. M., Wahleithner, J. A., Nelson, B. A., Shuster, J. R., Brown, S. H., Palmer, A. E., and Solomon, E. I. (1998) Site-directed mutations in fungal laccase: effect on redox potential, activity and pH profile, *Biochem. J 334 (Pt 1)*, 63-70.

[8] Anderson, G. P., Sanderson, D. G., Lee, C. H., Durell, S., Anderson, L. B., and Gross, E. L. (1987) The effect of ethylenediamine chemical modification of plastocyanin on the rate of cytochrome *f* oxidation and P-700$^+$ reduction, *Biochim. Biophys. Acta 894*, 386-398.

[9] Andolfi, L., Bruce, D., Cannistraro, S., Canters, G. W., Davis, J. J., Hill, H. A. O., Crozier, J., Verbeet, M. P., Wrathmell, C. L., and Astier, Y. (2004) The electrochemical characteristics of blue copper protein monolayers on gold, *J. Electroanal. Chem. 565*, 21-28.

[10] Pascher, T., Karlsson, B. G., Nordling, M., Malmström, B. G., and Vanngard, T. (1993) Reduction potentials and their pH dependence in site-directed-mutant forms of azurin from *Pseudomoms aeruginosa*, *Euro. J. Biochem. 212*, 289-296.

[11] Jeuken, L. J. C., and Armstrong, F. A. (2001) Electrochemical Origin of Hysteresis in the Electron-Transfer Reactions of Adsorbed Proteins: Contrasting Behavior of the "Blue" Copper Protein, Azurin, Adsorbed on Pyrolytic Graphite and Modified Gold Electrodes, *J. Phys. Chem. B 105*, 5271-5282.

[12] Lappin, A. G., Lewis, C. A., and Ingledew, W. J. (1985) Kinetics and mechanisms of reduction of rusticyanin, a blue copper protein from *Thiobacillus ferrooxidans*, by inorganic cations, *Inorg. Chem. 24*, 1446-1450.

[13] Lu, Y. (2003) Electron Transfer Cupredoxin, In *Comprehensive Coordination Chemistry II: From Biology to Nanotechnology* (Que, J., L., and Tolman, W. B., Eds.), pp 91-122, Elsevier Ltd., San Diego, CA, USA.

[14] Solomon, E. I., Szilagyi, R. K., DeBeer George, S., and Basumallick, L. (2004) Electronic structures of metal sites in proteins and models: contributions to function in blue copper proteins, *Chem. Rev. 104*, 419-458.

[15] Hall, J. F., Kanbi, L. D., Strange, R. W., and Hasnain, S. S. (1999) Role of the Axial Ligand in Type 1 Cu Centers Studied by Point Mutations of Met148 in Rusticyanin, *Biochemistry 38*, 12675-12680.

[16] Marshall, N. M., Garner, D. K., Wilson, T. D., Gao, Y. G., Robinson, H., Nilges, M. J., and Lu, Y. (2009) Rationally tuning the reduction potential of a single cupredoxin beyond the natural range, *Nature 462*, 113-116.

[17] Arciero, D. M., Pierce, B. S., Hendrich, M. P., and Hooper, A. B. (2002) Nitrosocyanin, a red cupredoxin-like protein from Nitrosomonas europaea, *Biochemistry 41*, 1703-1709.

[18] King, J. D., McIntosh, C. L., Halsey, C. M., Lada, B. M., Niedzwiedzki, D. M., Cooley, J. W., and Blankenship, R. E. (2013) Metalloproteins diversified: the auracyanins are a family of

cupredoxins that stretch the spectral and redox limits of blue copper proteins, *Biochemistry 52*, 8267-8275.
[19] Kyritsis, P., Lundberg, L. G., Nordling, M., Vänngård, T., Young, S., Tomkinson, N. P., and Sykes, A. G. (1991) The reactivity of spinach plastocyanin mutants with inorganic oxidants $[Fe(CN)_6]_3$ and $[Co(phen)_3]^{3+}$, *J. Chem. Soc., Chem. Commun.*, 1441.
[20] Kyritsis, P., Dennison, C., McFarlane, W., Nordling, M., Vanngard, T., Young, S., and Sykes, A. G. (1993) Reactions of five spinach plastocyanin PCu(I) mutants with $[Fe(CN)_6]_3$ and $[Co(phen)_3]^{3+}$ (phen = 1,10-phenanthroline) and related studies, *J. Chem. Soc., Dalton Trans.*, 2289.
[21] He, S., Modi, S., Bendall, D. S., and Gray, J. C. (1991) The surface-exposed tyrosine residue Tyr83 of pea plastocyanin is involved in both binding and electron transfer reactions with cytochrome *f*, *EMBO J. 10*, 4011-4016.
[22] Gong, X.-S., Wen, J. Q., Fisher, N. E., Young, S., Howe, C. J., Bendall, D. S., and Gray, J. C. (2000) The role of individual lysine residues in the basic patch on turnip cytochrome f for electrostatic interactions with plastocyanin in vitro, *Euro. J. Biochem. 267*, 3461-3468.
[23] Gong, X.-S., Wen, J. Q., and Gray, J. C. (2000) The role of amino-acid residues in the hydrophobic patch surrounding the haem group of cytochrome f in the interaction with plastocyanin, *Euro. J. Biochem. 267*, 1732-1742.
[24] Nordling, M., Sigfridsson, K., Young, S., Lundberg, L. G., and Hansson, Ö. (1991) Flash-photolysis studies of the electron transfer from genetically modified spinach plastocyanin to photosystem I, *FEBS Lett. 291*, 327-330.
[25] Ejdebäck, M., Bergkvist, A., Karlsson, B. G., and Ubbink, M. (2000) Side-Chain Interactions in the Plastocyanin–Cytochrome *f* Complex, *Biochemistry 39*, 5022-5027.
[26] Ubbink, M. (2011) Cytochromef/Plastocyanin Complex.
[27] Hart, P. J., Nersissian, A. M., and George, S. D. (2011) Copper Proteins with Type 1 Sites, *Encyclopedia of Inorganic and Bioinorganic Chemistry*.
[28] Szilagyi, R. K., and Solomon, E. I. (2002) Electronic structure and its relation to function in copper proteins, *Curr. Opin. Chem. Biol. 6*, 250-258.
[29] Winkler, J. R., Wittung-Stafshede, P., Leckner, J., Malmstrom, B. G., and Gray, H. B. (1997) Effects of folding on metalloprotein active sites, *Proc. Natl. Acad. Sci. U. S. A. 94*, 4246-4249.
[30] Di Bilio, A. J., Hill, M. G., Bonander, N., Karlsson, B. G., Villahermosa, R. M., Malmström, B. G., Winkler, J. R., and Gray, H. B. (1997) Reorganization Energy of Blue Copper: Effects of Temperature and Driving Force on the Rates of Electron Transfer in Ruthenium- and Osmium-Modified Azurins, *J. Am. Chem. Soc. 119*, 9921-9922.
[31] Bjerrum, M. J., Casimiro, D. R., Chang, I. J., Di Bilio, A. J., Gray, H. B., Hill, M. G., Langen, R., Mines, G. A., Skov, L. K., Winkler, J. R., and et al. (1995) Electron transfer in ruthenium-modified proteins, *J. Bioenerg. Biomembr. 27*, 295-302.
[32] Regan, J. J., Di Bilio, A. J., Langen, R., Skov, L. K., Winkler, J. R., Gray, H. B., and Onuchic, J. N. (1995) Electron tunneling in azurin: the coupling across a β-sheet, *Chem. Biol. 2*, 489-496.
[33] Skov, L. K., Pascher, T., Winkler, J. R., and Gray, H. B. (1998) Rates of Intramolecular Electron Transfer in Ru(bpy)2(im)(His83)-Modified Azurin Increase below 220 K, *J. Am. Chem. Soc. 120*, 1102-1103.
[34] Sigfridsson, K., Ejdebäck, M., Sundahl, M., and Hansson, Ö. (1998) Electron Transfer in Ruthenium-Modified Spinach Plastocyanin Mutants, *Arch. Biochem. Biophys. 351*, 197-206.
[35] Larsson, S. (1983) Electron transfer in proteins, *J. Chem. Soc., Faraday Trans. 279*, 1375.
[36] Fraga, E., Webb, M. A., and Loppnow, G. R. (1996) Charge-Transfer Dynamics in Plastocyanin, a Blue Copper Protein, from Resonance Raman Intensities, *J. Phys. Chem. 100*, 3278-3287.
[37] Sigfridsson, E., Olsson, M. H. M., and Ryde, U. (2001) A Comparison of the Inner-Sphere Reorganization Energies of Cytochromes, Iron–Sulfur Clusters, and Blue Copper Proteins, *J. Phys. Chem. B 105*, 5546-5552.

[38] Olsson, M. H. M., Ryde, U., Roos, B. O., and Pierloot, K. (1998) On the relative stability of tetragonal and trigonal Cu(II) complexes with relevance to the blue copper proteins, *J. Biol. Inorg. Chem. 3*, 109-125.
[39] Randall, D. W., Gamelin, D. R., LaCroix, L. B., and Solomon, E. I. (1999) Electronic structure contributions to electron transfer in blue Cu and Cu_A, *J. Biol. Inorg. Chem. 5*, 16-19.
[40] Armstrong, F. A. (2002) Insights from protein film voltammetry into mechanisms of complex biological electron-transfer reactions, *J. Chem. Soc., Dalton Trans.*, 661-671.
[41] Kalyanasundaram, K. (1982) Photophysics, photochemistry and solar energy conversion with tris(bipyridyl)ruthenium(II) and its analogues, *Coord. Chem. Rev. 46*, 159-244.
[42] Creutz, C., and Sutin, N. (1976) Electron-transfer reactions of excited states: direct evidence for reduction of the charge-transfer excited state of tris(2,2'-bipyridine)ruthenium(II), *J. Am. Chem. Soc. 98*, 6384-6385.
[43] Lide, D. R. (2004) CRC Handbook of Chemistry and Physics, Internet Version 2005, In *CRC Handbook of Chemistry and Physics* (Lide, D. R., Ed.) 85 ed., CRC Press Boca Raton, FL, 2005.
[44] Herrero, C., Quaranta, A., Fallahpour, R.-A., Leibl, W., and Aukauloo, A. (2013) Identification of the Different Mechanisms of Activation of a $[RuII(tpy)(bpy)(OH_2)]^{2+}$ Catalyst by Modified Ruthenium Sensitizers in Supramolecular Complexes, *J. Phys. Chem. C 117*, 9605-9612.
[45] Winkler, K., McKnight, N., and Fawcett, W. R. (2000) Electron Transfer Kinetics of Tris(1,10-phenanthroline)ruthenium(II) Electrooxidation in Aprotic Solvents, *J. Phys. Chem. B 104*, 3575-3580.
[46] Subbaiyan, N. K., and D'Souza, F. (2012) Light-to-electron converting panchromatic supramolecular solar cells of phthalocyanine-porphyrin heterodimers adsorbed onto nanocrystalline SnO_2 electrodes, *Chem. Commun. 48*, 3641-3643.
[47] Surdhar, P. S., and Armstrong, D. A. (1987) Reduction potentials and exchange reactions of thiyl radicals and disulfide anion radicals, *J. Phys. Chem. 91*, 6532-6537.
[48] Wardman, P., and von Sonntag, C. (1995) [3] Kinetic factors that control the fate of thiyl radicals in cells, *Methods in Enzymol. 251*, 31-45.
[49] Navaratnam, S., and Parsons, B. J. (1998) Reduction potential of histidine free radicals: a pulse radiolysis study, *J. Chem. Soc., Faraday Trans. 94*, 2577-2581.
[50] Rao, P. S., Simic, M., and Hayon, E. (1975) Pulse radiolysis study of imidazole and histidine in water, *J. Phys. Chem. 79*, 1260-1263.
[51] Schoneich, C. (2002) Redox processes of methionine relevant to beta-amyloid oxidation and Alzheimer's disease, *Arch. Biochem. Biophys. 397*, 370-376.
[52] Chatgilialoglu, C., Castelhano, A. L., and Griller, D. (1985) Structures and optical absorption spectra of some sulfuranyl radicals in solution, *J. Org. Chem. 50*, 2516-2518.
[53] Harriman, A. (1987) Further comments on the redox potentials of tryptophan and tyrosine, *J. Phys. Chem. 91*, 6102-6104.
[54] Solar, S., Getoff, N., Surdhar, P. S., Armstrong, D. A., and Singh, A. (1991) Oxidation of tryptophan and N-methylindole by $N_3^{\bullet}$, $Br2^{\bullet-}$, and $(SCN)_2^{\bullet-}$ radicals in light- and heavy-water solutions: a pulse radiolysis study, *J. Phys. Chem. 95*, 3639-3643.
[55] Candeias, L. P., Turconi, S., and Nugent, J. H. A. (1998) Tyrosine YZ and YD of photosystem II: Comparison of optical spectra to those of tyrosine oxidised by pulsed radiolysis, *Biochim. Biophys. Acta, Bioenerg. 1363*, 1-5.
[56] Holm, R. H., Kennepohl, P., and Solomon, E. I. (1996) Structural and Functional Aspects of Metal Sites in Biology, *Chem. Rev. 96*, 2239-2314.
[57] Brunschwig, B. S., DeLaive, P. J., English, A. M., Goldberg, M., Gray, H. B., Mayo, S. L., and Sutin, N. (1985) Kinetics and mechanisms of electron transfer between blue copper proteins and electronically excited chromium and ruthenium polypyridine complexes, *Inorg. Chem. 24*, 3743-3749.
[58] Hoffman, B. M., and Ratner, M. A. (1987) Gated electron transfer: when are observed rates controlled by conformational interconversion?, *J. Am. Chem. Soc. 109*, 6237-6243.

[59] Davidson, V. L. (2000) What Controls the Rates of Interprotein Electron-Transfer Reactions, *Acc. Chem. Res. 33*, 87-93.
[60] Zhou, J. S., and Kostic, N. M. (1993) Gating of photoinduced electron transfer from zinc cytochrome *c* and tin cytochrome *c* to plastocyanin. Effects of solution viscosity on rearrangement of the metalloprotein complex, *J. Am. Chem. Soc. 115*, 10796-10804.
[61] Qin, L., and Kostic, N. M. (1994) Photoinduced electron transfer from the triplet state of zinc cytochrome c to ferricytochrome b5 is gated by configurational fluctuations of the diprotein complex, *Biochemistry 33*, 12592-12599.
[62] Pletneva, E. V., Fulton, D. B., Kohzuma, T., and Kostić, N. M. (2000) Protein Docking and Gated Electron-Transfer Reactions between Zinc Cytochromecand the New Plastocyanin from the FernDryopteris crassirhizoma. Direct Kinetic Evidence for Multiple Binary Complexes, *J. Am. Chem. Soc. 122*, 1034-1046.
[63] Leferink, N. G., Pudney, C. R., Brenner, S., Heyes, D. J., Eady, R. R., Samar Hasnain, S., Hay, S., Rigby, S. E., and Scrutton, N. S. (2012) Gating mechanisms for biological electron transfer: integrating structure with biophysics reveals the nature of redox control in cytochrome P450 reductase and copper-dependent nitrite reductase, *FEBS Lett. 586*, 578-584.
[64] McCleskey, T. M., Winkler, J. R., and Gray, H. B. (1992) Driving-force effects on the rates of bimolecular electron-transfer reactions, *J. Am. Chem. Soc. 114*, 6935-6937.
[65] Mines, G. A., Bjerrum, M. J., Hill, M. G., Casimiro, D. R., Chang, I. J., Winkler, J. R., and Gray, H. B. (1996) Rates of Heme Oxidation and Reduction in Ru(His33)cytochrome *c* at Very High Driving Forces, *J. Am. Chem. Soc. 118*, 1961-1965.

Chapter V. Conclusions

Summary

Proteins acquire metal ions to perform essential functions in nature, including catalysis, signal transduction, transport and storage of small molecules and redox chemistry. *De novo* protein design offers an exciting and biologically relevant approach to examine the metal centers of native metalloproteins. This approach involves the design and synthesis of a peptide from scratch, allowing one to model and achieve the function of a desired metal center in a simplified protein scaffold. Moreover, the designed metal binding site is retained within a hydrophobic environment much like in native proteins, the chemistry is performed in aqueous solutions at pertinent pH conditions, and the designed constructs can be mass produced (in grams) using mild protein expression reagents. The field of *de novo* metalloproteins and enzymology has made great advances over the past decade[1-3] and promises the future capability of preparing multicenter redox enzymes designed from first principles. At present, well-defined and well-folded scaffolds have been made available for helical bundle motifs,[4-7] with the α_3D[8] system being an excellent example.

Recent work in the Pecoraro group by Chakraborty *et al.* (α_3D**IV**)[9] and Cangelosi *et al.* (α_3D$\mathbf{H_3}$)[10] produced derivatives of the α_3D scaffold that served as excellent functional models of native metalloregulatory proteins and carbonic anhydrase. However, fundamental understanding of α_3D**IV** and metal site structures was lacking. To resolve this issue, I solved the structure of apo α_3D**IV** to understand how the original α_3D framework can tolerate modification in order to serve as a structural/functional scaffold for future designed metalloproteins and metalloenzymes.[11] After establishing that α_3D**IV** is a well-defined scaffold, in Chapter 3, I utilized this structure to design an asymmetric metal binding site found in the ET center of

cupredoxin proteins. The main objective is to expand the functional scope of the α_3D family by sculpting an ET site within this framework. Finally, in Chapter 4, the ET capability of such constructs was tested using electrochemical and photophysical techniques. This work is summarized in Figure V-1.

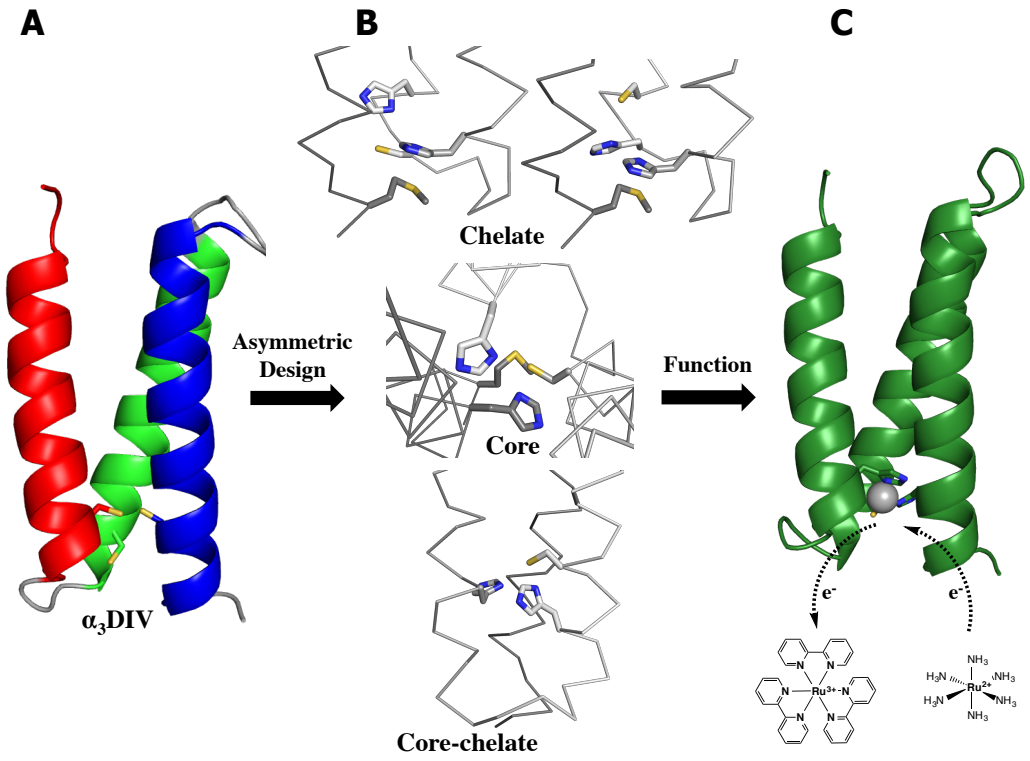

Figure V-1. Scheme summarizing the overall objectives of this thesis. A) Chapter 2 described the structure determination of apo α_3D**IV**,[11] demonstrating that sculpting a metal-binding site within α_3D produces a well-defined scaffold. B) In Chapter 3, the structure of α_3D**IV** was used as the base for designing an asymmetric metal binding site found in native ET cupredoxin proteins, and these constructs were characterized using several biophysical methods. C) In Chapter 4, the redox property and ET transfer activity of the designed constructs were investigated utilizing electrochemistry and photophysics.

As described in Chapter 2, the structure of α_3D**IV** comprised 1067 NOE restraints obtained from several multinuclear, multidimensional NMR experiments, as well as 138 predicted dihedral angles (ψ, ϕ and χ_1). The backbone and heavy atoms of the 20 lowest energy structures have an RMSD from the mean structure of 0.79 (0.16) Å and 1.31 (0.15) Å, respectively, exhibiting a high quality structure. Further, the Ramachandran statistics for the 20

structures show that 90.1% of the backbone stereochemistry is in the favored regions. A structural comparison to the parent structure α_3D revealed that α_3D**IV** still retains the same overall topology and fold, and interestingly, the substitution of Leu residues to Cys increased the overall α-helical content of the structure. This comparison also showed that the α_3D**IV** structure has decreased interhelical-tilts by 7° – 16° (Figure V-2A), causing a more packed apolar core (see Figure II-13). As shown in Figure V-2B, the structure of α_3D**IV** displays a distorted triscysteine metal binding sit and could result in the formation of "asymmetric" metal complexes, which was observed in the EXAFS analysis on Hg(II)-α_3D**IV**. The EXAFS work generated an average Hg(II)-S bond length at 2.36 Å that is indicative of a trigonal T-shaped coordination environment, with two short and one long (from Cys 28) Hg-S bonds. Moreover, thermal denaturation studies on metallated α_3D**IV** species showed an increase in the melting temperatures of Hg(II), Pb(II), or Cd(II) bound α_3D**IV** by a range of 18 – 24 °C. This result demonstrates metal-induced stability. Overall, the α_3D**IV** structure represents a major advancement in the field of biomimetic, providing a model for native metalloregulatory proteins with thiol-rich metal binding sites.

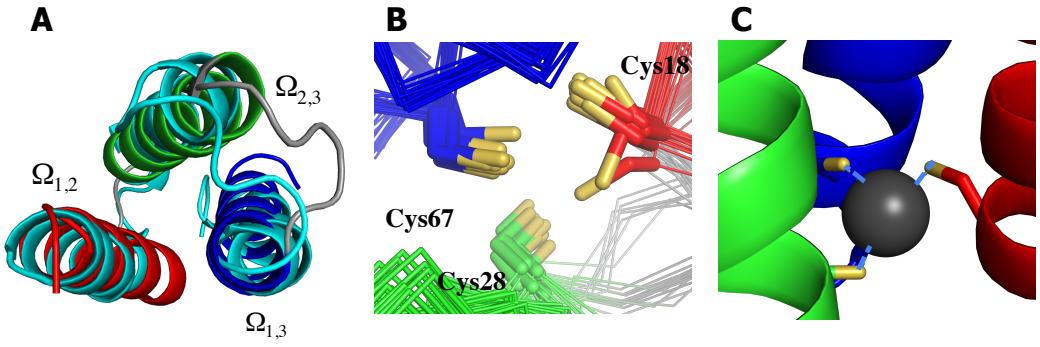

Figure V-2. A) α_3D**IV** (red, green and blue) overlaid with α_3D (cyan). This comparison shows that α_3D**IV** retains an antiparallel topology after the incorporation of 3Cys site. Moreover, the α_3D**IV** structure demonstrated lower inter-helical tilt angles by 7° – 16°, resulting in a more packed more (Figure II-13). B). The antiparallel three-helix bundle fold of α_3D produced a distorted 3Cys site, which could lead to formation of "asymmetric" metal complexes. C) The EXAFS analysis on Hg-α_3D**IV** revealed a Hg-S(Cys) bond length at 2.36 Å, which is indicative of a trigonal T-shaped complex with two short and one long (from Cys 28) bonds.

Now knowing that the incorporation of cysteine (in α_3D**IV**) and bulky histidine residues (in α_3D**H$_3$**) is possible in α_3D without compromising its overall fold, I designed an asymmetric

2HisCysMet copper-binding site found in the ET center of native cupredoxins plastocyanin, rusticyanin and azurin. However, azurin has a fifth ligand that is provided by a backbone carbonyl group, which would be difficult to incorporate in the α_3D scaffold. In nature, a β-barrel fold encompasses this metal center, where the copper ion is forced in a so-called rigid,"entatic" state. This unique copper complex exhibits some of the most interesting physical properties, such as an intense absorption band in the visible range (ε_{600nm} = 3000 - 5000 M^{-1} cm^{-1}), a compressed hyperfine coupling constant (<70 x 10^{-4} cm^{-1}), a short Cu-S(Cys) bond (2.1 – 2.3 Å) and large Cu(II/I) reduction potential (+180 – +800 mV vs. NHE). In Chapter 3, I described my work in building a cupredoxin site within the α_3D framework and examining how these properties are retained and/or changed in this distinct fold. Three distinct peptides were designed and are designated as core (α_3D-CR), chelate (α_3D-CH) and core-chelate (α_3D-ChC) constructs. In the core construct (α_3D-CR1), the 2HisCys residues are placed on three separate strands, which is analogous to the ligand arrangement in α_3D**IV**. For the chelate constructs (α_3D-CH3 and α_3D-CH4), a His-X_2-Cys chelate motif was incorporated at the helix-loop junction of helix 1. The metal binding site of both the core and chelate constructs are located at the C-terminal end of the bundle. Finally, in the core-chelate (α_3D-ChC2) construct, the His-X_2-Cys chelate group is contained inside the bundle, one layer toward the N-terminal end, forcing these ligands into a preformed conformation via steric interactions.

The circular dichroism analysis on α_3D-CR1, α_3D-CH3, α_3D-CH4 and α_3D-ChC2 demonstrated that these constructs still retained a well-folded α-helical structure, with percent folding that range from 63 – 98 %. However, the Gibbs free energy of unfolding for α_3D-CR1 and α_3D-CH3 revealed that the incorporation of the 2HisCys residues destabilized the fold by 2.4 – 3.7 kcal mol^{-1} compared to α_3D (5.1 kcal mol^{-1}). Cu(II) binding to the CR and CH constructs produced tetragonal CuT2 species, displaying an intense absorption band between 380-400 nm (~2000 M^{-1} cm^{-1}) and broad band between 600 – 700 nm, as well as large $A_{||}$ values of 152 – 185 x 10^{-4} cm^{-4}. α_3D-ChC2 generated a distinct brown copper species that has been observed in mutated azurin and rusticyanin. Unlike its core and chelate counterparts, this construct displayed two intense LMCT bands at 401 (4429 M^{-1} cm^{-1}) and 499 (2020 M^{-1} cm^{-1}) nm, indicating a significant structural change in the Cu(II) complex when bound to a core-chelate site. The

growth in intensity of the 494 nm band also suggested an improved S(Cys)π and Cu $3d_{x^2-y^2}$ interaction. Additionally, the $A_{||}$ value of α_3D-ChC2 is still ~70 x 10^{-4} cm^{-4} greater than its native counterparts. Overall, these results showed that these designed CuT1 sites lack the proper constraints to bind Cu(II) in an entatic state. Instead the copper ion is dictating geometry of the complex, however a remarkable effect was observed when this metal ion is bound deeper inside the hydrophobic core away from the C-terminal end of the bundle. Even though these constructs did not retain the spectroscopic signatures for the Cu(II) state, XAS analysis on the Cu(I) adducts revealed a coordination environment closely similar to that in reduced CuT1 proteins azurin and stellacyanin. These Cu(I) complexes exhibited a short Cu-S(Cys) bond at ~2.2 Å, as well as Cu-N(His) bond distances of ~2.0 Å. Figure V-3 shows models of the Cu(I) complexes derived from EXAFS. α_3D-CR1 and α_3D-ChC2 fitted well to a Cu(I)N_2S model, while α_3D-CH3 and α_3D-CH4 correlated with a Cu(I)N_2S_2 model. The chelate group of the latter two constructs is at the interface of the C-terminal end; and therefore, the Cu(I) ion is likely located at the border of the bundle, which allows the S(Met72) ligand to form a short Cu-S bond (Figure V-3C&D.)

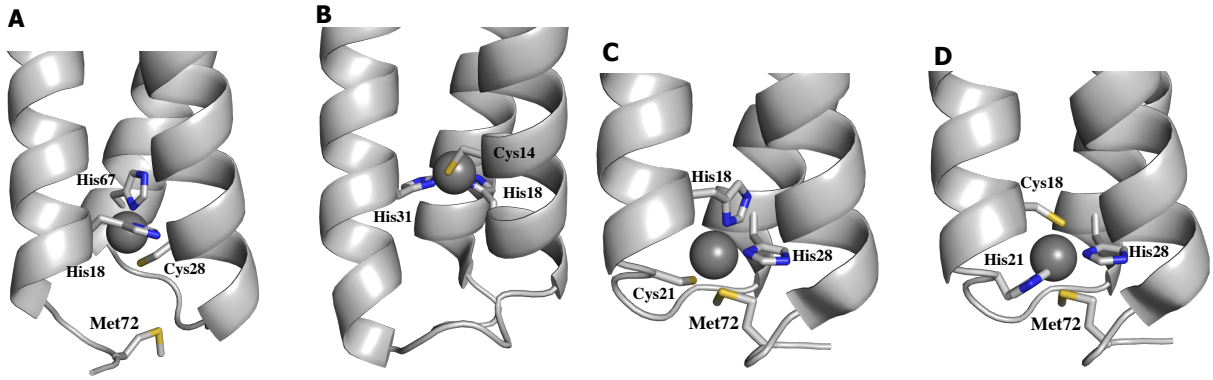

Figure V-3. EXAFS analysis on the Cu(I) adducts of the designed constructs indicated the formation of three- and four-coordinate Cu(I) complexes as show in this figure. Cu(I)α_3D-CR1 (A) and Cu(I)α_3D-ChC2 (B) fitted well to a Cu(I)N_2S model. Cu(I)α_3D-CH3 (C) and Cu(I)α_3D-CH4 (D) fitted well to a Cu(I)N_2S_2 model, where the second S atom was expected to originate from Met72.

The major objective of my thesis was to build an electron transfer site in the α_3D framework. To achieve this goal, I investigated the redox properties of the designed copper metallopeptides by determining their reduction potential and ET activity (Chapter 4). As previously mentioned, a highly positive Cu(II/I) reduction potential (E°) is one of the defining features of native cupredoxins. The E° values of the designed constructs were determined using

an electrochemical method, protein film voltammetry. This method involves the adsorption of proteins on an electrode surface to generate an electro-active film for ET. The Ala77Cys derivative of α_3D-CR1, α_3D-CH3, α_3D-CH4 and α_3D-ChC2 were tethered to a gold electrode, via Au-S(Cys) bonds, and the reduction potentials were determined from a trumpet plot analysis. The E° of α_3D-CR1, α_3D-CH3 and α_3D-CH4 range from +363 to +399 mV (vs. NHE), which is comparable to plastocyanin and azurin. α_3D-ChC2 has an E° of +462 mV, which is 200 mV lower than the reported value for rusticyanin. Overall, the electrochemistry work illustrates that I am successful at building a copper center in the α_3D framework with the suitable redox property for ET.

After establishing the reduction potential, the ET activity of the designed constructs was investigated using a photophysical method, flash-quench photolysis. This method was utilized to produce a highly oxidizing rutheniumtrisbipyridine species, Ru(III)bpy$_3$, that can interact with the designed constructs (starting at the Cu(I) state) through an intermolecular ET reaction. The transient spectra and kinetic trace (at 400 nm) of Cuα_3D-CR1, Cuα_3D-CH3 and Cuα_3D-CH4 demonstrated the decay of Ru(III)bpy$_3$ and the appearance of a Cu(II) species, indicating an ET reaction between the photo-oxidant and designed copper peptide. Further, the 1st order and bimolecular rate constant of these constructs were determined to be 10^5 s^{-1} and 10^8 s^{-1} M^{-1}, respectively. The latter values are comparable to corresponding results reported for plastocyanin, azurin and stellacyanin, using the same photophysical techniques. Interestingly, Cuα_3D-ChC2 was not observed to interact with the photo-oxidant, implying that the copper center is not easily accessible. Moreover, the ET reorganization energy (λ_{total}) of Cuα_3D-CH3 and Cuα_3D-CH4 were obtained from a study that used a series of photo-oxidants with varying reduction potentials. Both constructs generated a relatively high λ_{total} of ~1.1 eV, which is 1 eV lower than a copper compound [e. g., Cu(phen)$_2$]*[12]* and is equivalent or 0.5 eV higher than the reported values for plastocyanin and azurin*[13-16]* (Figure V-4). These results suggest that Cuα_3D-CH3 and Cuα_3D-CH4 require less geometry change during ET, compared to Cu(phen)$_2$, which interchanges between a tetrahedral and tetragonal complex. Overall, the work described in Chapter 4 illustrates that I have successfully imparted a copper center in the α_3D scaffold that is capable of participating in ET.

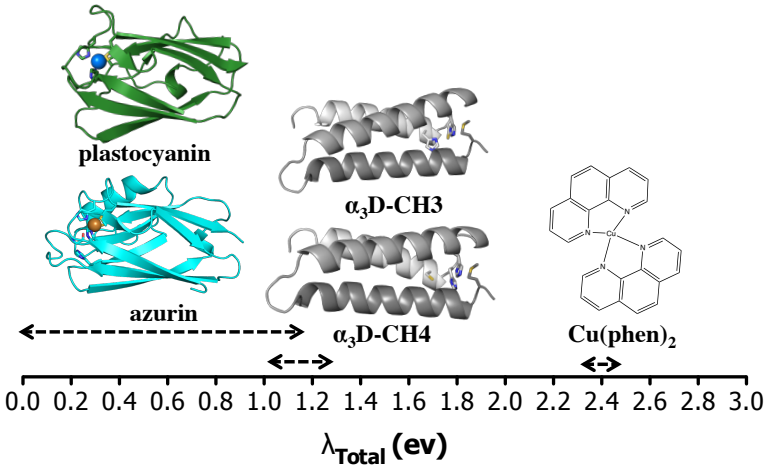

Figure V-4. Reorganization of designed constructs compared to native proteins and Cu(phenanthroline)$_2$.

Figure V-5 illustrates the efforts by the Pecoraro group to functionalize the α_3D scaffold. The first derivative, α_3D**IV**, possesses a 3Cys site that was used to investigate further metallobiochemistry of toxic heavy metals (Figure V-5A). Subsequently, a 3His zinc catalytic site was incorporated and demonstrated carbonic anhydrase activity (Figure V-5B). The third derivative, which is the work in this thesis, aimed to incorporate an asymmetric, redox active site in α_3D, found in cupredoxins. Photophysical measurements on Cuα_3D-CR1, Cuα_3D-CH3 and Cuα_3D-CH4 showed intermolecular electron transfer activity with ruthenium(III)trisbipyridine, exhibiting that the α_3D scaffold has now been imparted with an ET site.

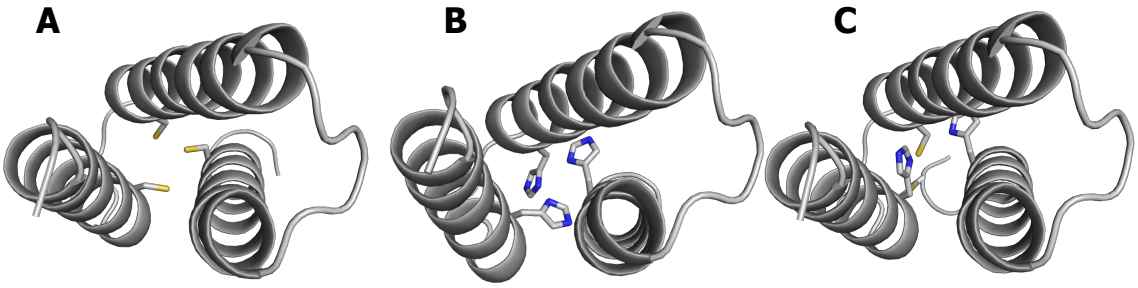

Figure V-5. Functional evolution of α_3D constructs. A) α_3D**IV** was designed to contain a 3Cys site to investigate further metallobiochemistry of toxic heavy metals cadmium, lead and mercury. B) A 3His site was incorporated in α_3D to bind zinc and this complex demonstrated the function of carbonic anhydrase. C) An asymmetric 2HisCys(Met) site found in the electron transfer site of cupredoxins was designed in the α_3D scaffold, which is the work described in this thesis. From the photophysical measurements, cupredoxin models Cuα_3D-CR1, Cuα_3D-CH3 and Cuα_3D-CH4 demonstrated ET reactivity with ruthenium(III)trisbipyridine.

Future Directions

De novo protein design allows for an iterative approach in modifying a stable peptide framework. The structure of apo α_3D**IV** demonstrates that by mutating packing Leu to Cys residues to achieve a thiol-rich metal binding site a well-folded peptide construct is still retained. This structure offers an excellent foundation for enhancing the understanding of protein tolerance for incorporation of metals, an important consideration for designing future systems in the field of protein engineering. We are now in a position to modify α_3D**IV** in order to improve metal binding affinity, selectivity and geometry, with the intention of studying the metallobiochemistry of toxic heavy metals further. These goals can be achieved with new constructs that will result in a more preformed, more symmetric triscysteine metal binding site in an antiparallel three-helix bundle. In the ensemble of structures, the S_γ of Cys28 consistently orients towards the C-terminal end forming a skewed S_3 plane. The first iteration involves moving the Cys28 one layer towards the N-terminal end by performing Cys28Phe and Phe31Cys mutations (Figure V-6A). Placing a Cys in the 31st position produces a S_3 plane that is perpendicular with the helical bundle and a Phe in the 28th provides a capping and directing force for Cys31, which yields a preformed site. The Cys28Phe/Phe31Cys α_3D**IV** construct can then be further modified with an iteration that directs the S_γ of Cys18 to form more of an "a" orientation (Figure V-6B). This can be achieved with an Ile14Leu mutation, where a smaller Leu residue affords space to form for the thiol group of Cys18 to orient towards the core. We are currently working on these modifications and plan to characterize the heavy metal binding properties of these new α_3D**IV** constructs fully.

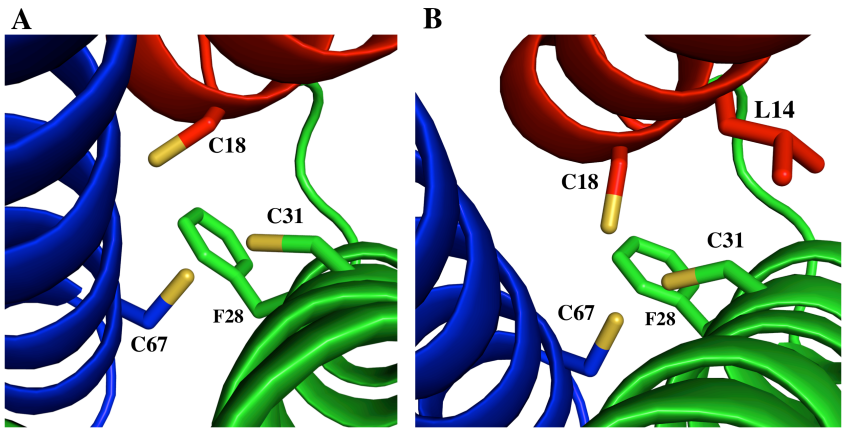

Figure V-6: New α_3D**IV** designs. (A) Model of α_3D**IV** C28F, F31C, where the Cys residue on helix 2 is moved one layer above its original position in order to form a triscysteine plane that is more perpendicular with the bundle. (B) Model of α_3D**IV** I14L, C28F, F31C, where a bulky Ile is replaced with a Leu residue in able generating space for the Cys residues to ultimately form a preformed metal binding site.

In addition to these mutants, improving metal binding affinity, selectivity and geometry in α_3D**IV** could also be achieved in a Grand α_3D**IV** derivative. The transition from Tri to Grand in the three-stranded coiled-coil system, which involves an expansion by one heptad, has been shown to enhance the stability of the tertiary structure by more than 5 kcal mol^{-1}. Further stabilizing the three-bundle of α_3D**IV** could result in a better-ordered hydrophobic core, therefore lead to a more preformed metal binding site. Grand α_3D**IV** can be achieved by extending the third heptad in each helix: AAIKTR to helix 1, IAAFESE to helix 2 and AAIRDE to helix 3. Table V-1 lists the amino acid sequence of this Grand derivative.

Table V-1. Amino acid sequence of α_3D**IV** compared to Grand α_3D**IV**.

Peptide	**Sequence**			
	abcdefg	abcdefg	abcdefg	loop
α_3DIV	MGSWAEFKQR EAE**C**AAFEKE NPEVEALRKE	LAAIKTR IAAFESE AAAIRDE	**C**QAL LQAY **C**QAYRHN	GGS KGKG
	abcdefg	abcdefg	abcdefg	abcdef loop
Grand α_3D**IV**	MGSWAEFKQR EAELAAFEKE NPEVEALRKE	LAAIKTR **C**AAFESE AAAIRDE	**C**AAIKTR IAAFESE **C**AAIRDE	LQAL GGS LQAY KGKG LQAYRHN

Bolded residues denote metal binding ligands.

As described in Chapter 3, the Cu(II) spectrum of α_3D-CR1, α_3D-CH3 and α_3D-CH4 produced tetragonal species with an intense absorption band between 380 – 400 nm. The corresponding spectrum of α_3D-ChC2 is markedly different and displayed two intense bands at 400 and 494 nm. This Cu(II) complex formed a brown species in solution that has been observed in a rusticyanin and an azurin mutant, where the Met axial ligand had been replaced with Glu residue. The copper site in these cupredoxin mutants was transformed to a tetragonal from a distorted tetrahedral geometry. Even though the absorption spectrum of Cu(II)α_3D-ChC2 deviated from its family, its copper center still reflects the property of a CuT2 tetragonal complex. To perturbed this geometry, the α_3D-ChC2 can be redesigned to include a fourth ligand that can lift the Cu(II) ion out of a tetragonal plane and generate a tetrahedral environment (Figure V-7). The first proposed derivative incorporates a Glu residue at the 35th position (α_3D-ChC2 Ile35Glu), modeling the copper site in nitrosocyanin[17] (Figure V-7A). A formation of a red copper spectrum will result in a 10 nm red and 50 nm blue shift of the 400 and 499 nm bands, respectively. The second iteration, α_3D-ChC2 Ile35Gln, (Figure V-7B) is inspired by the metal binding site in the green copper center of stellacyanin and nitrite reductase.[18] The success of this construct would be reflected by a 50 – 100 nm red shift in its absorption spectrum compared to α_3D-ChC2, as well as an inversion of the molar extinction coefficients as illustrated in Figure V-7B. The third derivative models a blue copper site by performing a Leu11Met mutation on the α_3D-ChC2 construct (Figure V-7C). To avoid forming a short Cu-S(Met), the Met residue is placed two layers above the 2HisMet metal binding site. Ultimately, these future constructs will bring us one step closer to achieving a CuT1 site within the α_3D framework.

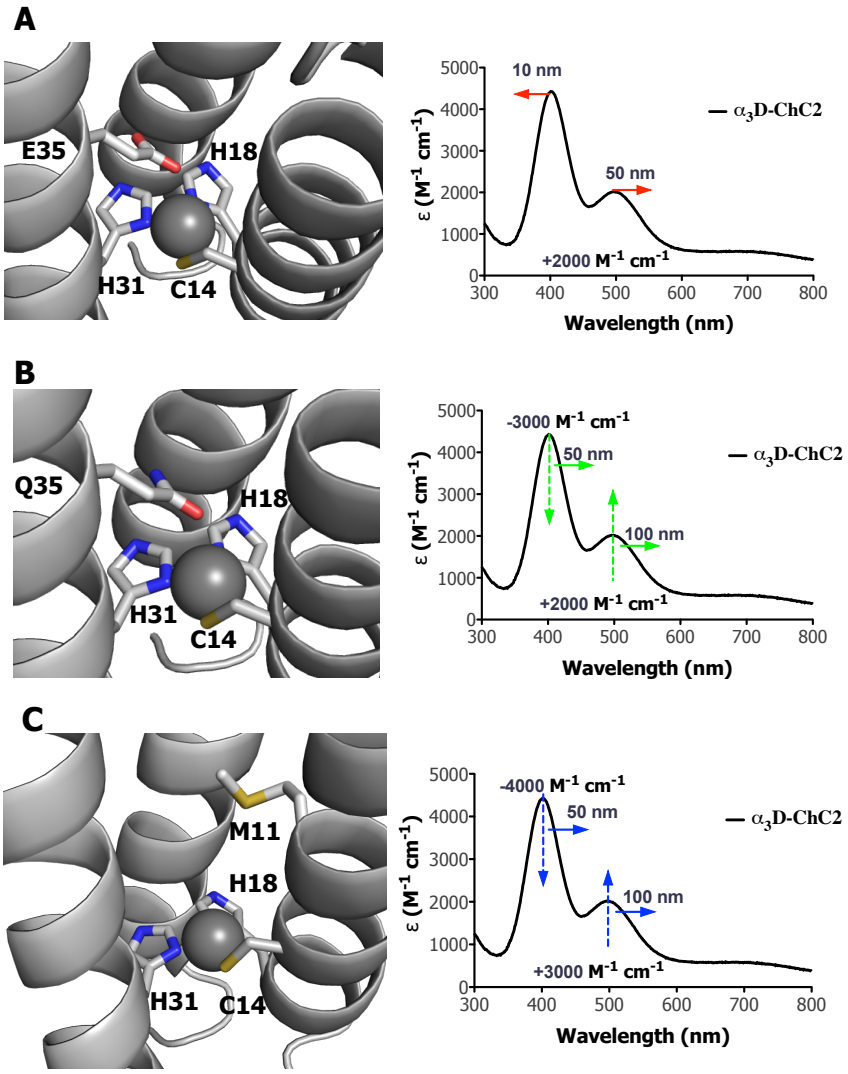

Figure V-7. Future α_3D-ChC2 constructs and expected changed in the Cu(II) spectrum of α_3D-ChC2 (right). A) α_3D-ChC2 I35E, modeling red copper center nitrosocyanin. B) α_3D-ChC2 I34Q, modeling green copper center stellacyanin. C) α_3D-ChC2 L11M, modeling blue copper center of plastocyanin and rusticyanin.

The electrochemical work showed that the desgined constructs can function as electro-active protein films. This led to further measurements that demonstrated that the Cu(II/I) reduction potential of cupredoxin proteins can be recapitulated in an α-helical fold. Moreover, it was observed that the ET reaction between the copper center and gold electrode is a quasi-reversible process because the reductive and oxidative peaks do not converge at slow scan rates.[19] This separation has been previously proposed to stem from a disordered protein film, where the proteins are predicted to take different conformations on the surface. One strategy used to control the order of the protein film is a co-grafting or co-adsorption technique.[20] For a

gold a surface, alkane thiol derivatives has been widely used to form a self-assembled monolayer (SAM) that creates ordered surface for protein adsorption. I have employed this technique in my electrochemical studies, but instead of forming a SAM, the alkane thiol was utilized to fill the gaps between the grafted peptides as shown in Figure V-8A. Preliminary data in Figure V-8B shows the trumpet plot of Cuα_3D-CR1 co-grafted with 1-hexanethiol. This data demonstrates that the co-grafting method did not affect the reduction potential of the metal center, however a separation between the potentials still exists. Therefore, future work could focus on varying the length and R group of alkane thiol and examine if these modifications can alter electrochemical behavior of the designed constructs.

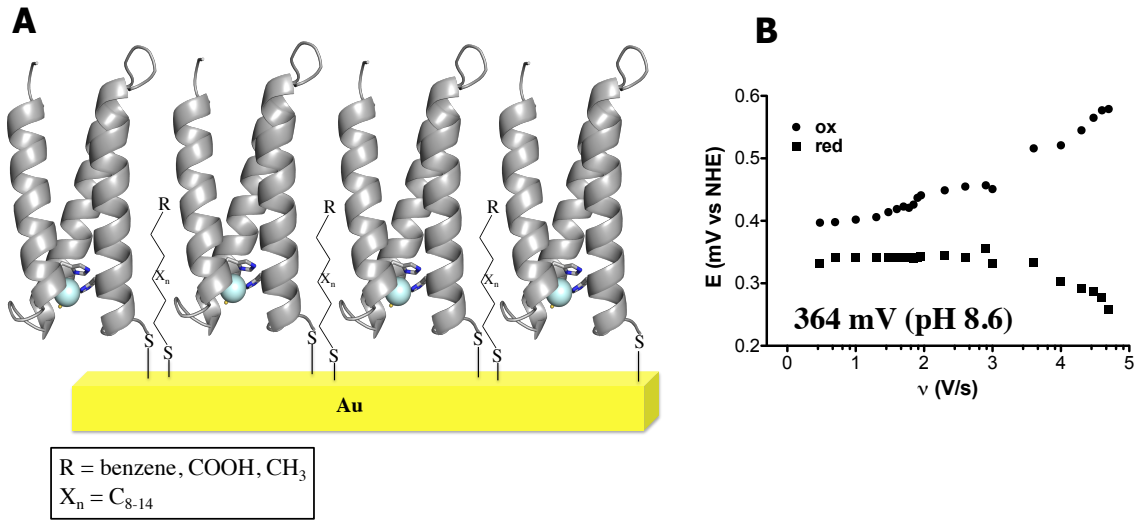

Figure V-8. Future electrochemical work on the designed constructs. A) Cartoon of co-grafting technique. B) Trumple plot of Cuα_3D-CR1 cografted with 1-hexanethiol.

The main objective of my thesis is to create copper metallopeptides capable of performing intermolecular ET. The photophysical work gives proof that Cuα_3D-CR1, Cuα_3D-CH3 and Cuα_3D-CH4 are capable of participating in an ET reaction with a photo-oxidant. Even though such function is evident, the ET pathway from the photo-oxidant to the copper center is unclear. This is especially important for future work that aims to study long-range ET in the α_3D scaffold. The 1st order rate constants of Cuα_3D-CR1 and Cuα_3D-CH4 are comparable to their apoprotein control, which indicates that protein oxidation is the rate-limiting step in the ET reaction. This protein oxidation could originate from a nearby Tyr residue, as in the case for

α_3D-CR1, or from one of the bound ligands, as expected for Cuα_3D-CH4. To elucidate this pathway, subsequent work could focus on mutating redox active to apolar residues, in a step-wise manner. The differences in the rate will provide insight into which residue(s) is oxidized prior to the copper center, as well as the origin of the ET reaction (e.g., side-on or from the C-terminal end of the bundle). Moreover, this future work is particularly important in understanding the ET reactivity of the core-chelate construct, Cuα_3D-ChC2, which was not oxidized by the photo-oxidant. In other words, we can begin to explore if ET in the α_3D system can only occur at the ends of the bundle. If that is the case, what strategies could we use to activate a core-chelate metal center? Perhaps placing a redox active residue, such as Tyr, near the core-chelate site, could mediate an ET reaction between the photo-oxidant and the copper center. Future work on the design aspect of this project can focus on such strategies.

In addition to elucidating the ET mechanism, subsequent work could also focus on expanding the Marcus plot (Figure IV-15) to obtain more precise reorganization energy. The current plots lack ET rates at lower driving forces. This work could be completed with a water soluble zinc phthalocyanine [Zn(PcS)] and phtalocyanine [H_2(PcS)] compound, which have reduction potentials of +821 and +862 mV (vs. NHE), respectively.

Once the ET is fully developed and realized in the α_3D scaffold, one can start designing bifunctional/bimetallic constructs that aim to examine photo-induced long-range ET and -redox-coupled catalysis as shown in Figure V-9. The first objective can be achieved by attaching a chromophore to one end of the bundle, such as ruthenium trisbipyridine, and incorporating a copper center at both ends of the bundle: CuHis$_2$Cys at the C-terminal (similar to α_3D-CR1 and α_3D-CH3) and CuHis$_3$ at the N-terminal end (zinc binding site in α_3D**H$_3$**). Overall, this work will lead to the exploration of the distance decay factor, which indicates the ET efficiency through a protein environment. β sheets have been shown to be more effective at mediating long-distance ET reactions than α-helices.[21] The α_3D scaffold provides a novel platform for examining this factor in an α-helical environment. Moreover, the same bimetallic construct can be further developed to perform a redox-coupled reaction, such as the nitrite reduction in copper nitrite reductase[22] (Figure V-9B). Tegoni, Yu and co-workers[23, 24] have reported nitrite reduction at the

$CuHis_3$ site of a three-stranded coiled-coil peptide and ongoing work by Tebo and co-workers demonstrated that the corresponding reaction can achieved in $Cu\alpha_3D\mathbf{H_3}$. Therefore, it is conceivable that future work will result in an α_3D construct that contains an ET and a catalytic site, modeling the active sites and function of native copper nitrite reductase.

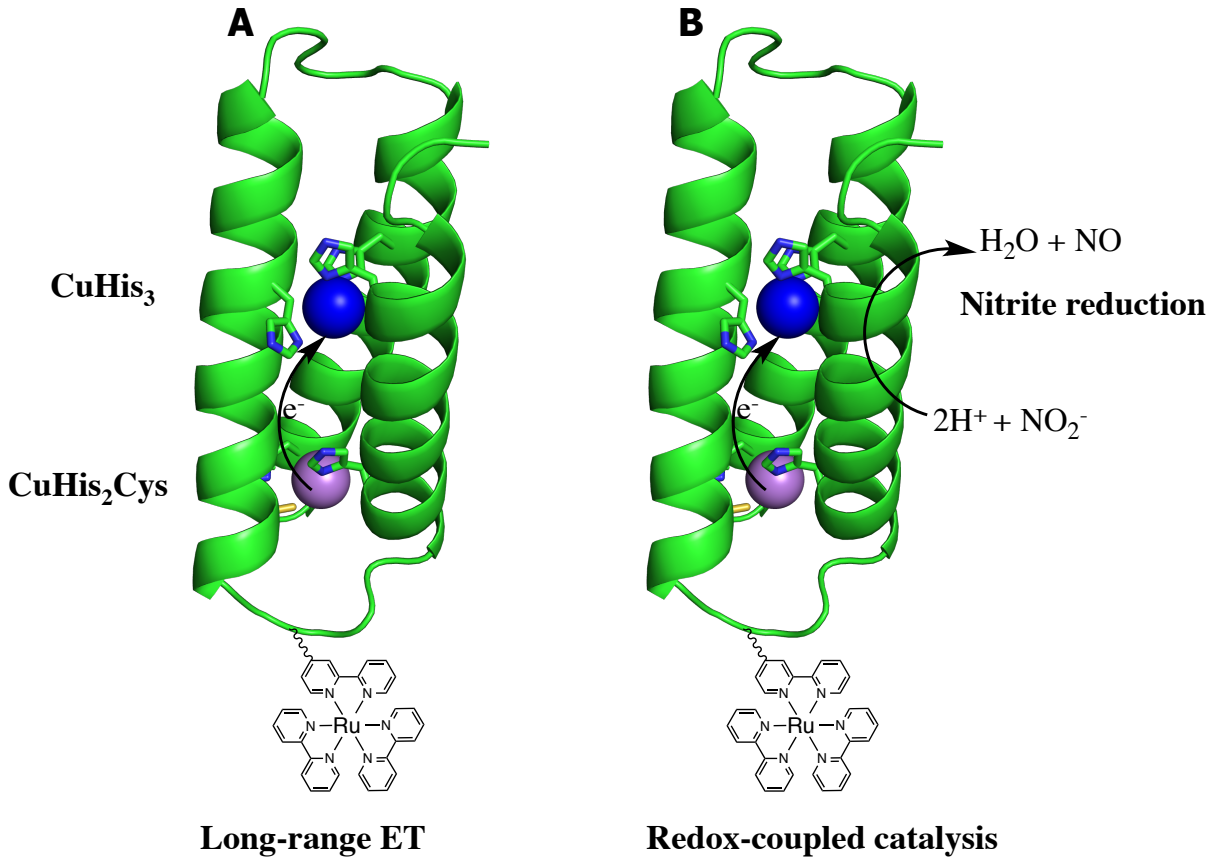

Figure V-9. Future designs that aim to study long-range ET (A) and redox-coupled catalysis (B).

In conclusion, the work in this thesis demonstrates significant advancement in the *de novo* design field. Prior to this work, the α_3D framework was functionalized with a toxic metal and catalytic center only. I have expanded this project by solving the solution structure of apo $\alpha_3D\mathbf{IV}$ establishing that α_3D is a well-defined scaffold that can be imparted with a metal-binding site. By demonstrating ET copper metallopeptides, I extended the functional scope of this framework. The work described in this thesis and by my co-workers forecasts exciting developments in *de novo* design of nature inspired multicenter redox enzymes.

References

[1] Lu, Y., Yeung, N., Sieracki, N., and Marshall, N. M. (2009) Design of functional metalloproteins, *Nature 460*, 855-862.

[2] Yu, F., Cangelosi, V. M., Zastrow, M. L., Tegoni, M., Plegaria, J. S., Tebo, A. G., Mocny, C. S., Ruckthong, L., Qayyum, H., and Pecoraro, V. L. (2014) Protein design: toward functional metalloenzymes, *Chem. Rev. 114*, 3495-3578.

[3] Plegaria, J. S., and Pecoraro, V. L. (2015) Sculpting Metal-binding Environments in *De Novo* Designed Three-helix Bundles, *Isr. J. Chem. 55*, 85-95.

[4] Christin, T. C., James, D. L., Mark, J. N., Dutton, P. L., Dan, E. R., and William, F. D. (1994) Design of a heme-binding four-helix bundle, *J. Am. Chem. Soc. 116*, 856865.

[5] Lombardi, A., Summa, C. M., Geremia, S., Randaccio, L., Pavone, V., and DeGrado, W. F. (2000) Retrostructural analysis of metalloproteins: application to the design of a minimal model for diiron proteins, *Proc. Natl. Acad. Sci. U. S. A. 97*, 6298-6305.

[6] Jinyou, Z., Jennifer, H. A., Ryan, K., John, H. D., Michael, J. B., and Brian, R. G. (2004) Design of a Five-Coordinate Heme Protein Maquette: A Spectroscopic Model of Deoxymyoglobin, *Inorg. Chem. 43*, 8218-8220.

[7] Steve, S. H., Ronald, L. K., Mitchell, L., Wand, A. J., and Dutton, P. L. (2004) The HP-1 maquette: From an apoprotein structure to a structured hemoprotein designed to promote redox-coupled proton exchange, *Proc. Natl. Acad. Sci. U. S. A. 101*, 5536-5541.

[8] Walsh, S. T., Cheng, H., Bryson, J. W., Roder, H., and DeGrado, W. F. (1999) Solution structure and dynamics of a *de novo* designed three-helix bundle protein, *Proc. Natl. Acad. Sci. U. S. A. 96*, 5486-5491.

[9] Chakraborty, S., Kravitz, J. Y., Thulstrup, P. W., Hemmingsen, L., DeGrado, W. F., and Pecoraro, V. L. (2011) Design of a three-helix bundle capable of binding heavy metals in a triscysteine environment, *Angew. Chem. Int. Ed. Engl. 50*, 2049-2053.

[10] Cangelosi, V. M., Deb, A., Penner-Hahn, J. E., and Pecoraro, V. L. (2014) A *de novo* designed metalloenzyme for the hydration of CO_2, *Angew. Chem., Int. Ed. Engl. 53*, 7900-7903.

[11] Plegaria, J. S., Dzul, S., Zuiderweg, E. R., Stemmler, T. L., and Pecoraro, V. L. (2015) Apoprotein Structure and Metal Binding Characterization of a *De Novo* Designed Peptide, α_3DIV, that Sequesters Toxic Heavy Metals, *Biochemistry*.

[12] Winkler, J. R., Wittung-Stafshede, P., Leckner, J., Malmstrom, B. G., and Gray, H. B. (1997) Effects of folding on metalloprotein active sites, *Proc. Natl. Acad. Sci. U. S. A. 94*, 4246-4249.

[13] Di Bilio, A. J., Hill, M. G., Bonander, N., Karlsson, B. G., Villahermosa, R. M., Malmström, B. G., Winkler, J. R., and Gray, H. B. (1997) Reorganization Energy of Blue Copper: Effects of Temperature and Driving Force on the Rates of Electron Transfer in Ruthenium- and Osmium-Modified Azurins, *J. Am. Chem. Soc. 119*, 9921-9922.

[14] Bjerrum, M. J., Casimiro, D. R., Chang, I. J., Di Bilio, A. J., Gray, H. B., Hill, M. G., Langen, R., Mines, G. A., Skov, L. K., Winkler, J. R., and et al. (1995) Electron transfer in ruthenium-modified proteins, *J. Bioenerg. Biomembr. 27*, 295-302.

[15] Regan, J. J., Di Bilio, A. J., Langen, R., Skov, L. K., Winkler, J. R., Gray, H. B., and Onuchic, J. N. (1995) Electron tunneling in azurin: the coupling across a β-sheet, *Chem. Biol. 2*, 489-496.

[16] Sigfridsson, K., Ejdebäck, M., Sundahl, M., and Hansson, Ö. (1998) Electron Transfer in Ruthenium-Modified Spinach Plastocyanin Mutants, *Arch. Biochem. Biophys. 351*, 197-206.

[17] Lieberman, R. L., Arciero, D. M., Hooper, A. B., and Rosenzweig, A. C. (2001) Crystal structure of a novel red copper protein from *Nitrosomonas europaea*, *Biochemistry 40*, 5674-5681.

[18] Hart, P. J., Nersissian, A. M., and George, S. D. (2011) Copper Proteins with Type 1 Sites, *Encyclopedia of Inorganic and Bioinorganic Chemistry*.

[19] Jeuken, L. J. C., and Armstrong, F. A. (2001) Electrochemical Origin of Hysteresis in the Electron-Transfer Reactions of Adsorbed Proteins: Contrasting Behavior of the "Blue" Copper Protein,

Azurin, Adsorbed on Pyrolytic Graphite and Modified Gold Electrodes, *J. Phys. Chem. B 105*, 5271-5282.

[20] Armstrong, F. A., Barlow, N. L., Burn, P. L., Hoke, K. R., Jeuken, L. J., Shenton, C., and Webster, G. R. (2004) Fast, long-range electron-transfer reactions of a "blue" copper protein coupled non-covalently to an electrode through a stilbenyl thiolate monolayer, *Chem. Commun.*, 316-317.

[21] Gray, H. B., and Winkler, J. R. (2003) Electron tunneling through proteins, *Q. Rev. Biophys. 36*, 341-372.

[22] Adman, E. T., and Murphy, M. E. P. (2011) Copper Nitrite Reductase, *Encyclopedia of Inorganic and Bioinorganic Chemistry*.

[23] Tegoni, M., Yu, F., Bersellini, M., Penner-Hahn, J. E., and Pecoraro, V. L. (2012) Designing a functional type 2 copper center that has nitrite reductase activity within α-helical coiled coils, *Proc. Natl. Acad. Sci. U. S. A. 109*, 21234-21239.

[24] Yu, F., Penner-Hahn, J. E., and Pecoraro, V. L. (2013) *De novo*-designed metallopeptides with type 2 copper centers: modulation of reduction potentials and nitrite reductase activities, *J. Am. Chem. Soc. 135*, 18096-18107.